Faculty of Science and Engineering
Department of Exploration Geophysics

Analytical and Numerical Modelling of Elastic Properties of Isotropic and Anisotropic Rocks and Their Stress Dependencies

Pavel Golodoniuc

This thesis is presented for the Degree of
Doctor of Philosophy
of
Curtin University

May 2015

DECLARATION

To the best of my knowledge this thesis contains no material previously published by any other person except where due acknowledgement has been made. Some results of the research that formed parts of the thesis chapters were published as conference extended abstracts and journal publications, and acknowledged accordingly in the thesis layout along with indication of my contribution to these works. This thesis contains no material that has been accepted for the award of any other degree or diploma in any university.

Signature:

Date: 5 May 2015

ACKNOWLEDGEMENTS

First and foremost, I have to thank my committee members for their guidance and support, Prof Boris Gurevich, Dr Marina Pervukhina, Dr Maxim Lebedev, and Dr Andrew Squelch. Without their assistance and dedicated involvement in every step throughout the process, this PhD dissertation would have never been accomplished. I would like to thank you very much for your support and understanding over these past six years.

I would like to express my deepest gratitude to my advisor, Dr Marina Pervukhina, for her excellent guidance, caring, patience, and providing me with an excellent atmosphere for doing research. Your advice on both research as well as on my career have been priceless. I would like to thank Prof Boris Gurevich, who was abundantly helpful and offered invaluable assistance and support. I would also like to thank Dr Maxim Lebedev for all the wonderful times spent in University laboratories that allowed to get an insight on experimental side of research. I appreciate all the help and support from Dr Andrew Squelch in computing aspects of my research. In addition, I would like to thank Curtin University research staff member, Assoc Prof Roman Pevzner, for assistance and insightful discussions over the years. This list would not be complete without a mention of Ms Deirdre L. Hollingsworth, Administrative Officer at the Department of Exploration Geophysics, who has always been responsive and helpful in administrative matters.

Deepest gratitude are also due to the CSIRO research staff, Dr Valeriya Shulakova, Dr David N. Dewhurst, Dr Tobias M. Müller, and Dr Michael B. Clennell, for the collaborative atmosphere that would not be otherwise possible without their support. Big thank you to all of them for willingness to share ideas and their vast knowledge. In addition, I would like to thank Dr Thomas Poulet, Dr Robert Woodcock, and Dr Simon Cox for their continual encouragement, support and career development advices.

Special thanks goes to Dr Claudio Delle Piane, Dr Nordgård Bolås, and Dr Jerome Fortin, who kindly provided rock samples and performed laboratory sample analysis, which were essential for the research.

I would also like to thank my family members for their endless love and support. They were always supporting me and encouraging me with their best wishes.

Finally, I would also like to thank all of my friends who supported me in this journey, and incented me to strive towards my goal.

TABLE OF CONTENTS

LIST OF FIGURES

LIST OF TABLES

ABSTRACT

Rock physics is a key scientific discipline that provides the bridge between seismic data and key rock properties, such as porosity, permeability and saturation. In this thesis, we try to establish links or dependencies between these key properties and the data obtained via direct measurements in laboratories. The knowledge of these dependencies allows more accurate estimations of porosity, permeability and saturation – the parameters that oil and gas industry is looking for to be produced from surface seismic data. With the recent development of computer tomography (CT) scanners, capable of producing high resolution 3D models of rock samples at resolutions up to below one micron, advancements in computer technologies, and availability of massive computational resources, it became feasible to run complex numerical experiments involving realistic models, verify various approaches, and up-scale laboratory measurements to much larger volumes. Advances in X-ray micro-CT technologies, including compact micro-CT scanners and gigantic national synchrotron facilities and scientific computing provides a range of opportunities for geophysicists to acquire realistic digital representations of complex porous media via computer tomography. This comes with its own challenges and requires a thoughtful approach to be taken during CT image acquisition and initial image processing including filtering, smoothing, and segmentation of different rock phases. Here we obtain realistic geometry of the Donnybrook sandstone sample and calculate sonic velocities using numerical simulation methods. For numerical simulations of rock properties the finite element method (FEM) is used. FEM is widely accepted in simulations of linear elastic properties of porous rocks and reliable implementations of FEM algorithms are readily available in a number of scientific packages. Predictions of elastic properties of sandstones are not straightforward and a number of studies have shown a tendency to predict somewhat higher velocities than obtained via laboratory experiments. Even at high resolution provided by modern micro-CT scanners they still cannot resolve cracks or contacts between individual grains in a mineral assembly. To explain the reason of discrepancies between numerically simulated and measured velocities, we compare velocities of saturated Donnybrook sandstone and Gassmann's predictions. At all confining pressures below 50 MPa the Gassmann's predictions are below measured velocities that is commonly explained by the squirt effect caused by presence of microcracks or grain

contacts. These grain contacts can reduce elastic moduli dramatically and lead to overestimation of elastic properties at low stresses. However, these microcracks are too thin and have very small aspect ratios (10^{-4} to 10^{-3}) to be detected by X-ray microtomography, and therefore are not accounted for in numerical simulations. Therefore, since we cannot yet see the grain contacts and microcracks at resolution we have available today, we need to further study this topic theoretically. This is the next topic of our study. In the development and refinement of the 3D models of rock samples, I contributed to the micro-CT image processing and reconstruction of 3D models and further digital model adaptation for finite element modelling (FEM). Significant part of my work involved development of numerical algorithms, FEM numerical simulations, parallelization and up-scaling of algorithms to computer clusters, as well as interpretation of results.

In the following chapters, we investigate elastic properties of grain contacts and microcracks using stress dependency of dry and saturated sandstones. We are specifically focused on the parameters, such as characteristic effective stress, under which microcracks are getting closed, as well as the function that describes stress dependency of crack specific areas. We begin with isotropic sandstones, then generalize our stress sensitivity approach to anisotropic media and specifically apply it to shales. I contributed to the development of the analytical model and implemented the numerical modelling workflow in MATLAB that is at the core of this study. I applied the numerical modelling procedure to shale samples, systematized, visualized, and contributed to critical analysis of the obtained results.

Stress dependency of elastic properties of shales is of high interest as shales are the most common rock type encountered in sedimentary basins. We took about 40 shale samples with stress sensitivities of elastic constants measured in laboratories and developed a model that describes the effect of orientation distribution function (ODF) of microcracks on elastic properties of rock matrix. This rock matrix can itself be either isotropic or anisotropic. The latter case is practically important as our shale samples are shown to be intrinsically anisotropic irrespective of presence of cracks in their structure. Combining the dual porosity approach of Shapiro (2003) with the non-interactive approximation of Sayers and Kachanov (1995) we propose a model that allows description of stress dependency of all five elastic coefficients of transversely isotropic (TI) shales by treating both the orientation distribution of clay

platelets and the compliance ratio of platelet contacts as model parameters. At first, this is done for the case of isotropic effective pressure and later extended further to the case of application of uniaxial anisotropic stress. We show that the same parameters can be used to describe variations in elastic stress tensor in shales in the case of applied isotropic or anisotropic stress. My contributions were in the areas of the further development of the proposed analytical model, performing numerical simulations on the test dataset, and theoretical interpretation of the results.

Finally, we have applied effective medium approach to study the effect of silt on elastic properties of shales and demonstrated that shale vertical velocities can be modelled with two key parameters, namely silt fraction and porosity. These parameters can easily be measured by conventional and modern logging tools. This forms another important aspect of proposed methodology – the fact that it does not rely on the detailed knowledge of mineralogical content of shales. This represents a great advantage as mineralogical analysis is a very laborious process by itself and this information is rarely readily available for shales. I contributed to the development of the new analytical model, implementation of the numerical workflow for forward and inverse modelling of shale and clay elastic properties, as well as analysis and interpretations of modelled results and their comparison with the experimentally measured data.

INTRODUCTION

RESEARCH BACKGROUND

Finding relationships between rock texture and macroscopic elastic properties is important for understanding and quantitative interpretation of borehole and surface geophysical data. Computing such macroscopic properties from the rock microstructure is called elastic up-scaling. Due to the complexity of real rock microstructure, such as random distribution of grains of different mineralogy, and presence of different pore systems (e.g., primary and secondary porosity, microporosity, microcracks, etc.), such up-scaling can be a challenging task. Typical methods used for the elastic up-scaling include effective medium theory, micro-mechanical models, upper and lower bounds based on continuum mechanics, or empirical relationships determined from laboratory or field measurements (e.g., Mavko et al., 1998).

As far as the micro-structural characterization of porous rocks is concerned, a great deal of progress has been achieved through the development of scanning electron microscopy (SEM) (e.g., Solymar and Fabricius, 1999) and X-ray computed tomography (e.g., Flannery et al, 1987; Van Geet and Swennen, 2001) yielding 3D representations of rock microstructure. Nowadays synchrotron source and conventional source X-ray micro-CT can provide us with direct measurements of a 3D structure at resolution down to one micron (e.g., Al-Raoush and Wilson, 2005; Arns et al., 2002; Spanne et al., 1994). These microtomograms yield detailed information on grain shapes and pore networks and are the building blocks of digital rock models.

Stress dependency of elastic properties of reservoir rocks and seals is practically important for seismic interpretation, overpressure prediction, fluid identification and 4D monitoring. In spite of the importance of the problem, there is no conventional theory that allows describing stress dependency of rock elastic properties with a small number of physically plausible parameters. Shapiro (2003) proposed a physically plausible explanation of the exponential saturation of ultrasonic velocities into a linear trend that was experimentally observed by Eberhart-Phillips et al. (1989) for a number of clean and shaly sandstones. Shapiro showed that such a stress dependency could be explained by cracks with low aspect ratios of the same order of magnitude. Shapiro (2003) also suggested that the

decrease of elastic compliances of sandstones could be described with the same exponent as the decay of soft porosity with effective stress. In this thesis, we test this hypothesis by applying the proposed stress dependency theory on a number of sandstones.

In the next stage of research, we further modify the model suggested by Shapiro (2003) to the case of shales that exhibit transversely isotropic symmetry. Two major causes of elastic anisotropy in shales are intrinsic anisotropy of clay platelets and anisotropic orientation distribution function (ODF) of these anisotropic clay platelets. These two sources of elastic anisotropy were successfully used to predict elastic anisotropy of shales in a number of studies starting from the pioneering work of Hornby et al. (1994). Two other causes of elastic anisotropy in shales, (1) anisotropic distributions of discontinuities and (2) aligned silt inclusions, have drawn much less attention in studies of shale elastic anisotropy. Stresses affect elastic properties of shales due to presence of discontinuities such as cracks and compliant grain contacts. Shapiro and Kaselow (2005) suggested a stress dependency model for orthorhombic media based on dual porosity approach that imply bimodal distribution of pore compliances and superposition of deformation fields caused by closure/shape change of these two groups of stiff and compliant pores under applied stress. Assumption that was made by Shapiro and Kaselow (2005) and Ciz and Shapiro (2009) to apply this dual porosity model to transversely isotropic (TI) media implicitly assumes that normal and tangential compliances of each individual crack are equal. This assumption oversimplifies the model and results in S_{13} coefficient to be independent of stress. However, as shown in Chapter 3, even though the variation of elastic compliance S_{13} might be small, it should not be neglected. Sayers (2005) used aligned discontinuities in shales to study stress dependency of elastic properties of shales. Here we use experimentally measured stress dependencies of shale elastic moduli to derive ODFs and elastic properties of cracks. We use formalism suggested by Sayers and Kachanov (1995) to develop a model that describes stress dependencies of all five elastic constants of TI media, if applied stress is isotropic.

The stresses in the Earth interior are usually anisotropic. Non-hydrostatic stresses can cause elastic anisotropy, if the rock was initially isotropic, and change the rock symmetry, if the rock was initially anisotropic. The effect of a stress field on a discontinuity depends on the orientation of the discontinuity with respect to the

stress field. Knowledge of the pattern of stress-induced anisotropy (as expressed, for example, by the ratio of anisotropy parameters) can be useful for distinguishing it from other causes of anisotropy, such as presence of aligned fractures. Such patterns can also be used to distinguish, say, P-wave anisotropy from S-wave anisotropy estimated from S-wave splitting (Crampin, 1985). A number of authors have modelled stress-induced anisotropy by assuming the rock to contain a distribution of penny-shaped cracks, and considering variation of this distribution due to applied stress (e.g., Nur, 1971, Sayers, 1988). However, penny-shaped crack geometry may not give an adequate quantitative description of discontinuities in rocks (Sayers and Han, 2002; Gurevich et al., 2009; Angus et al., 2009). Alternatively, Mavko et al. (1995) and Sayers (2002) developed modelling approaches that do not restrict the shape of discontinuities but instead infer their parameters from measurements. These approaches require numerical calculations to obtain an insight into anisotropy patterns. To obtain a more simple and general insight to these patterns, we make some simplifying assumptions that allow us to compute the anisotropy parameters analytically. Our main assumption is that a rock containing some distribution of discontinuities is subjected to a small uniaxial stress (or uniaxial strain) such that it results in a weak anisotropy of the discontinuity orientation distribution, and weak elastic anisotropy. The initial crack orientation distribution is obtained from the study of stress dependencies of shales subjected to isotropic stresses.

Modelling of anisotropic elastic constants of shales, if their porosity and mineralogy are known, is a challenging task by itself. Shales are complex composite materials with nanoscale intrinsically anisotropic clay platelets of different mineralogy interacting with nanoscale pores and silt inclusions of different shape, size and composition. Thus, many factors might critically affect elastic properties of these complex shale composites. Considerable effort has been made to predict elastic properties of shales using detailed knowledge of clay and silt mineralogy provided by XRD analysis, silt and pores aspect ratios and orientation distribution functions of clay platelets obtained from SEM images (e.g., Hornby et al., 1994; Peltonen et al. 2008; Peltonen et al., 2009; Bayuk et al., 2007; Jensen et al., 2011).

Mixture theories are routinely used to calculate effective elastic moduli of composites in the case when elastic properties of the constituents are known. Unfortunately, elastic properties of pure clays cannot be experimentally measured. A

classic approach for modelling of elastic properties of clays was suggested by Hornby et al. (1994). This classic approach counts for partial alignment of clay platelets (but not for microcracks or other discontinuities) and uses mixture theories to predict clay properties from the properties of water and 100% pure clay end members. This requires knowledge of a large number of parameters that can be measured only in laboratories on a limited number of samples, such as orientation distribution function of clay platelets, volumetric fraction of silt and volumetric fractions of free and bound water. Moreover, as it has been recently shown by Sayers (2013), this classic approach cannot explain larger strain magnitudes normal to bedding commonly observed in shales when stress is applied parallel to bedding compared to strain magnitudes parallel to bedding when the same stress magnitude is applied normal to bedding.

A different approach is reported in a series of papers (Ulm and Abousleiman, 2006, Ortega et al., 2007, Ortega et al., 2009). Ulm and Abousleiman (2006) directly measured elastic properties of wet clay packs using nanoindentation techniques and determined that the variations in shale elastic properties can be captured with two key parameters, namely, silt fraction and volumetric fraction of clay in a wet clay pack. Pervukhina et al. (2008a) inverted anisotropic moduli of shales obtained from ultrasonic pulse method for anisotropic moduli of clay. They confirmed the importance of the silt fraction and the fraction of clay in a wet clay pack as the key parameters for predicting of elastic properties of shales and elaborated the method. The obtained method was applied for modelling of sonic velocities in shales using silt fraction and porosity measured with wireline logging tools in a vertical well, which is detailed in Chapter 5. The obtained velocities were shown to be in a good agreement with measured sonic velocities throughout the depth of about 500 meters. Systematic overestimation of measured velocities by simulated sonic velocities in another vertical well was explained with abnormally high pore pressure (Pervukhina et al., 2013). The difference was calibrated with the experimental measurements and used for estimation of pore pressure in the formation. We use the same model to estimate elastic anisotropy in shales. Five elastic coefficients of vertical transversely isotropic (VTI) media are calculated using silt fraction and porosity measured with logging tools. Then these elastic coefficients are used to calculate phase and group

velocities in off-axis angle directions. The obtained velocities are then compared with sonic velocities measured in a deviated well.

Within this thesis, I refer to work and activities conducted as part of the research in first person plural form as each chapter is the result of discussions and close collaboration between various individuals involved in this research. The results arising from the research reported in this thesis have been published as journal papers and conference extended abstracts, which is acknowledged accordingly in the Thesis Layout section below.

THESIS LAYOUT

The following is intended to describe the motivation of each chapter of this thesis and briefly outline the chapter content.

Chapter 1. The thesis begins with an investigation of the potential to simulate the elastic properties of rocks on digitized 3D models obtained from high resolution X-ray computer tomography (CT) images and the possibility to accurately up-scale the results to larger volumes. The proposed up-scaling approach appeared to be a challenging task not only because most commercial micro-CT scanners do not allow clear differentiation between main constituents of sandstones we analysed (e.g., quartz, feldspar, clay minerals, etc.), but also because of the fact that even at the maximum resolution of ~1 micron it is still not sufficient to resolve complex geometry of the grain contact areas. We carefully describe various approaches to CT image processing, such as filtering, smoothing, and segmentation of rock phases. Further, we mesh both grain and pore phases using irregular meshing procedures available in AVIZO software package and compare the effect of mesh accuracy with uncertainties of numerical modelling of elastic properties. Finally, we compare the numerical simulation results with experimentally measured elastic parameters and show that the discrepancy obtained at low effective stresses can be explained by the presence of grain contacts that are unresolvable by micro-CT scanners. In this chapter, I used the material published in the following journal paper with permission from leading co-authors:

> Shulakova V., Pervukhina M., Müller T. M., Lebedev M., Mayo S., Schmid S., Golodoniuc P., De Paula O. B., Clennell B. M., and Gurevich B., 2011, Computational elastic up-scaling of sandstones on the basis of X-ray micro-tomographic images: Geophysical Prospecting, doi: 10.1111/j.1365-2478.2012.01082.x.

My personal contributions to the publication were in the areas of (a) micro-CT image processing, reconstruction of 3D models of rock samples, and further digital model adaptation for finite element modelling (FEM) in ABAQUS FEA software suite, (b) FEM numerical simulations of effective bulk and shear moduli,

(c) algorithms development, parallelization and up-scaling to computer clusters, and (d) interpretation of results.

Chapter 2. In this chapter, we looked at the physical nature of velocity-stress relationships for isotropic rocks and at the possibility to extend the theory to anisotropic rocks. We test the dual porosity concept proposed by Shapiro (2003) on experimentally measured elastic properties of dry reservoir sandstone from the Northwest Shelf of Australia (Siggins and Dewhurst, 2003). In this chapter, I used the material published in the following extended abstract with permission from leading co-authors:

> Pervukhina M., Gurevich B., Dewhurst D. N., Siggins A. F., Golodoniuc P., and Fortin J., 2010, Experimental verification of the physical nature of velocity-stress relationship for isotropic porous rocks: ASEG Extended Abstract at the 21st International Geophysical Conference and Exhibition (ASEG-PESA), Sydney, Australia.

I developed the numerical modelling workflow in MATLAB that is at the core of this study. I also helped to analyse simulated results and further contributed to model adaptation for the case of anisotropic rocks.

Chapter 3. The idea of the research reported in this chapter stems from successful application of Shapiro's model (2003) to the sandstone as described in the previous chapter. Using Sayers-Kachanov formalism, we develop the stress-dependency model for transversely isotropic (TI) media. The newly developed model describes stress sensitivity behaviour of all five elastic coefficients using four physically meaningful parameters, namely, specific tangential compliance of a single crack, ratio of normal to tangential compliances, characteristic pressure and crack orientation anisotropy parameter. This chapter is based on the published version of the following journal publication with permission from co-authors and publishers (see Appendix B):

Pervukhina M., Gurevich B., Golodoniuc P., and Dewhurst D. N., 2011, Parameterization of elastic stress sensitivity in shales: Geophysics, **76(3)**, p. WA147–WA155, doi:10.1190/1.3554401.

I contributed to the development of the analytical model and implemented it in MATLAB to simulate the effects of application of isotropic stresses on the anisotropic orientation of discontinuities, such as grain or platelet contacts, cracks or fractures. I applied the numerical modelling procedure to 20 shale samples, systematized and visualized the obtained results, and contributed to critical analysis in the Discussion section of the chapter.

Chapter 4. Here we further extend the model proposed in the previous chapter to gain a theoretical insight on the variation of elastic coefficients with anisotropic stress. Anisotropic stress is an important factor that adds to the complexities associated with the intrinsic anisotropy of shales caused by preferred mineral orientation. The model proposed in this chapter allows parameterization of the stress dependency of elastic coefficients of shales under anisotropic stress conditions with only four parameters that can be estimated from experimentally measured data. In this chapter, I used the material published in the following SEG extended abstract with permission from co-authors and publishers (see Appendix B):

Pervukhina M., Gurevich B., Golodoniuc P., and Dewhurst D. N., 2011, Stress dependency of elastic properties of shales: the effect of uniaxial stress: SEG Extended abstract at the SEG 2011 Conference, San Antonio, USA, doi:10.1190/1.3627669.

I planned the research in collaboration with research supervisors, contributed to further development of the proposed analytical model and performed numerical simulations on the test dataset obtained for a shale sample from the Officer Basin in Western Australia. I compared predicted elastic properties variation due to application of uniaxial stress for TI media with experimentally measured data, and was instrumental in theoretical interpretation.

Chapter 5. This chapter consists of two main parts – at first, using Clay-Plus-Silt approach, we model elastic properties of shales from porosity and mineralogy logs, and then we invert the elastic properties of shales obtained from the sonic log measurements in the same vertical well for those of clays.

Clay-Plus-Silt model is based on the idea that elastic moduli of clay can be estimated from total porosity and silt fraction that can relatively easy be obtained from wireline measurements or derived from common log measurements. This gives us an advantage to model and predict elastic properties of shales without detailed mineralogical analysis on samples, which significantly reduces the costs.

In the second half of the chapter, we invert elastic coefficients of shales for vertical profiles of clay elastic coefficients. The results of the analysis give us an insight on how elastic coefficients of shales and clays are controlled by the porosity decrease due to compaction.

In this chapter, I used the material previously published in the following EAGE and SEGJ extended abstracts, and that was later published in the Geophysics in 2015. All published materials were used with permission from leading co-authors and respective publishers (see Appendix B):

- Pervukhina M., Golodoniuc P., Gurevich B., Clennell M. B., Nadri D., Dewhurst D. N., and Nordgård Bolås H. M., 2012, An estimation of sonic velocities in shale from clay and silt fractions from the Elemental Capture Spectroscopy log: Extended abstract, 74th EAGE Conference, Copenhagen, Denmark.
- Pervukhina M., Golodoniuc P., and Dewhurst D. N., 2013, Rock physics modeling of sonic velocities in shales: Proceedings of the 11th SEGJ International Symposium, Yokohama, Japan, 398-401.
- Pervukhina M., Golodoniuc P., Gurevich B., Clennell M. B., Dewhurst D. N., and Nordgård Bolås H. M., 2015, Prediction of sonic velocities in shale from porosity and clay fraction obtained from logs – a North Sea well case study: Geophysics, **80(1)**, p. D1-D10, doi:10.1190/GEO2014-0044.1.

My role in the above mentioned publications were in the areas of (a) planning research activities and contribution to the development of the new analytical model,

(b) implementation of the numerical workflow for forward and inverse modelling of shale and clay elastic properties, and (c) analysis and interpretations of modelled results and their comparison with the experimentally measured data.

CHAPTER 1 – COMPUTATIONAL ELASTIC UP-SCALING OF SANDSTONES ON THE BASIS OF X-RAY MICROTOMOGRAPHIC IMAGES

Up-scaling the elastic properties of digitized rock volumes as obtained from X-ray computer tomography (CT) imaging via computer simulations has the potential to assist and complement laboratory measurements. This computational up-scaling approach remains a challenging task as the overall elastic properties are not only dependent on the elastic properties of the individual grains but also on the hardly resolvable pore spaces between adjacent grains such as microcracks. We develop a digitized rock image and elastic up-scaling workflow based on general-purpose and widely available software packages. Particular attention is paid to the CT image processing including filtering, smoothing, and segmentation, as well as to the strategy for optimal meshing of the digital rock model. We apply this workflow to the microtomographic image of a well-consolidated feldspatic sandstone sample and determine the up-scaled bulk and shear modulus. These effective elastic moduli are compared to the moduli inferred from laboratory ultrasound measurements at variable effective stress [0-70 MPa]. We observe that the numerically up-scaled elastic moduli correspond to the moduli at a certain effective stress level at about 50 MPa, beyond which the effective-stress dependency follows a linear trend. This indicates that the computational up-scaling approach yields moduli as if all compliant (soft) porosity was absent, i.e. microcracks are closed. To confirm this hypothesis, we estimate the amount of soft porosity on the basis of the dual porosity theory (Shapiro, 2003) and find that at 50 MPa the soft porosity is indeed practically zero. We conclude that our computational elastic up-scaling approach yields physically consistent effective moduli even if some geometrical features are below CT resolution. To account for these sub-resolution features either theoretical or additional computational approaches can be used.

In this chapter, I used the material published in the following journal paper with permission from leading co-authors:

> Shulakova V., Pervukhina M., Müller T. M., Lebedev M., Mayo S., Schmid S., Golodoniuc P., De Paula O. B., Clennell B. M., and Gurevich B., 2011, Computational elastic up-scaling of sandstones on the basis of X-ray micro-

tomographic images: Geophysical Prospecting, doi: 10.1111/j.1365-2478.2012.01082.x.

1.1 INTRODUCTION

Recent advances in computer technology triggered the development of elastic up-scaling approaches based on numerical simulations of the elasticity equations directly applied to the digital rock models. Roberts and Garboczi (2000) suggested solving the equations of elasticity using finite element modelling (FEM) directly for microstructure obtained from computer tomography. Based on the FEM algorithm developed by Garboczi (1998), Arns et al. (2002) derived elastic moduli – porosity relationships from microtomograms of Fontainebleau sandstone. A similar approach is adopted by commercial companies such as Ingrain Inc. (e.g., Dvorkin, 2009). To simulate elastic wave propagation in digital rock, Saenger et al. (2007) employed the finite-difference method with a rotated staggered grid. Each of these algorithms was specifically designed to simulate the elastic behaviour of highly heterogeneous structures consisting of a number of components with strongly contrasting properties.

Despite the progress in imaging technology and numerical algorithms, publications reporting numerical simulation of elastic properties of rock from the digitized microtomograms are scarce, and rarely are technical details given. We are not aware of any accurate prediction of elastic properties of rock from a microtomogram apart from the work of Arns et al. (2002) in which the authors studied a well consolidated, clean quartz Fontainebleau sandstone, a real godsend among sandstones. Typically, elastic moduli numerically simulated from microtomograms noticeably overestimate measured ones (e.g., Shulakova et al., 2011), with computed shear moduli being in general more uncertain than bulk moduli. Apparent reasons for this discrepancy between measured and simulated moduli are a complex involving mineralogy of the solid phase of the rock and compressibility of grain-to-grain contacts. Microtomograms obtained with most commercial micro-CT scanners with a single X-ray energy do not allow differentiation between quartz, feldspar and various clays, the three main constituents of most sandstones. Furthermore, current micro-CT resolution is not sufficient to image the grain contact areas. Even if the grain-to-grain geometry could be resolved, the elasticity of the grain contact area, which may be rugose or covered with

submicron layers of clays, remains elusive and is not captured by numerical up-scaling approaches based on a linear elasticity.

The objective of this chapter is two-fold: firstly, to advance our understanding of how successfully elastic properties can be computed from digitized images of porous rocks and how accurate these estimates can be (benchmarked against lab measurements) in the presence of the complexities discussed above; secondly, we aim to develop a workflow that would be widely available to the research community and industry through using general-purpose and broadly accessible software packages. We used the functionality of the commercial packages AVIZO (Visualization Sciences Group) and ABAQUS FEA (SIMULIA), including certain proprietary algorithms and routines embedded within them. Other software packages with similar broad functionality could be employed to the same end with minor variations to our described procedures. We propose a comprehensive rock physics workflow that includes image processing, and theoretical and numerical simulations that allow accurate prediction of elastic properties of feldspathic sandstone from microtomograms. The input for all these algorithms is a set of 3D images obtained by a micro-CT scanner (microtomograms). We first process these microtomograms using AVIZO software. This processing includes filtering, smoothing and segmentation into different phases. We also explore AVIZO[1] capabilities to generate an optimal mesh for subsequent finite-element modelling and propose a methodology for mesh size reduction. The obtained segmented tomograms are meshed and the resultant orphan mesh is saved in an ABAQUS input format. The meshed microstructure is imported into ABAQUS[1] finite element analysis (FEA) software in which elastic moduli of a rock sample are numerically simulated. The accuracy of the meshing and its effect on the accuracy of numerical simulation is tested using a microtomogram of a sandstone sample. Finally, we compare the simulated moduli with the experimentally measured ones.

[1] AVIZO is a trademark of Visualisation Science Group. ABAQUS is a trademark of Dassault Systèmes. The authors do not make any endorsement or recommendations of these products or draw comparison with competitor's software.

1.2 DONNYBROOK SANDSTONE PETROPHYSICAL AND MICRO-CT DATA

To demonstrate our workflow, we will use a sample of Donnybrook sandstone as an example. The Donnybrook is well-consolidated, feldspathic sandstone of Cretaceous age named after the town of Donnybrook in the South-West of Western Australia. The sample was obtained from a surface quarry as a block with no visible sedimentary structures or heterogeneities apart from very subtle planar cross-lamination, so that measurements on core plugs and from small sub-samples are expected to have similar average properties at scales beyond a few mm. Three main constituents of the sample known from a petrographic description are quartz, plagioclase feldspar and dissolved K-feldspar transformed into kaolinite, which also forms grain coatings. Volumetric fractions of these minerals to the rock matrix determined from SEM image (Figure 1.1) are 75%, 13% and 12%, respectively. The average helium porosity of the Donnybrook sandstone measured by an automatic porosity/permeability system AP-608 is 15% and permeability is around 9 millidarcies.

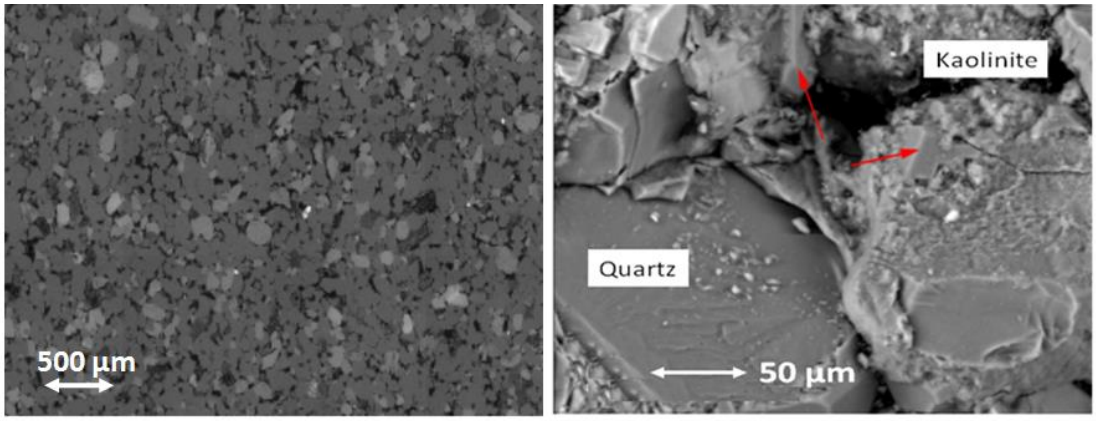

Figure 1.1 2D images of Donnybrook sandstone that comprise 66.1% of quartz (grey), 11.7% of feldspar (light grey), 10.6% of kaolinite (dark grey) and 11.6% of pore space (black): a) obtained on a micro-CT and (b) SEM.

The micro-CT images are obtained with the resolution of 2 μm on an X-ray microscope which has an advantage of giving high phase-contrast useful for highlighting high spatial frequency features at grain boundaries in these samples (Mayo et al., 2003). Firstly, a cube of 400×400×400 pixels is cropped from the centre of the microtomogram and segmented using the methods described below, into a

solid phase and a pore space. Then the original cube is subdivided into eight pieces of 200^3 pixels each (Figure 1.2).

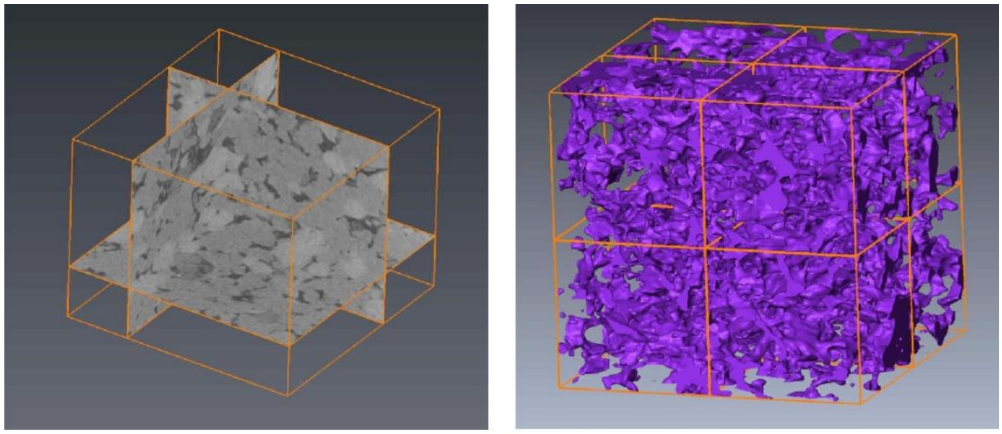

a) b)

Figure 1.2 Donnybrook sandstone microstructure: (a) reconstructed images in three perpendicular directions, (b) interfacial surface: solid phase is transparent and pore space is shown by magenta. The original cube of 400×400×400 pixels is subdivided into eight cubes of 200^3 pixels as shown.

1.3 IMAGE PROCESSING AND MESHING

Micro-CT images cannot be directly used for numerical simulations; they require pre-processing and segmentation into mineral and pore space phases. The data initially come as a set of 2D images, which are later stacked together to form 3D volume. Therefore, the processing of microtomograms can be either 2D slice-based or 3D volume based. Calculations in 2D only are generally much faster than 3D algorithms, but can lead to a range of problems. Throughout the chapter we use 3D processing of microtomograms as 2D slice-based processing can affect the geometry of the image features and cause undesired stripe-shape artifacts (Figure 1.3).

3D image processing is performed in general-purpose commercial AVIZO software developed by Visualisation Science Group (Westenberger, 2008). It allows the user to perform 2 and 3D interactive data visualization, quantitative analysis and processing which features image filtering, mathematical morphology, segmentation, separation and meshing.

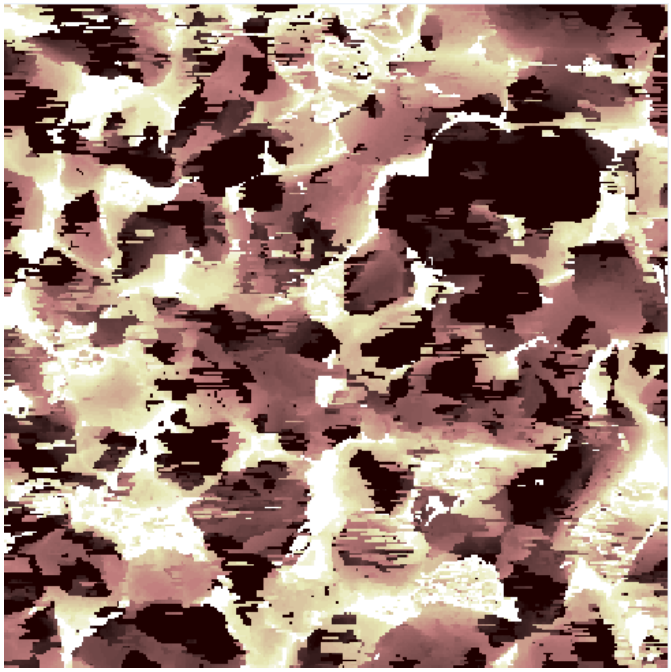

Figure 1.3 Effect of 2D routines (horizontal stripes) applied to the 3D sample of Donnybrook sandstone.

1.3.1 IMAGE PRE-PROCESSING FOR NOISE SUPPRESSION

Micro-CT images always contain noise of various types, which can degrade their quality and impede subsequent quantitative analysis. Thus, the first step in the processing of these images is suppression of random speckle noise. We tested different filter algorithms provided by AVIZO package aiming to enhance the signal-to-noise ratio. 3D low-pass linear filter and 3D Gaussian smoothing filter show tendency to muffle fine details and distort grain edges. In order to suppress noise in regions with constant intensity and maintain grain boundaries, the Edge Preserve Smoothing (EPS) algorithm has been proven to give the best results (e.g., Nikolaou and Papamarkos, 2009). The EPS filter cancels most of the noise, preserves grain boundaries by searching for the most homogeneous fragments in an elementary volume of an input dataset and assigns the averaged value to this elementary volume. The comparison of the performance of the 3D Gaussian smoothing and EPS filters on our data is shown in Figure 1.4. One can see that the 3D EPS suppresses noise yet preserves the most important features of the original image while the Gaussian filter blurs the grain edges. Thus, 3D EPS is our preferred filter and has been applied to the whole volume of the Donnybrook sandstone microtomogram.

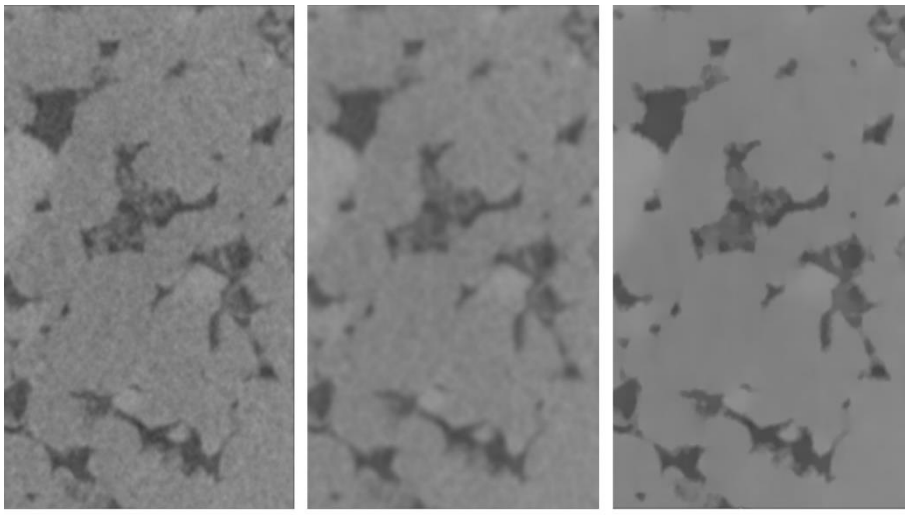

a) b) c)

Figure 1.4 Comparison of different filters on the fragment of 3D Donnybrook sandstone: a) original image, b) 3D Gaussian smoothing filter, and c) 3D edge preserve smoothing.

1.3.2 HISTOGRAM-BASED SEGMENTATION

A 3D microtomogram is a set of numbers corresponding to X-ray densities D(*x*,*y*,*z*) assigned to each voxel (*x*,*y*,*z*) of the scanned volume. The volume is assumed to consist of a fixed number of distinct mineral phases plus the void 'phase' or pore space. After pre-processing, the values of X-ray density are expected to be similar for voxels belonging to the same phase but different for voxels belonging to different phases. It is impossible to know physical properties (such as elastic properties) for each voxel. On the other hand, physical properties of various minerals are well-documented (Mavko et al., 1998). Thus, it is logical to assign the properties of a particular phase (one of the minerals or void) to all voxels belonging to that phase. In order to do this, we need to identify the phase to which each voxel belongs. For instance, if a rock is assumed to consist of minerals 1, 2 and 3, and the space pore, we need to compute, for each voxel (*x*,*y*,*z*), the phase identifier P(*x*,*y*,*z*), which can take values 0, 1, 2, or 3 (with 0 corresponding to the void phase). The transformation of X-ray density volume D(*x*,*y*,*z*), into a phase index volume P(*x*,*y*,*z*) is called segmentation.

As X-ray densities of quartz, feldspar and kaolinite in our micro-CT images are very close, we assume that these minerals form one composite mineral phase, and segment the tomogram into two phases only, namely, 'grains' and 'pores'. The

mineral composition is taken into account at the later stage (see Section – 1.4 Numerical simulation of effective bulk and shear moduli).

The segmentation is based on a simple threshold (histogram-based) algorithm, which assigns labels to voxels according to their intensities. While this approach is considered to be adequate for this type of rock, we are aware that segmentation based on voxel intensity alone will not work universally for all rock types. The final segmentation of the Donnybrook sandstone is shown in Figure 1.5. The white patches represent grains (blue segment on the histogram) and the black patches are pores (white segment on the histogram). Suitable thresholds are found from image histograms showing the number of occurrences of voxel values and the current partitioning of the intensity range.

Histogram-based segmentation algorithms do not properly treat overlapping distributions (e.g., Kaestner et al., 2008) and thus can lead to errors in phase segmentation and phase fractions obtained from microtomograms. Later we analyse the sensitivity of simulated elastic properties to variations in porosity arising from the variation of histogram cut-off values. For this study we opted to treat the solid as a single entity, and incorporate the effects of mineralogical variations through an averaging procedure rather than retaining distinct phases for quartz, feldspar and clay throughout the meshing and computation steps. The segmented tomogram could therefore be converted into a binary format where pore and grain are presented by zeros and ones, respectively. Further operations as described below are then needed to arrive at effective properties of the homogenized solid.

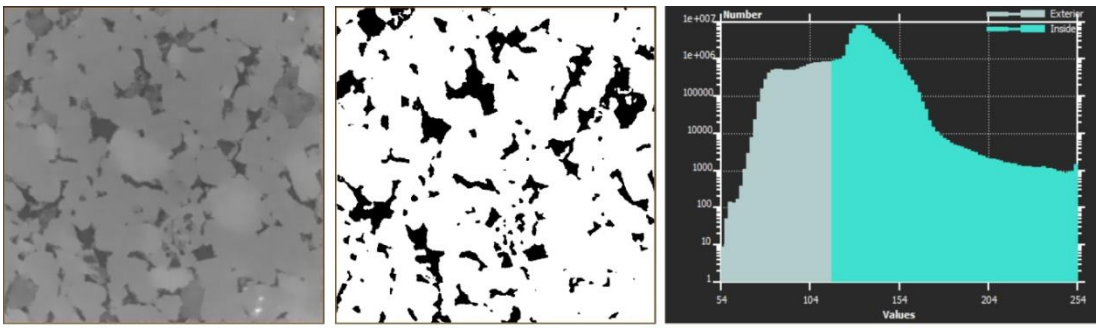

a) b) c)

Figure 1.5 A tomographic slice of a 3D image of a sandstone sample: a) original greyscale image, b) its segmented image consists of two phases – matrix (white patterns) and pore space (black patterns), c) image histogram showing the number of occurrences of voxel values and the current partitioning of the intensity range.

1.3.3 EFFECTIVE MEDIUM CALCULATION OF AVERAGED SOLID PROPERTIES

The micro-CT images of the Donnybrook sample do not have strong contrast in X-ray density between quartz, feldspar and kaolinite, and hence do not allow reliable discrimination between these minerals based on voxel intensity alone. Instead, we estimate the bulk and shear moduli of the solid phase by means of the effective medium theory, namely the self-consistent approximation (SCA) (Berryman, 1980). This approximation was specifically designed to provide estimates that are symmetric with respect to all constituents (that is, it does not treat any constituent as a host or inclusion). Bulk and shear moduli are chosen as 39 and 33 GPa for quartz (Han et al., 1986), 76 and 26 GPa for plagioclase feldspar (Woeber et al., 1963) and 12 and 6 GPa for kaolinite (Vanorio et al., 2003). Volumetric fractions of quartz, feldspar and kaolinite are determined from 2-D SEM image (Figure 1.1a) as 75%, 13% and 12%, respectively. Assuming (from SEM images, Figure 1.1b) that the aspect ratio of the grains is about 1, we obtain effective bulk and shear moduli of the solid phase as 37 GPa and 27 GPa, respectively. The adequacy of these assumptions and our implementation of SCA procedures can only really be tested by comparing computations (described next) against laboratory measurements of the rock elastic properties.

1.3.4 MESH GENERATION AND SIMPLIFICATION

In order to perform finite-element simulation of physical properties, a finite element mesh needs to be constructed. The two-phase segmented microtomogram is then subjected to meshing. First, interphase surfaces are represented by a set of triangles (so called triangular approximation). In AVIZO, this function is performed by SurfaceGen routine. As this and following methods are time and resource consuming, we have divided our 3-D volume into eight smaller subvolumes, and perform all the processing separately for individual subvolumes. The triangulated interface surfaces contain an enormous number of about 106 faces. Such a detailed mesh is often unnecessary, and can be reduced by a given factor S using AVIZO's edge collapsing algorithm (Garland and Heckbert, 1997). Numerical tests show that reduction of the mesh by a factor, *S*, up to 5 produces a geometrical configuration very close to the original mesh. After the simplification, a so-called edge-flipping

technique (De Berg et al., 2008) is applied to triangles that do not meet the Delaunay criterion (Delaunay, 1934; Barber et al., 1996).

Using a reduction factor $S > 5$ for the simplification algorithm results in oversimplified surfaces that do not preserve important details. To reduce the number of surfaces further, we use re-meshing algorithms. The best isotropic (BI) and high regularity (HR) re-meshing algorithms implemented in AVIZO allow us to keep fine details by fixing profiles of surfaces. The best isotropic vertex placement algorithm is based on Lloyd relaxation (Surazhsky et al., 2003). This high regularity algorithm uses explicit regularization of the triangles around a vertex (Szymczak et al., 2003; Alliez et al., 2005). While a decrease in a number of faces is crucially important for speed-up, it also causes distortion in pore shape and perturbs the total porosity. To estimate the effect of such distortion on resultant simulated elastic moduli, we tested 50%, 70% and 90% triangle number reduction for each algorithm. The described workflow of a surface generation, simplification and re-meshing is applied to all the real and model samples below. The only difference in the procedures is a re-meshing algorithm and face reduction coefficients used in re-meshing. Hereafter, we name meshes according to the name of the re-meshing algorithm used and the face reduction coefficient. For instance, mesh HR90 means that the mesh is produced by SurfaceGen routine followed by simplification and re-meshing with high regularity algorithm employing 90% face reduction. The most relevant re-meshing procedure is chosen below based on the comparison of numerical results with the exact theoretical predictions.

1.4 NUMERICAL SIMULATION OF EFFECTIVE BULK AND SHEAR MODULI

1.4.1 ALGORITHM AND SOFTWARE

For numerical simulation of elastic moduli, we use the finite element method that has been utilized in a number of works for elastic (and poroelastic) simulations. The simulations are performed by means of ABAQUS FEA software – a suite of software applications for finite element modelling, meshing and visualization – developed by Dassault Systèmes (http://www.3ds.com). To simulate the uniaxial deformation (P-wave) modulus M of a cubic volume, a normal displacement is applied to one of the faces, say, to the top of the cube while on all other faces the

normal the displacement is set to zero (Figure 1.6a). The modulus is then calculated as the ratio of the average stress to average strain $M = \langle \sigma_x \rangle / \langle \varepsilon_x \rangle$, where angle brackets denote averaging over all the elements. To simulate the shear modulus μ, a shear displacement is applied to the same face while the opposite face is fixed (Figure 1.6b). The bulk modulus is then calculated from *M* and shear modulus μ as $K = M - 4/3\mu$. In this study, we assume the sample to be isotropic and, thus, the choice of faces of loading and directions of displacement is not important.

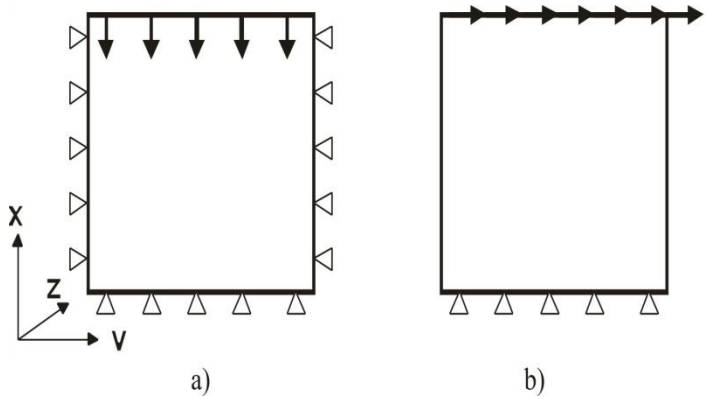

Figure 1.6 Schematic model of displacements applied to the faces of the cube to calculate (a) P-wave modulus and (b) shear modulus.

1.4.2 MESHING UNCERTAINTY

To analyse the effect of meshing on porosity and elastic properties, we have tested it on the spherical inclusion model for which an exact analytical solution is known. We create a 200×200×200 cubic model with a spherical cavity with radius of 25 units at the centre (Figure 1.7). A 3D volume is first generated by stacking a series of 2D tiff images with the nearest-neighbour interpolation algorithm. After assigning phase types as "solid" for the exterior and "pore" for the spherical inclusion, the SurfaceGen algorithm is used to create a triangulated interface. This interface contains 2.5·105 points and 5·105 faces. Then, this interface, is simplified to 0.5·105 points and 1·105 faces. Remeshing is done with HR and BI algorithms using 50%, 70% and 90% reduction coefficients. Any surface composed of triangles is checked for the presence of triangle intersections, which are removed manually by repositioning the corresponding tips. The results for both the algorithms look similar,

though the BI algorithm tends to produce surfaces with fewer intersections. Finally, the meshing of the phase volumes is generated using the TetraGen routine.

The six different models (BI50, BI70, BI90, HR50, HR70 and HR90) are produced by applying different meshing algorithms (best isotropic and high regularity) to this simple geometry with 50%, 70% and 90% of reduction (Figure 1.7c-f). Perturbation of porosity by meshing due to the discretization is shown in Table 1.1. Even coarse meshing (BI90 and HR90) results in only subtle fluctuations in porosity. However, even such small porosity perturbations along with possible shape distortion due to discretization may affect the results of numerical simulations of elastic properties. Below we compare results of numerical simulations of elastic properties for all our models with known theoretical results.

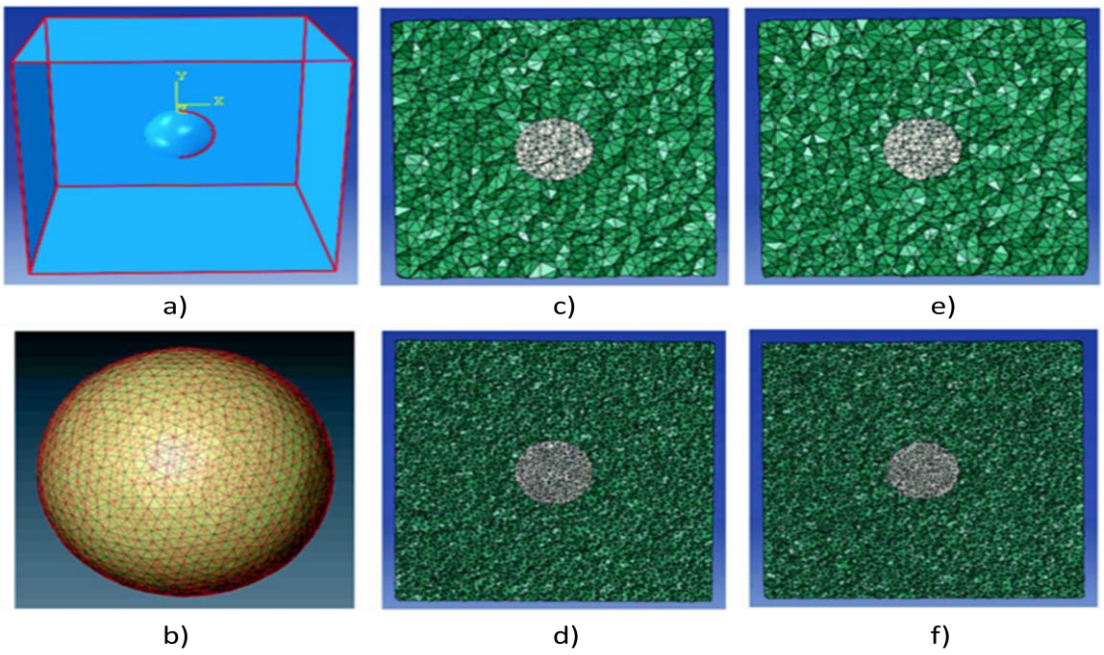

Figure 1.7 Models used for FEM simulations: (a) geometry; (b) overlapped meshing of BI and HR algorithms for spherical inclusion; (c) model BI70; (d) model BI50; (e) model HR70 and (f) model HR50.

Table 1.1 Model of spherical inclusion: surface re-meshing and volumetric gridding parameters. Initial parameters: 25.16·104 points, 50.32·104 faces; simplified surface: 5.00·104 points, 10.00·104 faces.

Remeshing algorithm		# points, $*10^4$	# faces, $*10^4$	# nodes, $*10^5$	# triangles, $*10^6$	# tetrahedrons, $*10^6$	Porosity, $*10^{-3}$	Porosity perturbation,%
BI (%)	90	0.50	0.99	2.63	2.86	1.40	8.02	1.97
	70	1.50	3.00	1.28	1.43	7.09	8.07	1.36
	50	2.50	5.00	2.73	3.10	1.54	8.17	0.14
HR (%)	90	0.50	1.00	2.65	2.89	1.42	8.02	1.97
	70	1.53	3.0	1.30	1.47	7.27	8.07	1.36
	50	2.56	5.13	2.81	3.20	1.59	8.10	0.99

1.4.3 NUMERICAL SIMULATION AND ACCURACY TESTING

We perform FEM simulations for a single spherical dry cavity with volume $\upsilon_p = (4/3)\pi R^3$ and a hydrostatic stress $d\sigma$ applied at the infinity. The effective bulk modulus K_{eff} for such a configuration is (Mavko et al., 1998):

$$\frac{1}{K_{eff}} = \frac{1}{K_g} + \frac{\phi}{K_\phi}. \tag{1.1}$$

Here K_g is bulk modulus of the mineral material and the single pore stiffness K_ϕ is:

$$\frac{1}{K_\phi} = \frac{1}{K_g}\frac{3(1-\nu)}{2(1-2\nu)}, \tag{1.2}$$

where ν is the Poisson ratio of the mineral material.

The simulations are performed for two materials with highly contrasting properties for the host material and spherical cavity. The bulk moduli are assumed to be 35 and 10^{-5} GPa, respectively, and Poisson ratio of the spherical cavity is assumed to be 0.5. Simulations are done for different Poisson ratios ν of 0.1, 0.16, 0.2, 0.3 and 0.4 of the host material. The results of the simulations are shown in Figure 1.8 for both HR and BI algorithms with different reduction coefficients. The larger the value Poisson ratio used, the larger is the deviation of the numerical solution from the theoretical one. However, for all the values of ν, the numerical results converge to the theoretical solution as the meshing quality is improved.

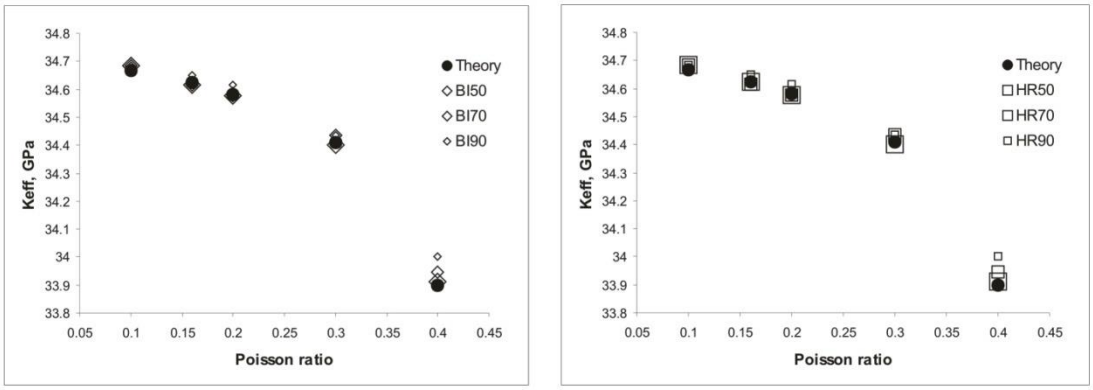

Figure 1.8 Comparison of the results of finite-element simulations with theoretical predictions for meshing fulfilled in (a) AVIZO using the BI method; (b) AVIZO using the HR method.

To estimate the uncertainty caused by the finite size of mesh elements for both HR and BI meshing algorithm with 50%, 70% and 90% of simplification, we calculated relative error in simulated bulk modulus $\Delta K/K_T$, where ΔK is an absolute difference between numerically simulated and theoretically predicted bulk modulus (K_T). Figure 1.9 shows the relative error of the bulk modulus against porosity perturbation, $\Delta\phi$ for the two meshing algorithms. For BI meshing, ΔK linearly decreases with $\Delta\phi$ with proportionality coefficients of 2 and 3 for Poisson ratios of 0.1 and 0.2, respectively, and tends to zero when the porosity perturbation tends to zero. The proportionality constant between ΔK and $\Delta\phi$ has values of 2 and 3 for Poisson ratios of 0.1 and 0.2, respectively. For the HR algorithm ΔK shows linear trends with $\Delta\phi$ as well but with twice the coefficients for the same Poisson ratio.

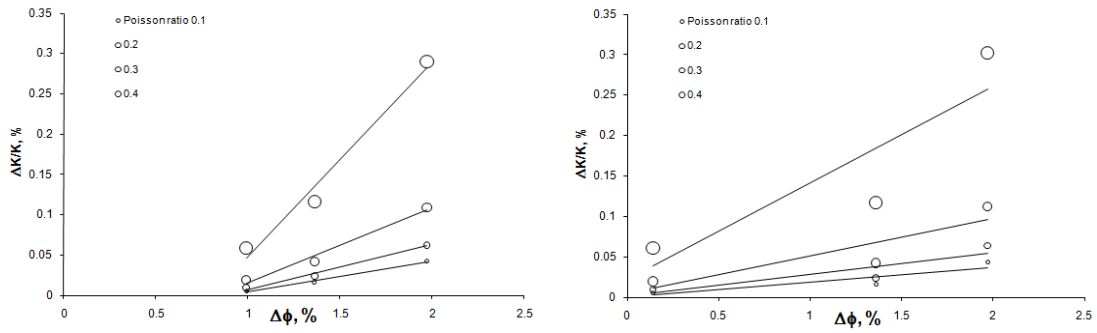

(a) (b)

Figure 1.9 Relative error of bulk modulus simulation caused by a finite size of a mesh element against porosity uncertainty for the (a) high-regularity method of meshing in AVIZO and (b) best isotropic method in AVIZO.

We prefer to use the BI algorithm for meshing the microstructure of the real sample as (1.1) the relative error in bulk modulus $\Delta K/K_T$ is smaller for the same porosity perturbation and (1.2) the BI algorithm is more stable when processing large volumes and complex geometry of real samples. The above analysis also allows estimating an error of simulated elastic moduli caused by discrete meshing. Meshing of the spherical inclusion model using BI50 and BI70 procedures causes relative perturbation in porosity of 0.1% and 1%, respectively. Assuming that the same meshing procedures lead to the same porosity perturbations in the case of the sandstone sample with total porosity of about 15%, the porosity error caused by the meshing is expected to be about 0.1- 1%. Using the relationship between errors in the porosity and elastic moduli for the case of spherical cavity (Figure 1.9), we expect that the uncertainty in elastic moduli caused by meshing will not exceed 1%.

1.4.4 MESHING AND NUMERICAL SIMULATION OF ELASTIC MODULI OF DONNYBROOK SANDSTONE

The cube of 400^3 voxels is cropped into eight cubic subvolumes of 200^3 voxels as shown in Figure 1.2b. To estimate the scatter of the properties within this sample, the porosity of subvolumes is calculated from segmented microtomograms and shows the spread from 12% to 22%. Note that the sample does not have gross heterogeneities or internal structures visible to the naked eye, so we can consider this level property variation to be inherent in this type of natural sandstone.

Each of these smaller cubes has been simplified and re-meshed using with the BI algorithm with 50% of surface simplification.

Figure 1.10 illustrates different stages of surface evolution for the first subvolume of the Donnybrook sample starting from (a) the original surface with 1,269,824 faces, followed by (b) simplification to 199,963 faces using edge-collapsing algorithm and (c) reduction to 1,014,965 faces after the best isotropic re-meshing algorithm reduced the surface by 50% from original.

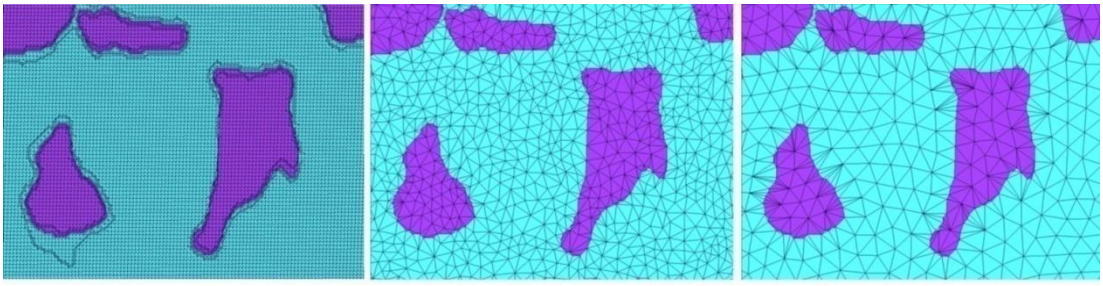

Figure 1.10 Different stages of surface simplification for part 1 of Donnybrook sandstone sample: a) original surface – 1,269,824 faces, b) simplified surface (edge collapsing algorithm) – 199,963 faces, c) re-meshed surface (BI algorithm, reduced by 50%) – 1,014,965 faces.

Surface generation, simplification and re-meshing are followed by meshing of the phase volumes by generating volumetric tetrahedral grids using the TetraGen routine based on the advancing front method (AFM) (Yasushi et al., 2004). A mesh of each of the eight subvolumes contains from 1.5-2.1 · 105 tetrahedra depending on the remeshing procedure (see Table 1.2 for details).

Table 1.2 Donnybrook sandstone: volumetric grid and porosity parameters for all 8 parts.

	Parts							
	1	**2**	**3**	**4**	**5**	**6**	**7**	**8**
φ	0.14	0.17	0.22	0.15	0.15	0.12	0.13	0.12
Δφ, %	0.97	1.18	0.67	1.26	1.28	1.65	2.03	1.56
Points, $*10^4$	4.9	4.9	5.0	4.9	4.6	5.6	4.4	4.9
Faces, $*10^5$	1.0	1.0	1.0	1.0	1.0	1.2	0.9	1.0
Nodes, $*10^5$	3.3	2.8	2.9	2.9	2.8	3.6	2.6	3.2
Triangles, $*10^6$	3.7	3.2	3.4	3.3	3.2	4.1	3.0	3.7
Tetraherda, $*10^6$	1.9	1.6	1.7	1.7	1.6	2.1	1.5	1.8

Figure 1.11 shows meshing of one of the subvolume of Donnybrook sandstone, where rock matrix and pore space are shown by blue and magenta colours, respectively.

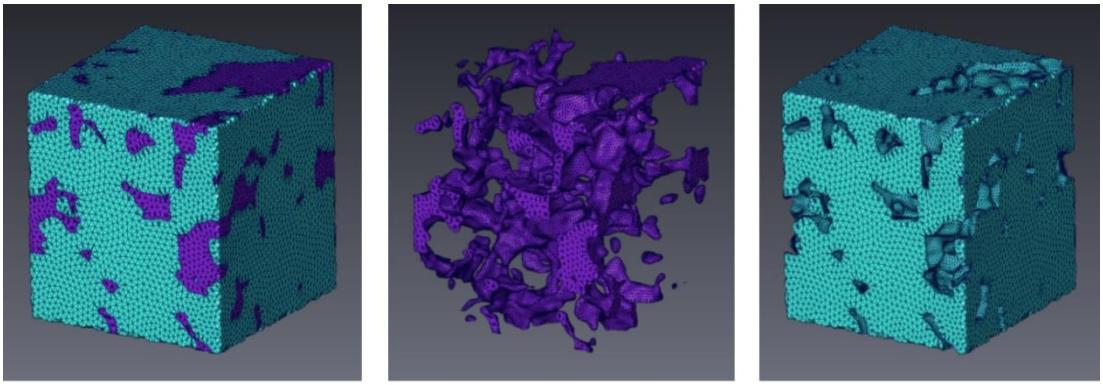

a) b) c)

Figure 1.11 Volumetric tetrahedral mesh of one of eight 200^3 cubes of Donnybrook sandstone: (a) solid and pore phases, (b) pore space and (c) rock matrix.

For each of the eight subvolumes, the elastic moduli are simulated using ABAQUS FEA software. The results of the simulations versus porosity are shown in Figure 1.12. Also shown in Figure 1.12 are SCA estimates for inclusions of different regular shapes, namely, spheres (aspect ratio 1) and oblate spheroids with different aspect ratios of 0.01-0.5. The moduli obtained by numerical simulation of the sandstone subvolumes are comparable with those obtained by SCA for a simple microstructure comprising equivalent elastic solids containing oblate spheroidal voids with aspect ratio ranging from 0.2-1. In order to define the aspect ratios for the actual sandstone pores we perform a statistical analysis. We first identify single items in the volume and thus we determine size, position and shape of each individual piece within a sample. We employ 3D watershed-based algorithm for partitioning (Najman and Schmitt, 1994). The values obtained from the statistical analysis give the average aspect ratio of pores of 0.7 (i.e. nearly equant) for the range of porosities from 0.12-0.22 found in the rock sub-volumes.

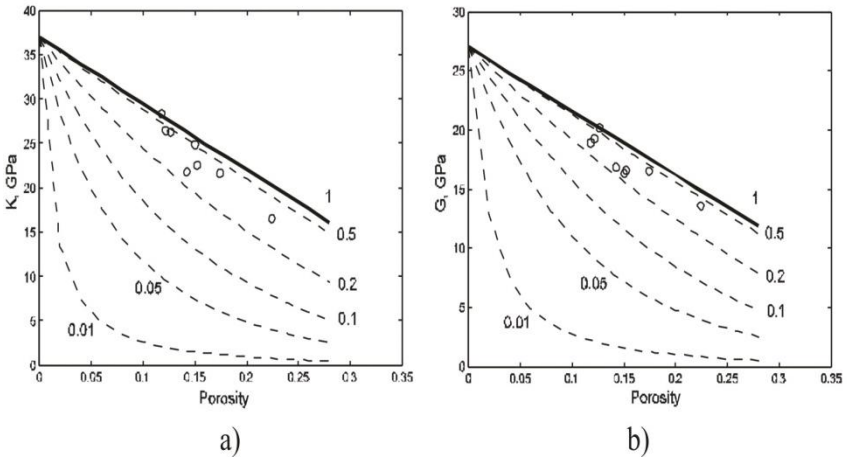

Figure 1.12 Bulk and shear moduli simulated for all parts (circles) in comparison with SCA method predictions for pores of different shapes from spheres (solid line) to oblate spheroids with aspect ratios (0.01-0.5) (dashed lines).

1.4.5 COMPARISON WITH EXPERIMENTAL DATA

The numerically simulated bulk and shear moduli are shown in Figure 1.13 in comparison with experimental data obtained for Donnybrook sandstone at effective stresses of 15-70 MPa using a pulse-transmission system operating at ultrasonic frequencies. The experiment was first performed on a sample with a diameter of 38.15 mm and a length of 93.04 mm and then was repeated for a smaller sample with the same diameter but a shorter length of 56 mm. The experimental data are shown by solid circles with error bars corresponding to measurement uncertainty. The results of numerical simulations are shown by lines parallel to the effective stress axis as the elastic moduli obtained. Note that the porosity of the sample employed for ultrasonic measurements is 15% and the simulated moduli are shown for the subvolume with the same porosity taken from among the 8 smaller cubes. Linear trends that characterize elastic moduli variations at high pressures of 50-70 MPa are shown by dashed lines.

One can see that numerically simulated moduli correspond to the measurements at the confining stress of about 40-50 MPa. To explain the differences between the simulated and experimentally measured moduli, we consider three different effective stress ranges, namely, low effective stresses 0-50 MPa, intermediate stresses of about 50 MPa and high effective stresses of 50-70 MPa. At low effective stresses, the elastic moduli are strongly affected by compliant porosity

represented by grain contacts and microcracks. Such microcracks reduce elastic moduli dramatically at low stresses (e.g., Shapiro, 2003; Angus et al., 2009; MacBeth, 2004; Liu H. H. et al., 2006). However, these microcracks are too thin and have too small aspect ratios (10^{-4} to 10^{-3}) to be detected by X-ray microtomography (even though it is performed at ambient pressure), and therefore are not accounted for in numerical simulations. Indeed, the larger part of each grain-to-grain contact in a microtomogram (Figure 1.1a) is likely to be a highly compliant void of a low aspect ratio (see Figure 1.1b), but is treated in our processing as a welded contact. Thus simulated elastic moduli represent the sample *without* compliant porosity, and correspond to measurements at such pressures where such compliant porosity is effectively closed with respect to transmission of shear and normal tractions. The closure of compliant porosity results in exponential dependency of the moduli with effective confining pressure (e.g., Shapiro, 2003; Ciz and Shapiro, 2009; Pervukhina et al., 2010) and further discussed in Chapter 3.

Figure 1.13 shows this exponential dependency in the experimental data up to the pressure of about 50 MPa. This is precisely where the measurements and simulations agree. At higher stresses of 50-70 MPa, we observe in the experimental points a linear trend of elastic moduli with pressure. Linear dependency of elastic moduli on stress at stresses above 40-50 MPa are a common feature of many rocks (Eberhard-Phillips et al., 1989), and is usually attributed to a decrease of stiff porosity (Mavko and Jizba, 1991; Shapiro, 2003; Vernik and Kachanov, 2010). The numerical simulations do not take into account this reduction of porosity (as the microtomograms are obtained at zero stress) and, thus, underestimate the experimentally measured elastic moduli.

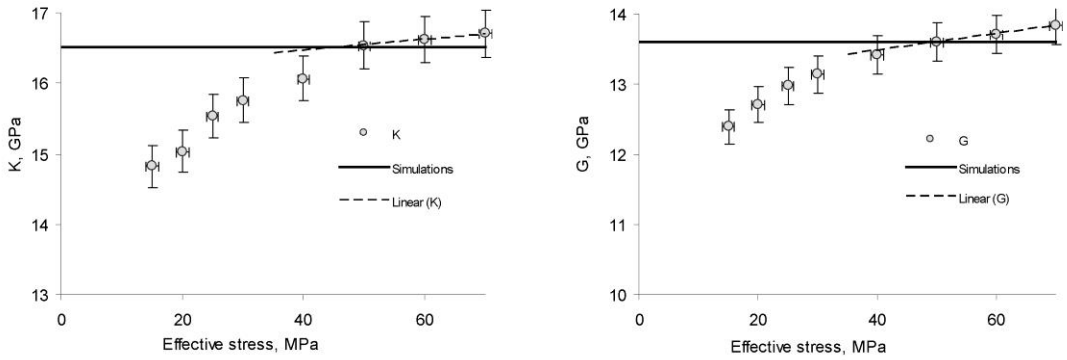

Figure 1.13 Comparison of simulated bulk (a) and shear (b) moduli (solid line) with experimental data (circles) for Donnybrook sandstone measured for effective stresses 15-70 MPa. Linear trend observable at effective stresses of 50-70 MPa is marked with a dashed line.

1.5 DISCUSSION

It is well established that pore space of a sandstone rock free of load-bearing clays can be considered to have, at least from the point of view of elastic properties, two different types of pores that are denominated "stiff" and "soft" porosity (Shapiro, 2003; Gurevich et al., 2009; Pervukhina et al., 2010). The stiff porosity corresponds to pores with large aspect ratios of ~10^{-2}-1 and the soft (compliant) porosity is represented by smaller aspect ratios of about 10^{-3}. The stiff porosity in sandstones comprises equant pores located at three or more grain junctions (see Figure 1.1) and it accounts for almost all of the total pore volume. The soft porosity, on the contrary, includes contacts between surfaces of grain faces, and contains only a tiny fraction of the total porosity (about 0.05-1% of the total). The stiff porosity in sandstones is well resolved by micro-CT scanners and the only source for errors associated with the stiff porosity is segmentation and meshing uncertainties. On the other hand, compliant porosity, which can be seen in SEM images (Figure 1.1b), is unresolvable in microtomograms. The reason is that the typical sandstone grain size is about 100 μm and the grain contact with aspect ratios of 10^{-3} would have a width of 0.1 μm, while the resolution of conventional micro-CT scanners is about 1 μm.

The impossibility to resolve soft porosity by conventional micro-CT methods makes quantitative prediction of elastic properties of sandstones a challenging problem as minor variations in the amount and aspect ratio of the compliant porosity lead to substantial changes in elastic compliances of sandstones (e.g., Shapiro, 2003;

Pervukhina et al., 2010). However micro-CT images contain all the necessary information to obtain moduli at high effective stresses as all existing theories accept that soft porosity shows exponential decay with an increase of effective stress and vanishes at stresses higher than 50-60 MPa (e.g., Pervukhina et al., 2010; Shapiro, 2003; Becker et al., 2007). Additionally, the images include information of probable sources of soft porosity at grain contacts, namely, their surface areas and orientation angles.

Soft porosity evaluated from fitting of stress dependency of experimentally measured compressibility (a reciprocal of bulk moduli) of dry rock by method suggested by Pervukhina et al. (2010) is shown in Figure 1.14a. An additional independent proof of the presence of soft porosity at low effective stresses and its closure at higher stresses can be given comparing the experimental moduli measured on the saturated sample with moduli calculated using Gassmann fluid substitution (Gassmann, 1951) obtained from experimentally measured dry moduli (Figure 1.14b). Measured and Gassmann-computed saturated moduli are in a good agreement at high stresses, but show obvious divergence at lower effective stresses. This discrepancy between the moduli at low stresses can be explained by squirt effect (viscous dampening when water fills the cracks) that implies the presence of compliant porosity (Mavko and Jizba, 1991; Gurevich et al., 2009). With increase of effective stress and closure of soft porosity, the squirt effect vanishes and the difference of between the measured bulk moduli and that estimated by Gassmann substitution becomes negligible (within the experimental error).

The procedure developed for image processing, interfacial surface triangulation and simplification, meshing and numerical simulation of elastic properties of rocks can be applied without much change for the analysis of 3D rock microstructure data obtained by Scanning Electron Microscope (SEM) combined with Focused Ion Beam (FIB) technology (e.g., Drury *and* Fitz Gerald, 1996; Matthijs de Winter et al., 2009) or other emerging techniques that increase the resolution down to nanometre scale. By employing such high-resolution techniques, numerical prediction of elastic properties might be possible at different confining stresses even with complex particle contacts. Further improvements can also come from the application of multi-energy data acquisition and processing (e.g., Shikhaliev, 2008; Yang et al., 2010; Qi et al., 2010) which allows clear

differentiation between grains with different mineralogy that would otherwise be lumped into a single "phase" in a single-energy tomogram. The segmentation of solid phase into the true mineral distribution then becomes possible and different elastic moduli can be attributed explicitly to individual grains instead of the use of the SCA to calculate effective elastic moduli of and averaged solid phase.

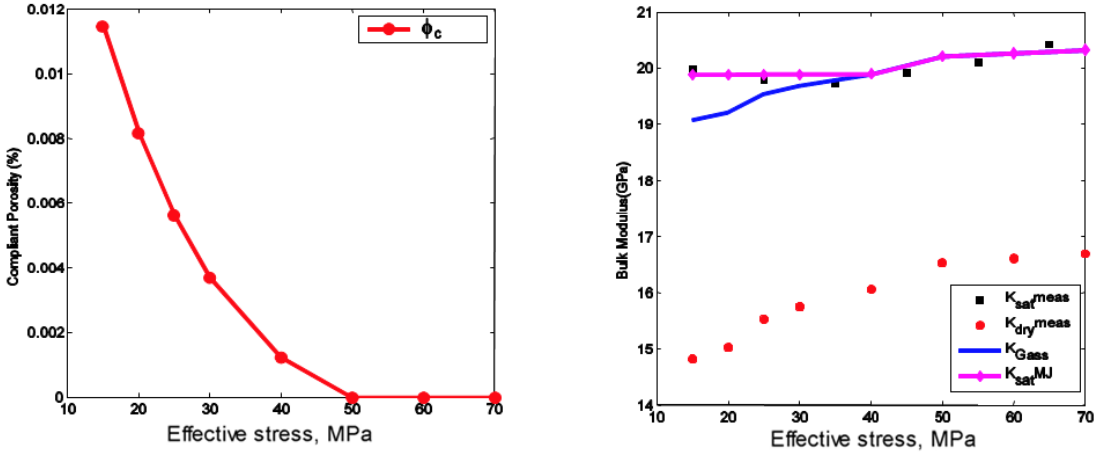

(a) (b)

Figure 1.14 Illustration of existence of soft porosity in Donnybrook sandstone: (a) soft porosity calculated from stress dependency of bulk modulus shows exponential decay and almost vanishes at 50 MPa; (b) Experimentally measured saturated bulk moduli in comparison with bulk moduli calculated using Gassmann fluid substitution equation from dry moduli at different effective stresses. Two saturated moduli show obvious difference at low effective stresses and are in a good agreement at higher stresses.

It is also noteworthy that our computational approach can be readily extended in various directions. The algorithms already used can be scaled up to allow for much larger simulation sizes, given sufficient computational power (e.g., GPU cluster), allowing larger rock volumes and/or higher resolution datasets to be tackled. We have not fully explored the capabilities of available adaptive grids algorithms. This becomes a crucial step if the modelling domain increases or other fields are simultaneously computed. For example, effective poroelastic rock behaviour of fluid-saturated rocks are of interest but require finer meshing in order to resolve fluid pressure diffusion processes (e.g., Wenzlau and Müller, 2009; Wenzlau et al., 2010). With adaptive meshing this complexity can be included without change in the overall numerical setup.

1.6 CHAPTER CONCLUSIONS

We have developed a comprehensive digital rock physics workflow including 3D imaging, processing and finite-element simulations of physical experiments with the focus on the numerical up-scaling of elastic moduli. As an example, the effective elastic bulk and shear moduli of a Donnybrook sandstone sample are numerically simulated using microtomograms. The simulated and measured elastic moduli are in a good agreement at the effective stress of about 50 MPa, which is the stress level where microcracks become effectively closed. We conclude that the computational elastic up-scaling approach yields physically consistent effective moduli for this rock microstructure, which is typical of many consolidated reservoir sandstones and aquifers. The grains are mainly quartz and feldspars with some clay and a moderate porosity and permeability is exhibited. To account for sub-resolution features, either theoretical or additional computational approaches need to be employed. Further research along these lines is also required to account for the full range of frequency and stress-dependent behaviour observed.

CHAPTER 2 – EXPERIMENTAL VERIFICATION OF THE PHYSICAL NATURE OF VELOCITY-STRESS RELATIONSHIP FOR ISOTROPIC POROUS ROCKS

The exponential increase of seismic velocities with effective stress has usually been explained by the presence of pores with a broad distribution of aspect ratios. More recently, a stress-related closure of soft pores with a narrow distribution of compliances (e.g., grain contacts) has been suggested to be sufficient to explain such exponential stress dependency. Here we verify this theoretical interpretation using laboratory measurements on dry sandstones. Based on the experimental data, linear dependency of elastic compressibility on soft porosity and exponential decay of soft porosity and elastic compressibility with effective stress up to 60 MPa is confirmed. Soft porosity, estimated from the fitting coefficients of elastic compressibilities, is on the same order of magnitude but slightly lower than obtained from strain measurements. The results confirm applicability of previously proposed stress sensitivity models and provide justification for using this approach to model stress dependency of elastic properties for isotropic and anisotropic rocks.

In this chapter, I used the material published in the following extended abstract with permission from leading co-authors:

> Pervukhina M., Gurevich B., Dewhurst D. N., Siggins A. F., Golodoniuc P., and Fortin J., 2010, Experimental verification of the physical nature of velocity-stress relationship for isotropic porous rocks: ASEG Extended Abstract at the 21st International Geophysical Conference and Exhibition (ASEG-PESA), Sydney, Australia.

2.1 INTRODUCTION

Knowledge of stress dependency of elastic properties of rocks is important for a variety of geophysical applications ranging from pore pressure prediction in sedimentary rocks and seismic monitoring of hydrocarbon production to constraining material properties in the mantle. It has been shown by many authors that stress dependency of compressional and shear velocity V in many dry porous rocks can be well approximated by a combination of linear and exponential terms (e.g., Zimmerman et al., 1991; Eberhart-Phillips et al., 1989):

$$V(P) = A + KP - B\exp(-PD), \tag{2.1}$$

where P is confining pressure, A, K, B, and D are fitting parameters that provide the best agreement with the measured data.

The exponential term in equation (2.1) is usually explained by presence of pores and cracks with a broad (often exponential) distribution of crack stiffnesses or aspect ratios. An attempt to explain the nonlinearity with cracks of similar shape was done by Mavko and Nur (1978) and resulted in polynomial strain vs. stress dependency and specific shape of non-elliptical cracks. Recently, Shapiro (2003) obtained a result that such exponential saturated to linear form may be explained by much more simple and physically plausible dual distribution of porosity. More precisely, Shapiro (2003) showed that if total porosity ϕ of an isotropic rock can be divided into stiff porosity part ϕ_s and much more compliant part ϕ_c, i.e.:

$$\phi = \phi_s + \phi_c \tag{2.2}$$

then dry rock compressibility C_{dr} can be written as a simple linear function of stiff and compliant porosities:

$$C_{dr}(P) = C_{drs}\left(1 + \theta_s \Delta\phi_s + \theta_c \phi_c\right) \tag{2.3}$$

Here C_{drs} is the compressibility of the porous rock with all compliant porosity closed (hereafter, stiff limit), θ_s and $\theta_c >> \theta_s$ are coefficients related to compliance of stiff and compliant pores, respectively, $\Delta\phi_s = \phi_s - \phi_{s0}$ is the deviation of the stiff porosity from its zero-pressure value ϕ_{s0}. Compliant porosity ϕ_c and $\Delta\phi_s$ are assumed as low as 10% or less (Shapiro, 2003) to satisfy the assumption of linear variation of compressibility with porosity and independent in a sense that closure of ϕ_c does not affect θ_s and vice versa. Note a change in notation: $\Delta\phi_s$ in the present work corresponds to ϕ_s in Shapiro (2003).

In many cases, $\theta_s \Delta\phi_s << \theta_c \phi_c$ and equation (2.3) reduces to:

$$C_{dr}(P) = C_{drs}\left(1 + \theta_c \phi_c\right) \tag{2.4}$$

Variations of stiff and soft porosity with pressure have the form:

$$\Delta\phi_s = P\left[C_{gr} - (1-\phi_{s0})C_{drs}\right] \tag{2.5}$$

and

$$\phi_c = \phi_{c0}\exp(-\theta_c C_{drs} P) \tag{2.6}$$

where C_{gr} is the compressibility of the solid grain material and ϕ_{c0} is the compliant porosity at zero pressure. Equation (2.5) is slightly more general than the form used by Shapiro (2003), as it does not require initial stiff porosity ϕ_{s0} to be small. Substituting expression (2.6) for compliant porosity into equation (2.4) gives the variation of compressibility with pressure $\Delta C_{dr}(P) = C_{dr}(P) - C_{drs}$ in the form:

$$\Delta C_{dr}(P) = C_{drs}\theta_c\phi_{c0}\exp(-\theta_c C_{drs} P) \tag{2.7}$$

If this variation is small ($\Delta C_{dr}(P) << C_{drs}$), then equation (2.3) together with the corresponding equation for the shear compliance yields equations similar in form to (2.1) for the bulk and shear moduli and for compressional and shear velocities of the dry rock (Shapiro, 2003). The moduli and velocities of saturated rocks (at low frequencies) can be obtained using Gassmann equations; in this case pressure *P* has the meaning of effective pressure.

The stress sensitivity theory of Shapiro (2003) was extended to anisotropic rocks by Shapiro and Kaselow (2005). A number of studies use the theory to describe behaviour of various isotropic and anisotropic rocks, for instance, Becker et al., (2007), Pervukhina et al. (2008a), Pervukhina et al. (2008b), Liu et al. (2008) and De Paula et al. (2008).

While the stress sensitivity approach of Shapiro (2003) provides an appealingly simple interpretation of equation (2.1) and the existence of compliant porosity has been reported by many authors, it is not yet widely accepted, partly due to the lack of the experimental verifications of this interpretation. The main difficulty in such experimental verification lies in the fact that, in most cases, the velocity-stress relationship is obtained through ultrasonic experiments where variation of porosity with stress is not simultaneously measured.

In this chapter, we overcome this difficulty by using simultaneous measurements of ultrasonic velocity and porosity in a high-pressure cell. Porosity variations are estimated from measurements of axial strain. The results of our analysis for the sandstone samples used in the experiments are consistent with the physical interpretation of Shapiro (2003).

2.2 WORKFLOW

Our workflow consists of three main parts: laboratory measurements, computation of the key parameters, and analysis.

2.2.1 EXPERIMENT

The experimental program involves the following steps:

1. Measure compressional V_p and shear V_s velocities for a dry sample as a function of isotropic confining pressure P.
2. Simultaneously measure axial strain ε_{ax} as a function of pressure.
3. Measure initial porosity at zero pressure ϕ_0 and/or initial density ρ_0.

2.2.2 CALCULATIONS OF KEY PARAMETERS

Once these data are measured, compressibilities plus stiff and soft porosities are obtained as follows:

1. For each pressure, the dry bulk modulus K_{dr} is obtained using the standard equation $K_{dr} = \left[V_P^2 - (4/3)V_S^2\right]\rho_0$ and compressibility as $C_{dr} = K_{dr}^{-1}$. Note that accuracy of the calculation of the bulk modulus using initial density ρ_0 at $P = 0$ should be checked for a particular rock since the introduced error might be sufficient for a compliant rock. In the case of our samples, we have estimated density perturbations from axial strain measurements assuming that

all deformations are isotropic and found that the error caused by use of the initial density ρ_0 is less than 0.4%.

2. We then compute variation of porosity with pressure. Since experiments are performed with hydrostatic pressure, we assume that ε_{ax} represents the strain in all three directions. Then, the volumetric strain (relative variation of the sample volume v with pressure) is $\varepsilon = (v - v_0)/v_0 = 3\varepsilon_{ax}$, where v_0 is sample volume at zero pressure. At the same time, the relative change of total volume v_{gr} of solid grains with pressure is $\varepsilon_{gr} = (v_{gr} - v_{gr0})/v_{gr0} = -C_{gr}P/(1-\phi)$, where v_{gr0} is total volume of solid grains at zero pressure and C_{gr} is the compressibility of the solid grain material, which is assumed known from mineralogical analysis. Since pore volume at any pressure is the total volume minus grain volume, $v_\phi = v - v_{gr}$, using Zimmerman *et al.* (1986), we get:

$$\phi = \frac{v_\phi}{v} = 1 - \frac{v_{gr}}{v} = 1 - \frac{\left[1 - C_{gr}P/(1-\phi)\right]v_{gr0}}{(1+\varepsilon)v_0} \tag{2.8}$$

For small deformations, this gives:

$$\phi = 1 - (1-\varepsilon)(1-\phi_0) - C_{gr}P = \phi_0 + (1-\phi_0)\varepsilon + C_{gr}P \tag{2.9}$$

Note that for $P > 0$, total volumetric strain, ε, is negative, and is larger in absolute value than the grain deformation $C_{gr}P$; therefore, using (2.9), porosity will decrease with increasing pressure, as it should.

3. Now we have to define the parameters, which we called stiff and soft porosities. Since stiffness of pores is a relative measure, there is some freedom inherent in this distinction. One way to define stiff porosity is to assume that within the pressure range of measurements, say from 0-100 MPa, the stiff porosity changes linearly with pressure. Indeed, if measured

compressibilities and velocities can be described by a simple exponential relationship of the type given by equation (2.4), then at large pressures the compressibility C_{dr} approaches a constant value C_{drs}. Constant compressibility corresponds to a linear variation of the strain with pressure. Indeed, in a pressure interval where dry compressibility is approximately constant, $C_{dr} \approx C_{drs}$, volumetric strain $\varepsilon = -C_{dr}P$ and equation (2.8) gives a linear relationship between porosity and pressure. This linear porosity trend is expected in the upper part of our pressure range, where all soft pores can be assumed closed. We can thus call this part of the porosity the stiff porosity. Assuming, following Shapiro (2003), that stiff and soft porosity variations are independent of one another, we can extrapolate this stiff porosity trend to lower pressures. In practice, we will estimate stiff porosity by fitting a linear trend to the porosity-pressure dependency in the uppermost part of the measurement pressure range (Walsh, 1965; Mavko and Jizba, 1991).

4. Once stiff porosity is defined, the compliant (soft) porosity is defined by equation (2.2) as the difference between total and stiff porosity. We will also obtain soft porosity from a non-linear fitting of experimentally measured $\Delta C_{dr}(P)$ as a ratio of the coefficient before the exponential to the exponent as predicted by equation (2.7). Hereafter, we refer to the former and latter soft porosity as measured and predicted, respectively.

We fitted experimentally measured compressibilities $C_{dr}(P) = C_{drs} + C_{drs}\theta_c\phi_{c0}\exp(-\theta_c C_{drs}P)$ to get the best fit values of the stiff limit C_{drs} and then calculated $\Delta C_{dr}(P) = C_{dr}(P) - C_{drs}$.

2.2.3 TESTING THEORETICAL PREDICTIONS

With equations (2.2) and (2.5) used effectively as definitions, we will test experimentally the following elements of Shapiro's (2003) stress sensitivity theory:

1. Test the adequacy of the linear relationship (2.4) between the dry compliance and soft porosity.

2. Test the adequacy of the exponential approximation, equation (2.6), for the soft porosity.
3. Compare the exponent $\theta_c C_{drs}$ in the soft porosity fit, equation (2.6), with the same exponent in the ΔC_{dr} fit, equation (2.7), hereafter, λ_ϕ and λ_C, respectively.
4. Compare the measured against predicted soft porosity.
5. Compare the two stress sensitivity coefficients appearing in equation (2.7). The coefficient θ_{dyn} obtained from the proportionality constant is called dynamic because it is derived from the measurements of ultrasonic velocities. In contrast, the coefficient in the exponent θ_{st}, which describes variation of soft porosity with pressure, is called static. In deriving these values from the corresponding fits (linear fit of ΔC_{dr} versus ϕ_c and exponential fit for ΔC_{dr} versus pressure) we assume that high-stress compressibility C_{drs} is the same in both instances.

2.3 DATA

We used reservoir sandstone core samples from the Northwest Shelf of Australia between depths of 1700-2000 metres (Siggins and Dewhurst, 2003) to validate the stress dependency model. The other sample we used in our research is a cylindrical specimen of 80 mm in length and 40 mm in diameter that was prepared from Bleurswiller Sandstone, which was collected from a quarry in Frain (Vosges, eastern France). The experimental procedure and results were published in Fortin et al. (2007). We calculate elastic compressibilities using longitudinal and shear velocities in the dry samples. Porosity variations are obtained from changes in the length of the cylindrical samples.

Total, stiff and compliant porosity are shown in Figure 2.1 for the Bleurswiller Sandstone sample for loading phase. As outlined above, stiff porosity (solid line) is obtained by linear extrapolation of the high-stress trend determined from two points at 60 and 65 MPa. Compliant porosity (open circles) is estimated by subtracting stiff porosity from the total porosity and is reasonably approximated by an exponential fit (dashed line). The total porosity is shown as solid circles.

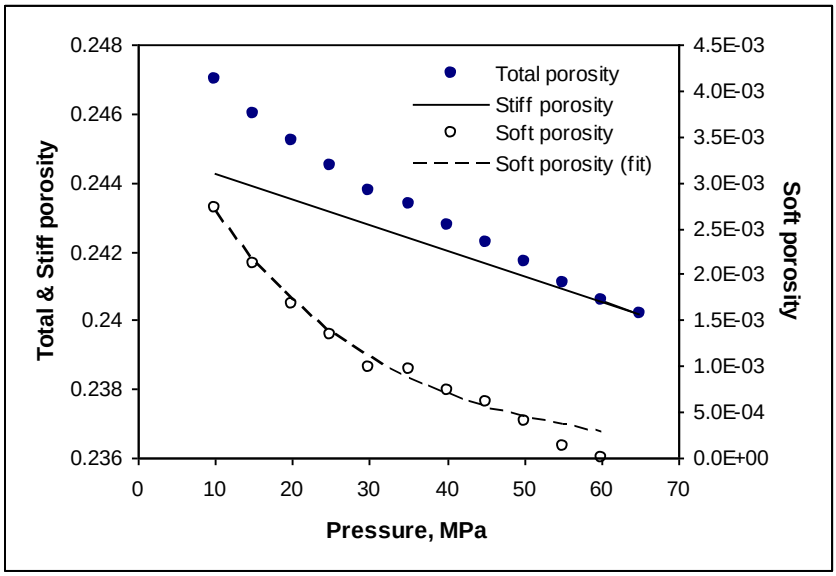

Figure 2.1 Total, stiff and compliant porosities.

2.4 RESULTS

In Figures 2.2 and 2.3, we illustrate tests of the stress sensitivity theory for the Bleurswiller sandstone and then show test results on all samples (Figure 2.4). The test of linearity of the relationship between compressibility and soft porosity (equation 2.4) is demonstrated in Figure 2.2, which shows pressure variation of compressibility $\Delta C_{dr}(P)$ as a function of compliant porosity and its linear fit for the loading limb. The square of the Pearson product moment correlation coefficients R^2 is 0.99 indicating a very good correlation between $\Delta C_{dr}(P)$ and $\phi_c(P)$.

Measured stress dependencies of variations of elastic compressibility ΔC_{dr} and compliant porosity ϕ_c with stress for the same sample are presented in logarithmic scale in Figure 2.3. Straight solid and dashed lines show linear fits of the compressibility deviation $\Delta C_{dr}(P)$ and compliant porosity $\phi_c(P)$, respectively. Those linear fits are nearly parallel, which confirms that compressibility variation and soft porosity are well approximated by the same exponentials.

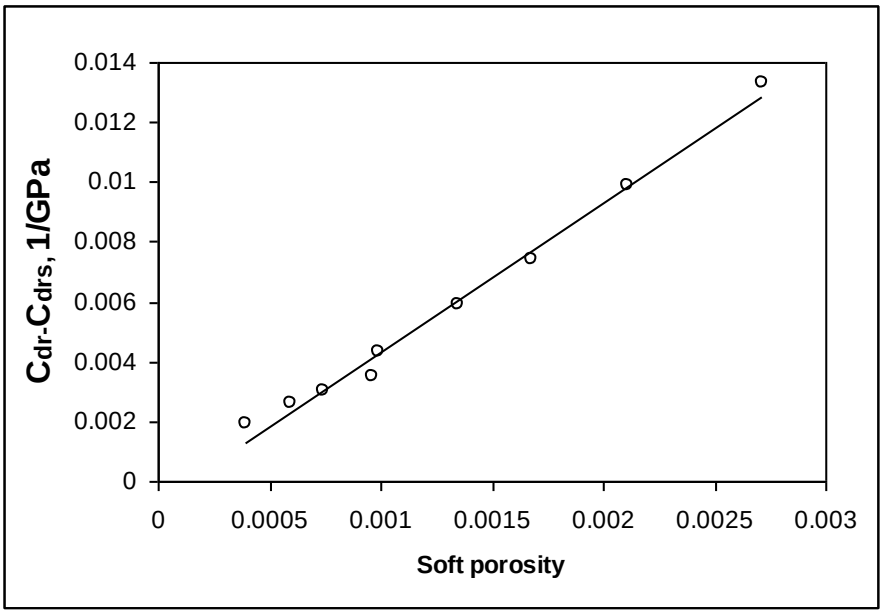

Figure 2.2 Linear dependency of variation of compressibility with soft porosity.

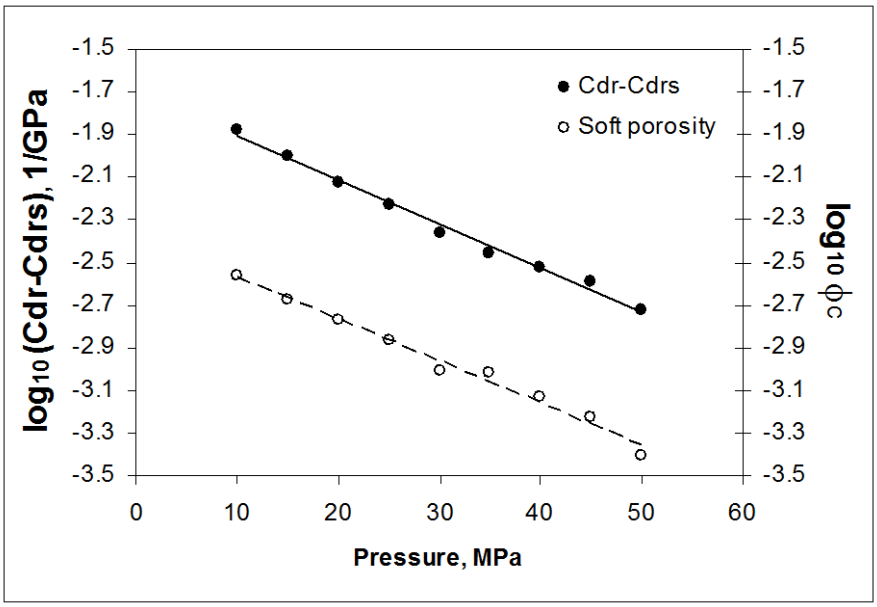

Figure 2.3 Pressure dependency of compressibility and soft porosity with pressure.

The predicted soft porosities shown in Figure 2.4 in comparison with measured ones are of the same order of magnitude but somewhat lower. The predicted vs. measured soft porosity trends are $\theta_{pr} = 0.74\theta_m$ and $\theta_{pr} = 0.84\theta_m$ for loading and unloading, respectively, indicating a better prediction of the soft porosity from the measured compressibility data during unloading.

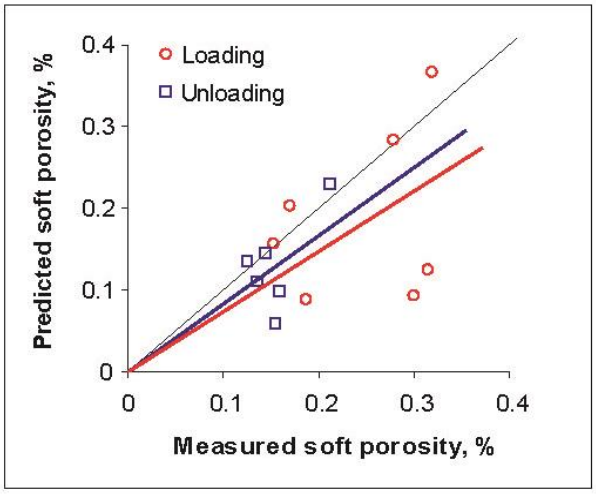

Figure 2.4 Correlation between predicted and measured soft porosities.

2.5 CHAPTER CONCLUSIONS

Theoretical interpretation of exponential stress dependency of elastic properties of rocks based on a dual porosity concept has been tested using laboratory measurements on dry sandstones. For those sandstone samples, the following postulates of the theoretical model are shown to work well: (1) linear dependency of elastic compressibility on soft porosity and (2) exponential decay of soft porosity and elastic compressibility with effective stress up to 60 MPa. The magnitude of the variation of stiff porosity with stress is shown to be comparable with compliant porosity. However, this variation has a negligible effect on rock compressibility up to 60 MPa. Soft porosity estimated from the fitting coefficients of the elastic compressibilities is on the same order of magnitude but slightly lower than obtained from strain measurements. These results confirm the applicability of Shapiro's (2003) stress sensitivity model and hence provide justification for using this approach to model the effect of stress on properties of both isotropic and anisotropic rocks.

CHAPTER 3 – PARAMETERIZATION OF ELASTIC STRESS SENSITIVITY IN SHALES

Stress dependency and anisotropy of dynamic elastic properties of shales is important for a number of geophysical applications, including seismic interpretation, fluid identification and 4D seismic monitoring. Using Sayers-Kachanov formalism, we develop a new model for transversely isotropic (TI) media, which describes stress sensitivity behaviour of all five elastic coefficients using four physically meaningful parameters. The model is used to parameterize elastic properties of about 20 shales obtained from laboratory measurements and from the literature. The four fitting parameters, namely, specific tangential compliance of a single crack, ratio of normal to tangential compliances, characteristic pressure and crack orientation anisotropy parameter show moderate to good correlations with the depth from which the shale was extracted. With increasing depth, the tangential compliance exponentially decreases. The crack orientation anisotropy parameter broadly increases with depth for most of the shales, indicating that cracks are getting more aligned in the bedding plane. The ratio of normal to shear compliance and characteristic pressure decreases with depth to 2500 m and then increases below this to 3600 m. The proposed model allows evaluation of the stress dependency of all five elastic compliances of a TI medium, even if only some of them are known. This may allow the reconstruction of the stress dependency of all five elastic compliances of a shale from log data for example.

This chapter is based on the published version of the following journal publication with permission from co-authors and publishers (see Appendix B):

Pervukhina M., Gurevich B., Golodoniuc P., and Dewhurst D. N., 2011, Parameterization of elastic stress sensitivity in shales: Geophysics, **76(3)**, p. WA147–WA155, doi:10.1190/1.3554401.

3.1 INTRODUCTION

Shales are the most common rock type encountered in sedimentary basins. Due to their strongly anisotropic properties, the presence of shales in the subsurface may cause significant errors in depth obtained from surface seismic data, in normal moveout (NMO) correction, dip moveout correction (DMO), migration and amplitude versus offset analysis (e.g., Castagna et al., 1993; Banik, 1984; Sayers, 1999; Tsvankin et al., 2009). Seismic anisotropy of shales is caused by a number of factors, including intrinsic anisotropy of clay minerals that are abundant in shales, preferred orientation of clay platelets, alignment of thin flat pores, and kerogen inclusions (e.g., Hornby et al., 1994; Johnston and Christensen, 1995; Sayers, 1999).

Various studies have addressed the problem of prediction of shale anisotropy, which requires values of the five elastic stiffness coefficients required to describe a transversely isotropic (TI) medium and Thomsen's anisotropy parameters (Thomsen, 1986). Johnston and Christensen (1995) reported a strong positive correlation between seismic anisotropy and so-called orientation indices that reflected clay mineral alignment. Johansen et al. (2004) studied the effect of alignment of grain scale texture on seismic anisotropy and reflectivity of shales. Sayers (2005) related the clay platelet orientation distribution to the behaviour of Thomsen's δ parameter, which is the only anisotropy parameter needed to interpret the small-offset amplitude variation with offset (AVO) response. Using self-consistent approximation (SCA) effective media theory, Hornby et al. (1994) reconstruct the TI elastic tensor of the Greenhorn Shale on the basis of the knowledge of clay platelet orientation distribution and silt inclusion fraction, assuming knowledge of clay elastic properties. All these previous studies required knowledge of detailed microstructure and assume that anisotropic the elastic moduli of individual clay minerals are known. However, the clay platelet orientation characteristics, which require thorough quantitative image analysis, can vary from sample to sample even for shale samples acquired just a few meters apart. In addition, elastic properties of clay minerals reported in the literature range in value by more than an order of magnitude (e.g., Aleksandrov and Ryzhova, 1961; Woeber et al., 1963; Han et al., 1986; Castagna et al., 1993; Hornby et al., 1994; Katahara, 1996; Vanorio et al., 2003; Ortega et al., 2007) and depend on a number of parameters such as clay mineralogy, water content and sample preservation.

Recently, Ulm and Abousleiman (2006) suggested a simple model that allows prediction of anisotropic elastic moduli of shales. This model implies that shale elastic properties are independent of clay mineralogy and allows prediction of elastic moduli on the basis of only two parameters, namely, silt fraction and clay packing density (CPD), a volumetric fraction of clay minerals in wet shale without silt inclusions. Using this model in combination with the SCA approach, Ulm and Abousleiman (2006) estimated elastic moduli of clay minerals from measurements of elastic properties of a number of shales. Bayuk et al. (2007) used the general singular approximation (GSA) effective media approach to estimate the elasticity tensor of clay minerals from experimentally measured elastic properties of the Greenhorn Shale used in Hornby's study (Hornby et al., 1994). The approach of Ulm and Abousleiman (2006) and Bayuk et al. (2007) was further refined by Pervukhina et al. (2008a, 2008b) who suggested using a differential effective media (DEM) approach as the most relevant for shale microstructure. The suggested method works quite well for predicting anisotropic elastic moduli of shales based on CPD and silt fraction. However, it fails to predict stress dependency of elastic properties of shales (Pervukhina et al., 2008a, 2008b), which has been observed in many experiments (e.g., Jakobsen and Johansen, 2000; Dewhurst and Siggins, 2006; Kuila et al., 2010; Delle Piane et al., 2010).

The problem of stress dependency of shale properties is important for such applications as pore pressure prediction, or time lapse seismic monitoring. Despite this, there is no widely accepted theory for stress dependency of elastic properties of shales. Sayers (1999) studied stress dependencies of air-dry and fluid-saturated shales using the Sayers and Kachanov (1995) excess compliance approach and obtained ratios of normal to tangential compliances of clay platelet contacts for the both cases, assuming the contacts were well aligned. Prioul et al. (2004) and Prioul and Lebrat (2004) described the stress dependency of shales using a model based on non-linear elasticity with three stress-sensitive (nonlinear) parameters, although this model is suitable only for a stress range where stiffnesses are quasi-linear with stress. Shapiro and Kaselow (2005) suggested a stress dependency model for orthorhombic media based on a dual porosity approach. Their model is based on the bimodal distribution of pore compliances and superposition of deformation fields caused by closure/shape change of these two groups of soft and stiff pores under applied stress.

Ciz and Shapiro (2009) used this approach to build a model of experimental shale measurements from the North Sea previously reported by Hornby (1998) and showed a good model fit to the measurements. However in the isotropic limit, the model of Ciz and Shapiro (2009) has been shown to be equivalent to the isotropic version of the model of Sayers (1999) with exponential dependency of excess compliances on pressure and with an additional assumption that normal and tangential compliances of each grain contact are equal (Gurevich et al., 2009). This assumption may not be physically adequate, especially for water-saturated rocks at ultrasonic frequencies, since water in intergranular pores and microfractures should strongly reduce normal, but not tangential, compliance.

Herein, a new model is proposed that allows description of stress dependency of all five elastic coefficients of TI shales by treating both the orientation distribution of clay platelets and the compliance ratio of platelet contacts as model parameters. To this end, we combine the dual porosity approach of Shapiro and Kaselow (2005) with the non-interactive approximation of Sayers and Kachanov (1995).

3.2 MODELLING OF THE EFFECT OF ISOTROPIC STRESS ON THE ANISOTROPIC ORIENTATION OF DISCONTINUITIES

Following Shapiro (2003), Shapiro and Kaselow (2005) and Ciz and Shapiro (2009), we assume that variation of elastic properties of a shale subjected to effective confining pressures of up to 60 MPa can be explained by closure of soft (compliant) porosity. Soft porosity comprises a small part of total porosity and consists of pores with high compliances, such as fractures, cracks and grain or clay platelet contacts. Figure 3.1 shows an SEM image, which illustrates existence of both stiff and compliant pores in shales.

We model shale as an intrinsically transversely isotropic medium that is permeated with discontinuities such as grain or platelet contacts, cracks or fractures, which are distributed anisotropically. We assume that the probability density for a particular orientation can be written as:

$$W(\theta,\phi)=\frac{1+\eta\cos^2\theta}{\int_0^{2\pi}\int_0^{\pi}\left(1+\eta\cos^2\theta\right)\sin\theta d\theta d\phi}=\frac{1+\eta\cos^2\theta}{4\pi\left(1+\eta/3\right)} \tag{3.1}$$

where θ is an angle between the z-axis and the normal to the crack surface (range [0, π]), ϕ determines the rotation about the z-axis (range [0, 2π]) and η is the crack orientation anisotropy parameter. Isotropic distribution of cracks corresponds to the case when $\eta = 0$ and in the case when η is large, there is a strong alignment of cracks. One can check that the probability density defined by equation 3.1 satisfies the normalization condition:

$$\int_0^{2\pi} \int_0^{\pi} W(\theta, \phi) \sin\theta d\theta d\phi = 1 \tag{3.2}$$

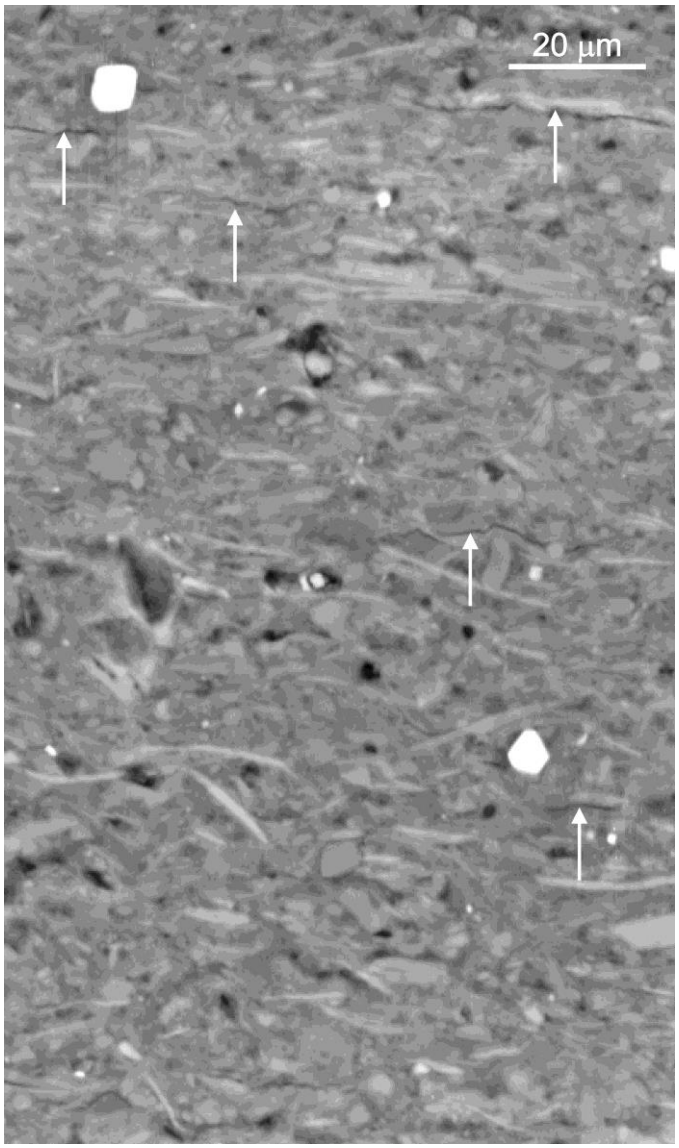

Figure 3.1 An Officer Basin shale showing particle alignment and the presence of microfractures (white arrows). Modified from Kuila et al. (2010).

The exact geometry of individual cracks is not specified. Instead, the behaviour of cracks is defined by B_T, the specific tangential compliance (tangential compliance of a crack with a unit surface area) and a ratio $B = B_N / B_T$ where B_N is specific normal compliance. For parameterization purposes, only effective properties are important, so the surface area A and the compliance ratio B are assumed to be the same for all cracks. We assume that B_N and B_T are independent of cracks orientation and do not change with stress (for analysis of this assumption for isotropic rocks, see Pervukhina et al., 2010). Following Schoenberg (2002), Shapiro (2003) and Shapiro and Kaselow (2005), we further assume that the surface area of individual cracks decreases with stress exponentially. Therefore, a specific surface area per unit volume $s_0 = N_0 A$ also varies exponentially with stress, such that:

$$s(P) = N_0 A^0 \exp(-P / P_c) \tag{3.3}$$

where N_0 is the total number of cracks integrated over all angles, A^0 is the specific surface area of an individual crack at zero stress, P is effective stress and P_c is a characteristic crack closing pressure.

When a rock with this distribution of discontinuities is subjected to a small compressive isotropic stress, the density of cracks along a particular plane is assumed to be reduced exponentially with the normal stress traction acting on that plane. The area of the cracks in the case of their anisotropic distribution will reduce differently in different directions. An effect of this anisotropic variation of the crack areas on elastic properties can be modelled using the Sayers and Kachanov (1995) non-interactive approximation:

$$\Delta S_{ijkl} \equiv S_{ijkl} - S^0_{ijkl} = \frac{1}{4}\left(\delta_{ik}\alpha_{jl} + \delta_{il}\alpha_{jk} + \delta_{jk}\alpha_{il} + \delta_{jl}\alpha_{ik}\right) + \beta_{ijkl} \tag{3.4}$$

$$\alpha_{ij} = \frac{1}{V}\sum_r B_T^{(r)} n_i^{(r)} n_j^{(r)} A^{(r)} \tag{3.5}$$

$$\beta_{ijkl} = \frac{1}{V}\sum_r \left(B_N^{(r)} - B_T^{(r)}\right) n_i^{(r)} n_j^{(r)} n_k^{(r)} n_l^{(r)} A^{(r)} \tag{3.6}$$

Here, ΔS_{ijkl} is the excess compliance caused by the presence of compliant cracks, S^0_{ijkl} are compliances at high stress with all soft cracks closed and S_{ijkl} are the compliances at some intermediate stress; δ_{ij} is the Kronecker delta; r is the number of planar discontinuities with surface area $A^{(r)}$ and $n_i^{(r)}$ and $n_j^{(r)}$ are i-th and j-th components of the unit vector that is normal to the surface of the r^{th} grain boundary in volume V; finally, B_N and B_T are the normal and tangential compliances of an individual crack.

Substituting equations 3.1 and 3.3 into equations 3.4-3.6, we obtain variation in compliances due to the closure of discontinuities at different pressures as follows:

$$\Delta S_{11} \equiv S_{11} - S^0_{11} = \frac{s_n B_T \exp\left(-P/P_c\right)}{105}\left(14 + 4\eta + 21B + 3B\eta\right) \tag{3.7}$$

$$\Delta S_{33} \equiv S_{33} - S^0_{33} = \frac{s_n B_T \exp\left(-P/P_c\right)}{105}\left(14 + 6\eta + 21B + 15B\eta\right) \tag{3.8}$$

$$\Delta S_{44} \equiv S_{44} - S^0_{44} = \frac{s_n B_T \exp\left(-P/P_c\right)}{105}\left(42 + 16\eta + 28B + 12B\eta\right) \tag{3.9}$$

$$\Delta S_{66} \equiv S_{66} - S^0_{66} = \frac{s_n B_T \exp\left(-P/P_c\right)}{105}\left(42 + 10\eta + 28B + 4B\eta\right) \tag{3.10}$$

$$\Delta S_{13} \equiv S_{13} - S^0_{13} = \frac{s_n B_T \exp\left(-P/P_c\right)}{105}\left(7B + 3B\eta - 7 - 3\eta\right). \tag{3.11}$$

Here $s_n = s/\left[4\pi\left(1+\eta/3\right)\right]$ and $s = N_0 A^0$ is the specific surface area of cracks per unit volume. The detailed derivation of equations 3.7-3.11 is given in Appendix A. Note that shales exhibit TI anisotropy and five independent elastic compliances $S_{11}{}^0$, $S_{33}{}^0$, $S_{44}{}^0$, $S_{66}{}^0$ and $S_{13}{}^0$ are required even at high effect stresses when all compliant cracks are supposed to be closed. Such intrinsic anisotropy is caused by anisotropic individual clay mineral moduli and preferential orientation of domains of aggregated clay minerals. If we assume $B_N = B_T$, then equations 3.7-3.11 can be simplified as follows:

$$\Delta S_{11} \equiv S_{11} - S_{11}^0 = \frac{s_n B_T \exp\left(-P/P_c\right)}{15}\left(5+\eta\right) \tag{3.12}$$

$$\Delta S_{33} \equiv S_{33} - S_{33}^0 = \frac{s_n B_T \exp\left(-P/P_c\right)}{15}\left(5+3\eta\right) \tag{3.13}$$

$$\Delta S_{44} \equiv S_{44} - S_{44}^0 = \frac{s_n B_T \exp\left(-P/P_c\right)}{15}\left(10+4\eta\right) \tag{3.14}$$

$$\Delta S_{66} \equiv S_{66} - S_{66}^0 = \frac{2s_n B_T \exp\left(-P/P_c\right)}{15}\left(5+\eta\right) \tag{3.15}$$

$$\Delta S_{13} \equiv S_{13} - S_{13}^0 = 0\,. \tag{3.16}$$

Thus, to parameterize the stress dependency of shales for the general case, when $B_N \neq B_T$ (i.e. equations 3.7-3.11 above), four parameters are necessary, namely $s_n B_T$, tangential compliance of an individual crack per unit area multiplied by the normalized specific surface area of cracks per unit volume; *B*, the ratio of crack normal to crack tangential compliance; η, the crack orientation anisotropy parameter that characterizes angular crack distribution, and P_c, the characteristic pressure at which compliant pores close. For the case of so-called scalar crack approximation when $B_N = B_T$, three parameters $s_n B_T$, η, P_c are required. Note that the parameters s_n and B_T are coupled and cannot be obtained independently. Hereafter, we refer to $s_n B_T$ as B_T bearing in mind that it is, in fact, multiplied by the normalized specific surface area of cracks per unit volume. Below, we fit experimentally measured stress dependencies of elastic properties of shales using both the general set of equations 3.7-3.11 and the scalar crack approximation (equations 3.12-3.16) and show the uncertainties that are introduced in the latter case.

3.3 DATA

We applied our model to a number of shales from the Officer Basin, Bass Basin, Carnarvon Basin (offshore Australia), Africa and the North Sea (Pervukhina et al., 2008b). The details of the experimental procedure and sample preparation can be found in Dewhurst and Siggins (2006) and Dewhurst et al. (2008a, 2008b). We

also used stress dependencies measured by Wang (2002) on shale samples from Africa, North Sea shales, Gulf Coast shale and hard shales. We used measurements obtained for samples cut parallel and perpendicular to bedding, as application of an isotropic stress would not change the TI symmetry of these samples. All the samples were preserved (prevented from drying) before measurements. All the data were obtained in the experiments with controlled pore pressure. The measurements for shales from the Officer Basin, Bass Basin, Carnarvon Basin, Africa and the North Sea were obtained under a pore pressure of 5 MPa. The pore pressures for other shales are given in Wang (2002).

The shale samples were recovered from depths between 200 and 3604 m and vary in their physical properties and in their mineralogy. Unfortunately, Wang (2002) does not report information about overburden pressure, diagenesis, geological history, clay content and mineralogy of the investigated shales. The depth of origin of the shale samples is the only environmental parameter known for all the shales.

3.4 FITTING PROCEDURE AND TRENDS IN MICROCRACK PROPERTIES

The fitting procedure is schematically shown in Figure 3.2. Compliances calculated from experimentally measured velocities at different isotropic effective stresses are fitted using the sets of equations defined in 3.7-3.11 or 3.12-3.16. The Levenberg-Marquardt method (Moré, 1977) is used for nonlinear fitting of experimentally obtained stress dependencies of the elastic compliances of shales with equations 3.7-3.11 or 3.12-3.16, considering B_T, B, P_c and η as fitting parameters. We first fit the data using the scalar crack approximation in equations 3.12-3.16 and then use the resultant parameters B_T, P_c and η and $B = 1$ as an initial estimate for the general set of equations 3.7-3.11. For the second procedure, we use a condition $B \leq 2$ as a constraint to fit the results.

A histogram of the compliance ratio, B, obtained using equations 3.7-3.11, is shown in Figure 3.3. The values are distributed in three distinct groups, (i) small values less than 0.2, (ii) normal values from 0.7-1.1 and (iii) large values of about 2. Departure from unity is observed even in the group with the values from 0.7 to 1.1. This suggests that the ratio $B = 1$ which corresponds to the model of Ciz and Shapiro (2009) may not be adequate for shales.

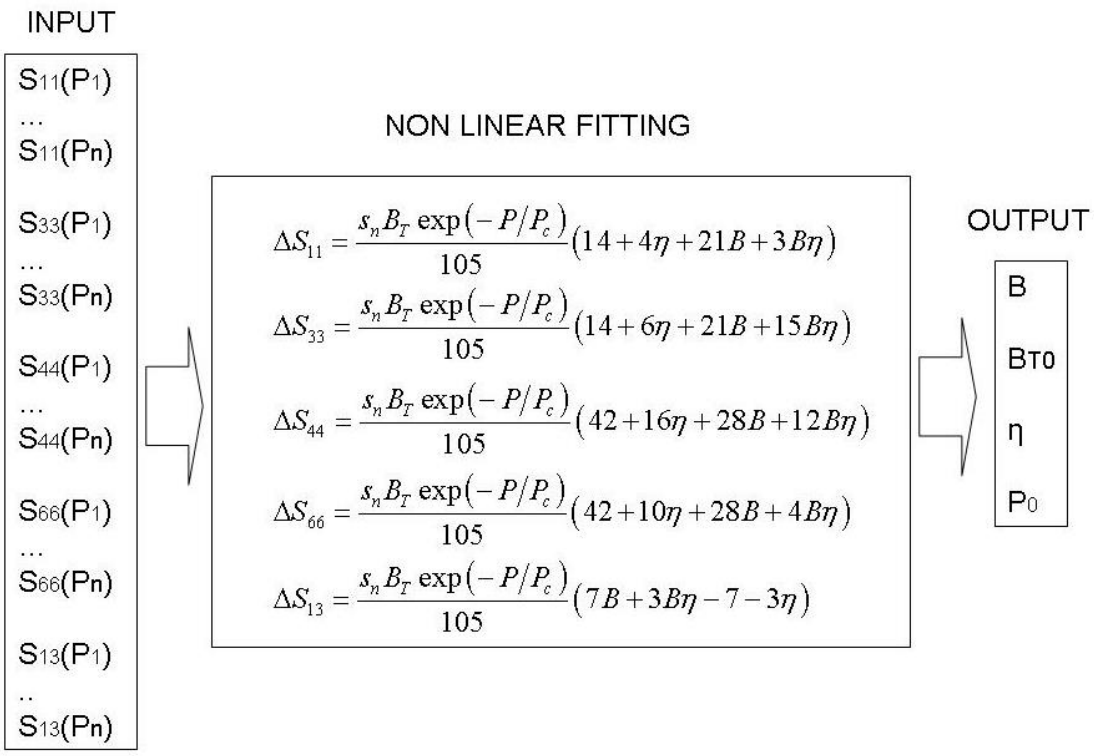

Figure 3.2 Schematic diagram of fitting procedure. Compliances calculated from experimentally measured velocities at different isotropic effective stresses are fitted using a set of equations 3.7-3.11. As a result of the fitting, four fitting parameters are obtained.

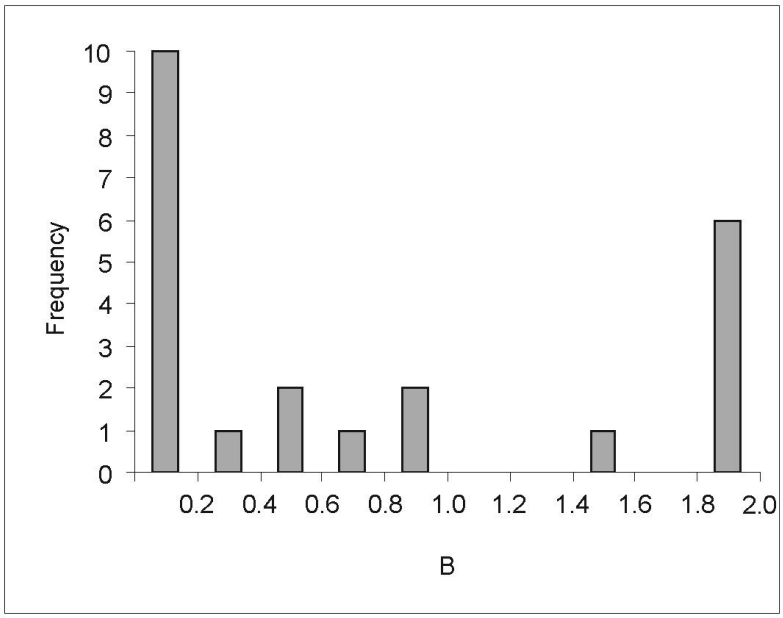

Figure 3.3 Histogram of the ratio of normal to tangential compliance for all the shale samples. Most of the values are far from unity.

To understand the excess in misfit of the experimental stress dependencies caused by the assumption that $B = 1$, we compare the results of the experimental data fitting using equations 3.7-3.11 and 3.12-3.16. The misfits are shown in Figure 3.4a by solid dots (equations 3.7-3.11) and open circles (equations 3.12-3.16). Figure 3.4b shows the relative excess of misfit caused by the assumption that $B_N = B_T$. The relative misfits are close to zero and consequently the misfits are almost the same when B is close to unity. However in other cases, the misfit by equation set 3.12-3.16 noticeably exceeds the one obtained by use of equations 3.7-3.11 (note that the plot in Figure 3.4a is in logarithmic scale). The error caused by use of a scalar crack approximation (equations 3.12-3.16) exceeds the error resulted from fitting with the full set of equations 3.7-3.11 by up to 70%. Similar results were obtained by Angus et al. (2009) who used a synthetic data set to estimate an error caused by usage of a scalar crack approximation instead of the full set of equations. From here onwards, we use only equation set 3.7-3.11 to fit the experimental stress dependencies of elastic properties of shales to avoid additional errors caused by the assumption that $B_N = B_T$.

All four fitting parameters are plotted versus depth of shale extraction in Figure 3.5. Crack orientation anisotropy parameter, η, shows a general linear growth with depth of origin (Figure 3.5a) although there is significant scatter of the fitting values. Higher values of η mean better alignment of the cracks in the bedding plane; consequently, an increase of η with the depth indicates increased alignment of discontinuities with increasing overburden pressure.

Tangential compliance of a single crack normalized to the area of the crack exponentially decreases with depth (Figure 3.5b). This implies that cracks are stiffer in shales that are recovered from greater depths than in the shales extracted from shallower depths.

The ratio of normal to tangential compliance initially decreases from 1 to 0.1 with the increase of depth from 1000 to 2500 m (Figure 3.5c), implying that normal stiffness of shales grows faster with the overburden pressure than the tangential one. Then B increases again reaching 2 at the depth of 3500 m. In other words, in the depth range of 1000-2500 m, cracks become relatively stiffer in the plane of the crack than in the normal direction with increasing depth. However, below 2500 m, the reverse seems to occur. While it is commonly accepted that individual shales can

become stiffer and more anisotropic with depth, this variation of the ratio of normal to tangential compliance is a new finding that has yet to be explained.

The characteristic pressure, P_c, shows no obvious trend with the depth of origin (Figure 3.5d). P_c is equal to ~20 MPa for the shallow (less than 1500 m) and deep (more than 2500 m) depth. For the intermediate depth of 1500-2500 m, P_c drops to 10 MPa.

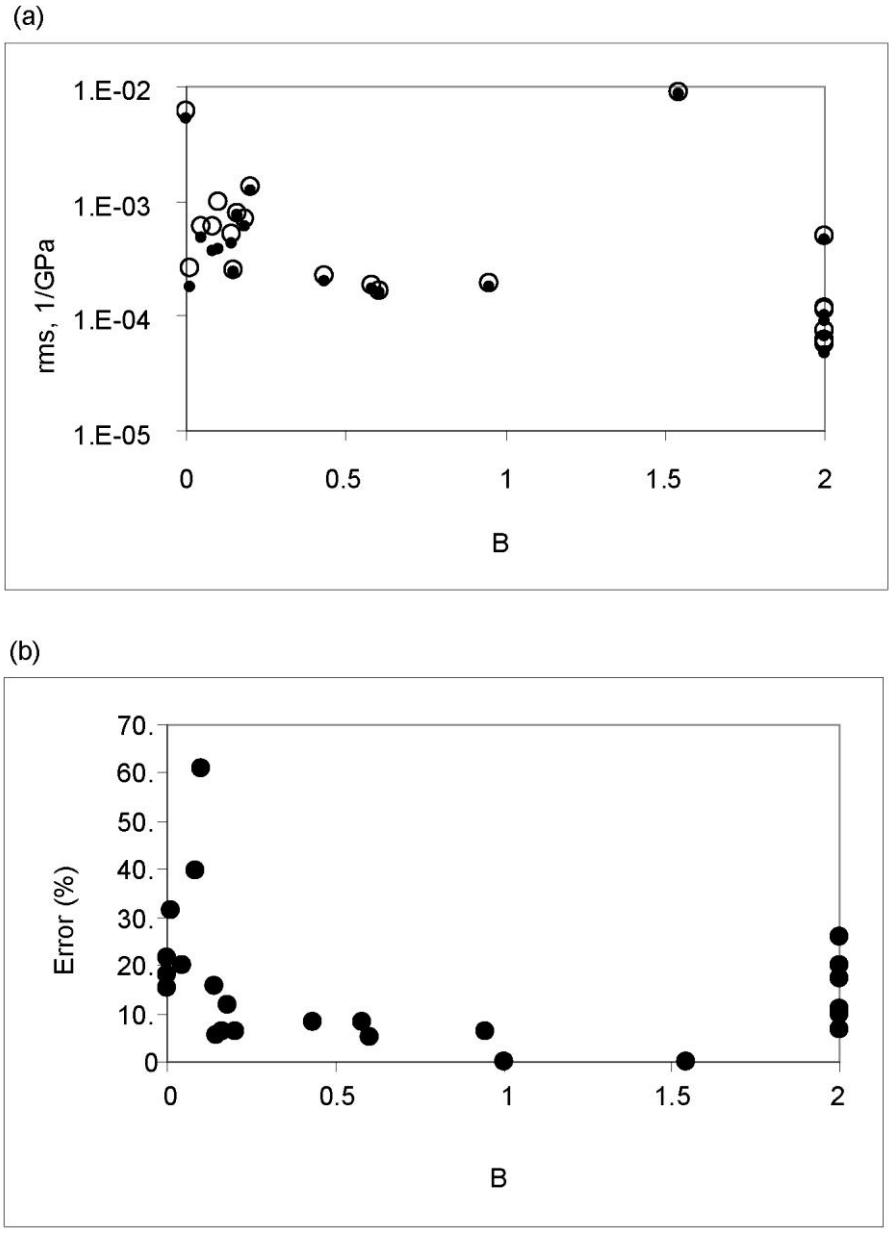

Figure 3.4 Quality of fitting of the experimental stress dependencies of elastic coefficients. (a) Misfits from equations 3.7-3.11 and equations 3.12-3.16 are shown by solid dots and open circles, respectively. (b) Relative excess in misfit caused by use of equations 3.12-3.16.

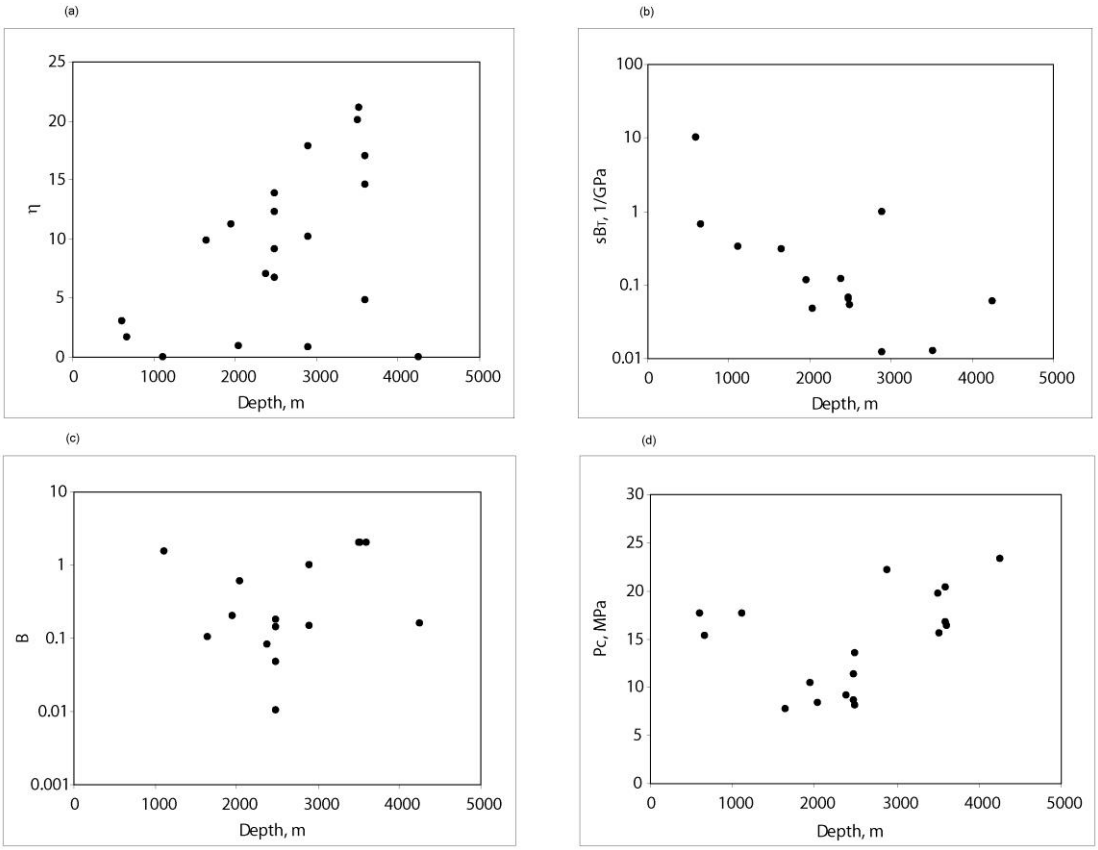

Figure 3.5 Variations with depth of (a) crack orientation anisotropy parameter η, (b) tangential compliance sB_T, (c) ratio of normal to tangential compliance B, (d) characteristic pressure P_c.

3.5 DISCUSSION

Our model of pressure dependency of shale properties can be compared to that of Ciz and Shapiro (2009). Although our fits to experimental data are somewhat better, this is achieved by introducing a new parameter, the compliance ratio B. Is this justified? Connected to this, we note that in the isotropic limit, the equations of Ciz and Shapiro (2009) reduce to a particular case of the equations of Shapiro (2003) with the ratio of bulk to shear 'piezosensitivities' (Q) equal to $(1+\nu)/(1-2\nu)$, where ν is Poisson's ratio at the high-pressure limit where all compliant porosity is closed. In turn, it has been shown (Gurevich et al., 2009) that equations of Shapiro (2003) (without dependency of stiff porosity on pressure) are equivalent to an isotropic version of Sayers and Kachanov (1995) equations with exponential dependency of both B_N and B_T on pressure. There is also a direct relationship between Q and the compliance ratio $B = B_N / B_T$ in the isotropic version of the Sayers-Kachanov model.

In particular, $Q=(1+\nu)/(1-2\nu)$ corresponds to $B=1$ (Gurevich et al. 2009, equation 10). While improvement of the fit by allowing *B* to be a free parameter may not be huge, we think that assumption $B=1$ may not be physically adequate, especially for water-saturated rocks at ultrasonic frequencies, since water in intergranular microcracks should strongly reduce B_N but not B_T. For isotropic rocks, this has been confirmed by analysis of laboratory measurements (see Sayers and Han, 2002, and Angus et al., 2009). We believe this is also logical for anisotropic rocks, including shales, even if quality of shale data may not be sufficient at present to show this conclusively. We also note that even with a new parameter *B*, our model still has fewer parameters than the model of Ciz and Shapiro (2009).

The developed model allows one to obtain statistically qualitative properties of microcracks in shales. For the analysed dataset, these properties show moderate to good correlations with the depth of extraction. Even though some of the parameters exhibit only a broad correlation with the depth of origin, such general correlations for shales may be helpful for initial characterisation of stress dependencies of elastic properties of shales in new basins. Thus, we believe that more extensive and statistically representative studies are required to confirm, improve (if possible) and understand the physical meaning of the obtained broad correlations. For example, it is well known that stress history and temperature also control mechanical and elastic properties of shales (e.g., Nygard et al., 2004; Peltonen et al., 2009) through poroelastic effects and diagenetic mineral reactions respectively. Unfortunately, such data were not available for most of the shales evaluated, so we were unable to characterize the shales more specifically in these terms at this stage. However, even with this restriction, the model gives some results that seem geologically intuitive, suggesting a physically sound basis for further development.

From analysing this limited dataset, one can conclude that the crack orientation anisotropy parameter η shows only a broad correlation with the depth. While clay particle orientation and associated microfractures are often seen as dependent on overburden stress, this can also occur through other less well defined processes that are not governed by depth alone. In addition, clay alignment also can depend on the volume of the silt fraction and the shape of silty grains, which may result in differential compaction of clays and wrapping around more rigid particles.

Hence, larger datasets may not drastically improve the correlation between η and depth of extraction or overburden pressure.

Shear compliance (B_T) shows a good correlation with depth of extraction (Figure 3.5b). More complex behaviour is observed for the ratio of normal to tangential compliance B (Figure 3.5c) in that it decreases from 1 to 0.1 between 1000 and 2500 m and then increases above unity to 3600 m. This may reflect the effects of diagenesis that generally starts at the depth of about 2000-3000 meters, driven by temperatures above 65˚C (Ruud et al., 2003; Avseth et al., 2008; Storvoll and Brevik, 2008). It should be noted that the ratio of normal to tangential compliance in a given rock will reflect the roughness of the crack surfaces and this might be affected by mineralization. The values of B estimated for real rocks often exceed theoretical predictions for traction-free cracks (which always yields $B < 1$). In particular, Angus et al. (2009) observed values of B_N/B_T up to 1.75 for dry shales. MacBeth and Schuett (2007) found that the ratio B may increase to the values above unity for thermally damaged samples. Possible contact mechanisms and the effect of mineralization on the values of B are discussed in detail in Sayers et al. (2009) and Kachanov et al. (2010). The characteristic stress, P_c, also shows a minimum in absolute values at depths of ~2500 m, similar to that observed for B; this may support our speculative suggestion that the microcrack parameters reflect the effects of mechanical compaction and diagenesis undergone by a particular shale sample. More data and detailed information on shale mineralogy and microstructure are required to test these observations.

The model we have developed can also be used for predicting the stress dependency of unknown elastic parameters from the known ones. This problem is practically important either for laboratory measurements in shales, where the C_{13} coefficient is often unreliable and, for the field data analysis, where log data only allow determination of up to four out of five elastic coefficients of TI media (Sinha et al., 2006). Note that the fitting problem described by equations 3.7-3.11 is overdetermined (see Figure 3.2). Elastic compliances used for the fitting are calculated for each effective stress at which ultrasonic velocities were measured. For instance if ultrasonic velocities were measured at n_p effective stresses, we have $5n_p$ equations in total. Thus, the four fitting parameters might be determined from experimental stress dependencies of an incomplete set of elastic coefficients. If, for

example, compliances S_{11}, S_{33}, S_{44} and S_{66} are known at four different effective stresses, we have in total 16 equations. The problem is still over determined in that four output parameters that provide the best fit of our experimental data can be found and then used to calculate the variation of S_{13} at different effective stresses using equation 3.11. If we assume that only S_{11}, S_{33} and S_{66} compliances are known at four different effective stresses, we obtain a system of 12 equations that still allow solutions for the four parameters B, B_{T0}, η and P_0. Then the variations of elastic compliances S_{13} and S_{44} can be found with equations 3.9 and 3.11. For sample G3 from brine-saturated hard shales (Wang, 2002), Figure 3.6 shows the prediction of stress dependencies of the elastic coefficients, Thomsen anisotropy parameters and anellipticity parameter (Tsvankin, 1997) using as input stress dependencies of five, four and three elastic coefficients.

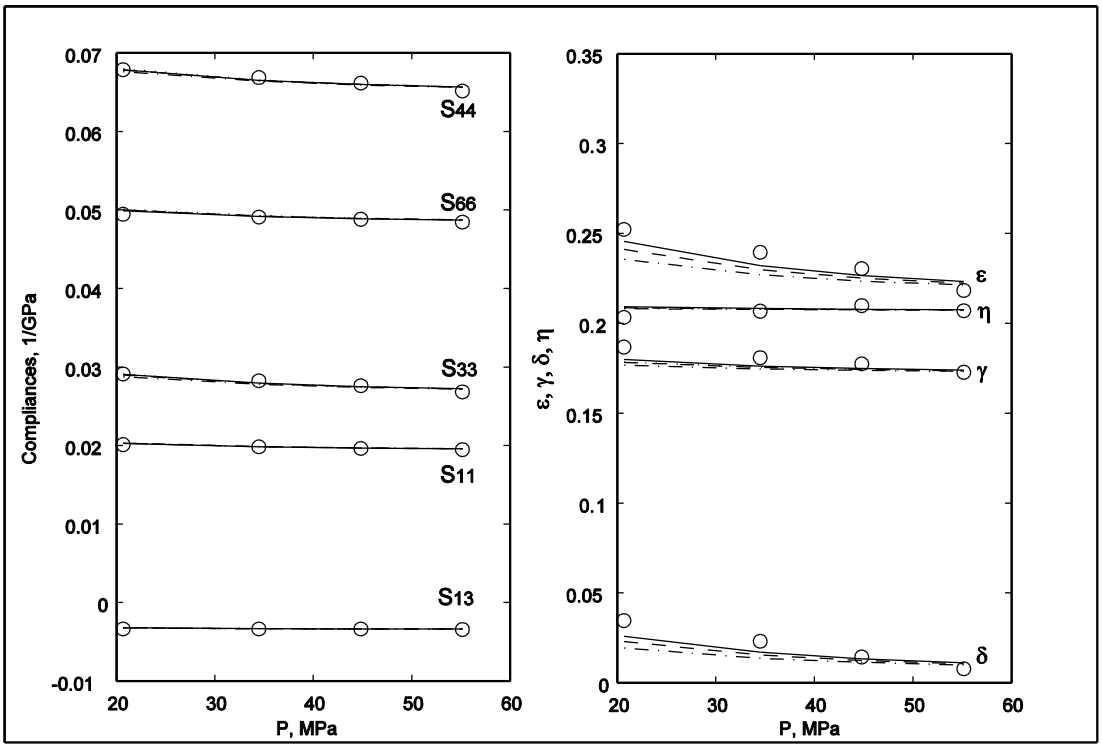

Figure 3.6 Compliances (left) and anisotropy parameters (right) for both measurements and our model on brine-saturated hard shale (sample G3 from Wang, 2002). Values calculated from ultrasonic measurements are shown by circles. Fits using the full set of five compliances are shown by thick lines. Thin lines show fits using incomplete sets of compliances. In most of the cases, the thin and thick lines coincide.

The fitting parameters η, B, sB_T, P_0 are 20, 2, 0.007 GPa^{-1} and 20 MPa. The predictions obtained from input of four elastic coefficients (S_{11}, S_{33}, S_{44}, S_{66}) are almost indistinguishable from those obtained for the input of five; the differences for the case of input of three elastic coefficients (S_{11}, S_{33}, S_{66}) are also small. However, it is important to note explicitly that this prediction does not include prediction of the intrinsic compliances S_{ij}^0, nor of the stress dependence due to the hard compliance at large effective stress.

3.6 CHAPTER CONCLUSIONS

A new stress dependency model for TI media was developed and used to parameterize stress dependencies of the elastic properties of about 20 shales. The four fitting parameters (namely, specific tangential compliance of a single discontinuity, ratio of normal to tangential compliances, characteristic pressure and crack orientation anisotropy parameter) show moderate correlations with the depth from which the shale was extracted. With increasing depth, the tangential compliance exponentially decreases. The crack orientation anisotropy parameter broadly increases with the depth for most of the shales, indicating that cracks are becoming more aligned. The ratio of normal to shear compliance as well as characteristic pressure decrease to depths of 2500 m and then increase below this to 3600 m. The suggested model also allows the prediction of stress dependency of all five elastic compliances if only three or four compliances are known. This could be useful for the reconstruction of stress dependencies of all five elastic compliances of shale from log data, for example.

CHAPTER 4 – STRESS DEPENDENCY OF ELASTIC PROPERTIES OF SHALES: THE EFFECT OF UNIAXIAL STRESS

Along with intrinsic anisotropy caused by preferred mineral orientation that is common in shales, anisotropic stress is an important factor that affects shale elastic response. While variations of elastic coefficients with anisotropic stress have been the subject of experimental studies, theoretical insight is still largely lacking. Here, we further extend the model proposed in Chapter 3 to the case where shales are subjected to uniaxial stress, which allows parameterization of the stress dependency of elastic coefficients of shales under anisotropic stress conditions. We show that parameterization requires four parameters, namely, specific tangential compliance of a single crack, the ratio of normal to tangential compliances, characteristic pressure, and a crack orientation anisotropy parameter. These parameters can be estimated from experimentally measured stress sensitivity of elastic coefficients in shales to isotropic stress.

In this chapter, I used the material published in the following SEG extended abstract with permission from co-authors and publishers (see Appendix B):

> Pervukhina M., Gurevich B., Golodoniuc P., and Dewhurst D. N., 2011, Stress dependency of elastic properties of shales: the effect of uniaxial stress: SEG Extended abstract at the SEG 2011 Conference, San Antonio, USA, doi:10.1190/1.3627669.

4.1 INTRODUCTION

The effect of stress on elastic properties of shales is also important for understanding of depositional trends especially at the upper 2000-3000 meters where the compaction is mostly mechanical. Despite the importance of the effects of isotropic and especially anisotropic stress on elastic properties of shales, little work has been done on theoretical understanding and predicting such properties and generally for the case of isotropic stress. All the existing theoretical approaches to the problem of elastic stress sensitivity are based on the analysis of orientation distribution of discontinuities and their normal, B_N, and shear, B_T, compliances. Sayers (1999) studied stress-dependent seismic anisotropy of shales using ultrasonic

measurements on two fully saturated shales of Jurassic age reported by Hornby et al. (1994), two air-dry shales from the Millboro and Braillier members of the Devonian-Mississipian Chattanooga Formation (Johnston and Christensen, 1993) and air-dry mature, kerogen-rich shale (Vernik, 1993). Sayers used the formalism presented in Sayers and Kachanov (1995) that takes into account extra compliance induced by fractures and cracks. Sayers (1999) calculated B_N / B_T ratios for each point of confining stress assuming that the discontinuities are perfectly aligned. Analysing the experimentally obtained stress dependencies of the five elastic coefficients, Sayers (1999) concluded that the contacts between clay particles are more compliant in shear than in compression and the ratios of normal to tangential compliances of individual cracks are higher for the air-dry shales compared to those in saturated shales.

Ciz and Shapiro (2009) studied the variations of elastic compliances and anisotropic parameters of Jurassic North Sea shale with isotropic stress reported in Prioul et al. (2004). They applied the so-called porosity deformation model (also known as dual porosity model, stress-sensitivity or piezo-sensitivity) initially developed by Shapiro (2003) for dry isotropic rock and later extended by Shapiro and Kaselow (2005) to the case of orthorhombic symmetry. Ciz and Shapiro (2009) described stress dependency of all elastic coefficients apart from S_{13}, which is independent of stress in the porosity deformation model. As laboratory measurements commonly show noticeable variations in S_{13} with pressure, this is a limitation of the porosity deformation model. The Sayers-Kachanov model seems to be more universal.

Using the Sayers-Kachanov model, Gurevich et al. (2011) suggested a new analytical model of stress induced anisotropy caused by application of uniaxial stress to an isotropic cracked medium. Using a similar approach, we developed a new model for stress dependency of transversely isotropic (TI) media in Chapter 3, which predicts stress sensitivity behaviour of all five elastic coefficients using four physically plausible parameters. These are the specific tangential compliance of a single crack, the ratio of normal to tangential compliances, the characteristic pressure and a crack orientation anisotropy parameter. The model has been used to parameterize elastic properties of about 20 shales. The four fitting parameters showed moderate to good correlations with the depth from which the shale was

extracted. With increasing depth, the tangential compliance exponentially decreases. The crack orientation anisotropy parameter broadly increases with the depth for most of the shales, indicating that cracks are getting more aligned in the bedding plane. The ratio of normal to shear compliance and characteristic pressure decrease with the depth to 2500 m, and then increase in the depth range of 2500-3600 m. The suggested model also allows prediction of the stress dependency of all five elastic compliances of a TI medium, even if only some of them are known.

This study extends the model developed earlier in Chapter 2 and Chapter 3 to anisotropic (uniaxial) stresses. We show that at small uniaxial stresses, these effects can be described using the same four parameters. Moreover, the values of these parameters can be extracted from the experimental measurements obtained at isotropic stress. Predictions of the model are compared with experimental measurements.

4.2 MODELLING THE EFFECT OF ANISOTROPIC STRESS ON ELASTIC COEFFICIENTS OF SHALES

Continuing the study we have conducted earlier in Chapter 3, we model the shale as an intrinsically transversely isotropic medium that is permeated with discontinuities (cracks or fractures). We assume an anisotropic orientation distribution of discontinuities for which the probability density for a particular orientation can be written as:

$$W(\theta,\phi)=\frac{1+\eta\cos^2\theta}{\int_0^{2\pi}\int_0^{\pi}\left(1+\eta\cos^2\theta\right)\sin\theta d\theta d\phi}=\frac{1+\eta\cos^2\theta}{4\pi\left(1+\eta/3\right)} \tag{4.1}$$

where θ is an angle between the *z*-axis and the normal to the crack surface (range [0, π]), ϕ determines the rotation about the z-axis (range [0, 2π]) and η is the crack orientation anisotropy parameter. An isotropic distribution of cracks corresponds to the case where $\eta=0$ and in the case when η is large, there is a strong alignment of cracks. One can check that the probability density defined by equation 4.1 satisfies the normalization condition:

$$\int_0^{2\pi}\int_0^{\pi}W(\theta,\phi)\sin\theta d\theta d\phi=1 \tag{4.2}$$

Both here and below, the *z*-axis is chosen as a symmetry axis of the TI medium. The exact geometry of individual cracks is not specified. Instead, the behaviour of cracks is defined by a ratio B of the normal B_N to tangential B_T excess crack compliances. All cracks are assumed identical; thus, B is the same for all cracks.

The medium can undergo a zero or nonzero isotropic stress. The effect of the nonzero isotropic stress on shale can be taken into account by assuming an exponential reduction of crack area $A^{(r)}$ (and specific area of cracks $s = A^{(r)}/V$) with effective pressure P (confining pressure minus pore pressure) as follows:

$$s = s^0 \exp\left(-P / P_c\right) \tag{4.3}$$

where s^0 is specific area of all the cracks at zero pressure and P_c is a characteristic crack closing pressure (Schoenberg, 2002; Shapiro, 2003; Shapiro and Kaselow, 2005; Vlastos et al., 2006).

When the rock is subjected to a small uniaxial compressive stress (σ) in addition to an isotropic stress, the density of cracks along a particular plane is reduced in proportion to the normal stress traction acting on that plane. To model closure of cracks due to application of anisotropic stress, we can assume that $B_N^{(r)}$ and $B_T^{(r)}$ are the same for all orientations of cracks, while $A^{(r)}$ (and specific area of cracks $s = A^{(r)}/V$) varies with direction of the crack normal, depending on the normal stress acting in that direction:

$$s = s^0 \exp\left(-\sigma / P_c\right) \tag{4.4}$$

When uniaxial stresses are small compared to P_c, the exponential expression in equation 4.4 can be approximated by a linear expression:

$$s = s^0 \left(1 - \sigma / P_c\right) \tag{4.5}$$

The uniaxial stress does not change the TI symmetry of the shale if it is applied along its symmetry axis (*z*-axis in our case). The variation of elastic compliances with the applied isotropic and uniaxial stresses can be calculated using Sayers-Kachanov model as follows:

$$\Delta S_{ijkl} \equiv S_{ijkl} - S^0_{ijkl} = \frac{1}{4}\left(\delta_{ik}\alpha_{jl} + \delta_{il}\alpha_{jk} + \delta_{jk}\alpha_{il} + \delta_{jl}\alpha_{ik}\right) + \beta_{ijkl} \tag{4.6}$$

$$\alpha_{ij} = \frac{1}{V}\sum_r B_T^{(r)} n_i^{(r)} n_j^{(r)} A^{(r)} \tag{4.7}$$

$$\beta_{ijkl} = \frac{1}{V}\sum_r \left(B_N^{(r)} - B_T^{(r)}\right) n_i^{(r)} n_j^{(r)} n_k^{(r)} n_l^{(r)} A^{(r)} \tag{4.8}$$

Here, ΔS_{ijkl} is the excess compliance caused by the presence of compliant cracks, S^0_{ijkl} are compliances at high stress with all soft cracks closed and S_{ijkl} are the compliances at some intermediate stress; δ_{ij} is the Kronecker delta; r is the number of planar discontinuities with surface area $A^{(r)}$ and $n_i^{(r)}$ and $n_j^{(r)}$ are i-th and j-th components of the unit vector that is normal to the surface of the r-th grain boundary in volume V; finally, B_N and B_T are the normal and tangential compliances of an individual crack.

Substituting equations 4.1, 4.3 and 4.5 together into equations (4.6-4.8), we can obtain variations of five elastic compliances for a TI fractured medium that is subject to both pressure (P) and uniaxial stress (σ) parallel to the symmetry axis of the TI medium. The derivation of the equations can be done following the procedure that is described in detail in Chapter 3.

Here we restrict our study to the case of constant effective pressure P and calculate variations of elastic compliances with variation of only anisotropic stress σ. The formulae below express the variations in terms of the four parameters as follows:

$$\Delta S_{11}^{an} = \frac{\sigma}{105P_c} B_{T0} e^{-\frac{P}{P_c}} \left(4 + 2\eta + 3B + B\eta\right) \tag{4.9}$$

$$\Delta S_{33}^{an} = \frac{\sigma}{315P_c} B_{T0} e^{-\frac{P}{P_c}} \left(18 + 10\eta + 45B + 35B\eta\right) \tag{4.10}$$

$$\Delta S_{13}^{an} = \frac{\sigma}{315P_c} B_{T0} e^{-\frac{P}{P_c}} \left(-9 - 5\eta + 9B + 5B\eta\right) \tag{4.11}$$

$$\Delta S_{44}^{an} = \frac{2\sigma}{315P_c} B_{T0} e^{-\frac{P}{P_c}} \left(24 + 17\eta + 18B + 10B\eta\right) \tag{4.12}$$

$$\Delta S_{66}^{an} = \frac{2\sigma}{315P_c} B_{T0} e^{-\frac{P}{P_c}} \left(15 + 7\eta + 6B + 2B\eta\right). \tag{4.13}$$

Here we employ the conventional matrix notation (e.g., Nye, 1985), which assumes that:

$S_{mn} \rightarrow S_{ijkl}$, when *m* and *n* are 1, 2, or 3;

$S_{mn} \rightarrow 2S_{ijkl}$, when *m* or *n* is 4, 5, or 6;

$S_{mn} \rightarrow 4S_{ijkl}$, when both *m* and *n* are 4, 5, or 6.

Note that the four parameters in equations 4.9-4.13 are the same as in the case of isotropic stress and hence can be determined from the isotropic experiments. Thus, the variations of elastic properties of shales if an anisotropic stress is applied can be predicted from the variations that occur when the shale is subjected to an isotropic stress. Here we show the applicability of this approach using experimental measurements made on a shale from the onshore Officer Basin in Western Australia (Kuila et al., 2010).

4.3 VALIDATION ON EXPERIMENTAL DATA

We compare ultrasonic velocities that were measured in a multistage triaxial test on a shale sample from the Officer Basin with predictions from the theoretical model. The Officer Basin shales are red shales of low porosity, comprising mainly illite, orthoclase and quartz. These shales are laminated and in parts are rigid grain supported. The sample of interest is extracted from the depth of 603 m and has a porosity of 6%, clay fraction of 17% and clay content of 41%. It consists of quartz (25%), orthoclase (29%), illite (35%), albite (4%), chlorite (4%), kaolinite (2%) and haematite (2%). The sample is cut perpendicular to the bedding and thus, the application of a uniaxial stress normal to the bedding does not change the TI symmetry of the sample.

The ultrasonic experiments were done on a preserved, saturated shale sample with controlled pore pressure. Firstly, a confining pressure is increased to some level, for instance 20 MPa, and pore pressure is equilibrated at, for instance, 5 MPa, then the axial stress is increased by increments, for instance, to 1, 2, 5, 8 and 15 MPa. The details of the experimental procedure and sample preparation can be found in Kuila et al. (2010).

The theoretical predictions made using formulas 4.9-4.13 and model parameters B = 0.2, B_T = 7 MPa^{-1} η = 4 and P_c = 57 MPa were obtained from isotropic measurements (refer to Chapter 3 for further details). In Figure 4.1, the measured and predicted variations in P- and S-wave velocity due to variations of axial stress are shown for effective pressures of ~10 MPa. In Figure 4.2 (a, b), P- and S-wave velocities are shown as a function of angle of incidence for the same effective stress and axial stresses of 1, 8 and 15 MPa.

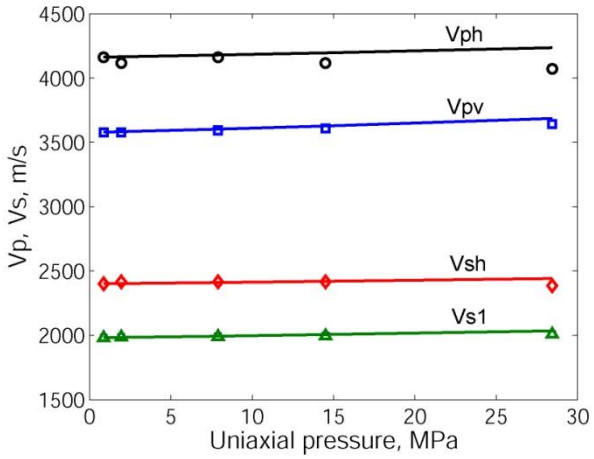

Figure 4.1 V_{ph} (circles), V_{sh} (diamonds), V_{pv} (squares) and V_{s1} (triangles) velocities measured at 10 MPa of effective pressure in Officer Basin shale compared with model predictions (solid lines).

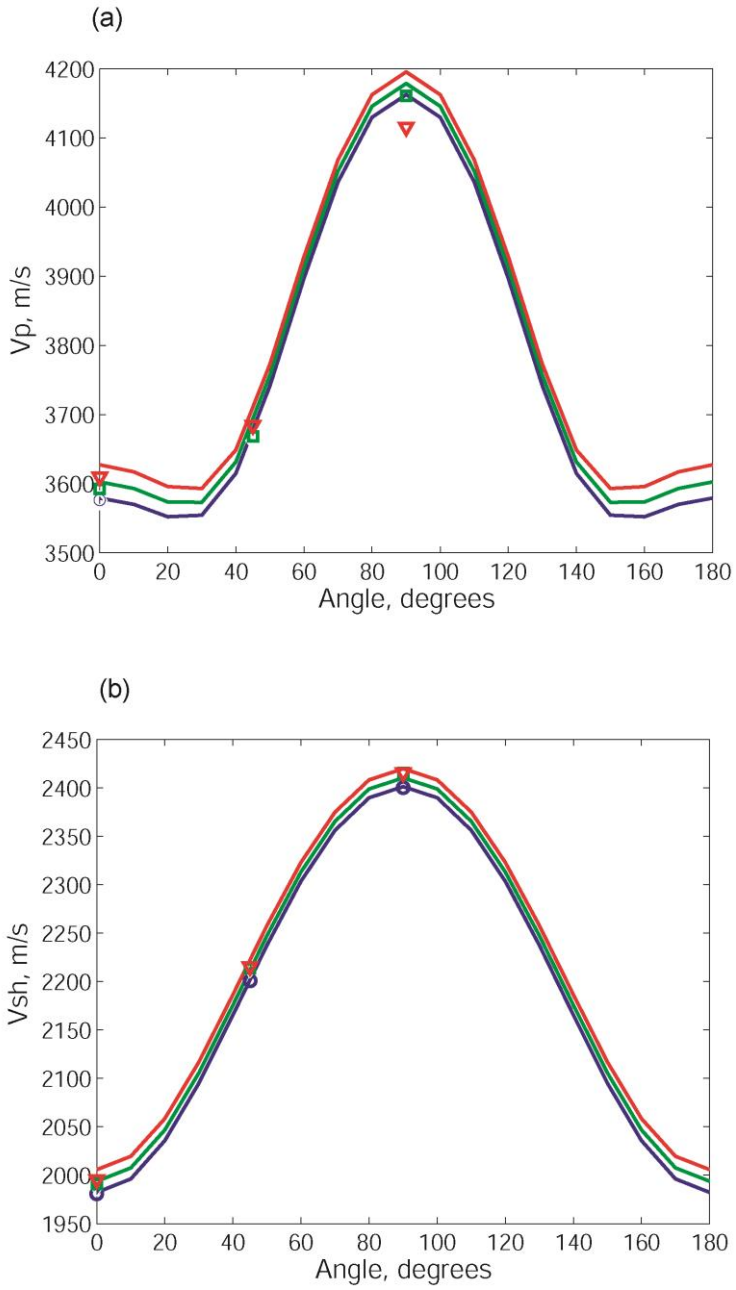

Figure 4.2 Experimentally measured and predicted velocities in Officer Basin shale at effective pressures of 10 MPa vs. angle between the direction of the wave propagation and the normal to the bedding plane: (a) V_P, (b) V_{SH}. Predicted angular dependencies for 1 MPa, 8 MPa and 15 MPa are shown by blue, green and red lines, respectively. Experimentally measured velocities for 1 MPa, 8 MPa and 15 MPa are shown by blue circles, green squares and red triangles, respectively.

4.4 DISCUSSION

Both theoretical predictions and measurements show moderate dependency of velocities with the uniaxial stress: this dependency gets weaker with an increase of effective stress. While uniaxial stress increases from 0 to 8 MPa, V_P and V_S increase by ~20 m/s at effective stresses of 10-20 MPa and even by a smaller amount at higher stresses. The model predicts maximal variations in V_P when the wave propagates perpendicular to the bedding plane, while V_S increases in both directions (parallel and perpendicular to the bedding plane). Variations in the uniaxial stress have the smallest effect on acoustic wave propagation in oblique directions. However, these conclusions are valid for this particular shale and need to be verified on other shales before application.

The developed model predicts well the variations in velocities due to the application of uniaxial stress at small values (< 10 MPa) of the uniaxial stress. At higher values of uniaxial stress, the model overestimates experimentally measured velocities, which show no further increase and can even decrease with increasing uniaxial stress. This is probably caused by opening of cracks parallel to the applied direction of the uniaxial stress which is known to reduce velocities in shale samples (Sayers, 1988; Dewhurst and Siggins, 2006; Kuila et al., 2010). The model presented here is not designed for prediction of such effects and is thus applicable to small axial stress variations ($\sigma << P_c$) only, due to the assumed linear closure of discontinuity areas with stress (equation 4.5).

It is worth emphasizing again that the four parameters used in the model are derived from the dependency of the elastic properties of the shale on *isotropic* stress and are nevertheless shown to the given an adequate prediction of variation in elastic properties under uniaxial stress. This fact implies that the model captures the essence of the stress dependency mechanism and the proposed four parameters can be used to parameterize stress sensitivity of different rock types.

The model can be used to analyse stress-related anisotropy in shales *in situ* where stress perturbations are small and the corresponding variation in elastic moduli can be assumed linear. For the general case of large stresses, when density of the cracks cannot be considered reducing linearly, an analytical solution is not feasible and numerical solution is required. However, experimental measurements in shales show that for many samples, linear variation of compliances with stress is a

reasonable approximation and our model can be used to analyse the experimental data for a moderate range of applied uniaxial stresses. The stress range that can be investigated increases with shale strength.

4.5 CHAPTER CONCLUSIONS

A new model for prediction of elastic properties variation due to application of uniaxial stress for TI media with discontinuities has been developed. The model has been tested on experimental data obtained for a shale sample from the Officer Basin in Western Australia. The predicted variations in elastic velocities are in a good agreement with experimentally measured data. The developed model can be used for prediction of elastic properties response to application of a small uniaxial stress normal to the bedding plane when only variation of elastic properties with isotropic stress is known.

CHAPTER 5 – PREDICTION OF SONIC VELOCITIES IN SHALE FROM POROSITY AND CLAY FRACTION OBTAINED FROM LOGS

Prediction of sonic velocities in shales from well logs is important for seismic to log ties, when sonic log is absent for a shaly section, for pore pressure anomaly detection, and for data quality control. Anisotropic elastic coefficients of the wet clay, a hypothetic composite material that includes all clay and water of the shale but exclude silt inclusions, are assumed as a first order approximation to be linearly dependent on wet clay porosity. Here by the wet clay porosity, we mean a ratio of a pore volume occupied by water to a total volume of the wet clay, where the former is calculated from bulk and grain densities. Effects of silt inclusions on elastic coefficients of shales are taken into account by using the anisotropic differential effective medium (DEM) model. Silt inclusions are modelled as spherical quartz particles. Simulated elastic coefficients of shales are used to calculate compressional and shear velocities and compared with the sonic velocities observed on a test dataset from a well penetrating a 500 m vertical section of shale.

To further study elastic properties of clays, elastic coefficients of shales are inverted for vertical profiles of clay elastic coefficients. The analysis of these coefficients shows that in the considered well, the increase in elastic coefficients of shales is controlled by the increase of silt fraction with depth. Elastic coefficients of clay show no increase with depth. Compared to the elastic moduli of shale, the inverted elastic moduli of wet clay show much stronger correlation with clay porosity, which confirms the hypothesis that silt fraction is one of the key parameters for modelling of elastic properties of shale.

In this chapter, I used the material previously published in the following EAGE and SEGJ extended abstracts, and that was later published in the Geophysics in 2015. All published materials were used with permission from leading co-authors and respective publishers (see Appendix B):

- Pervukhina M., Golodoniuc P., Gurevich B., Clennell M. B., Nadri D., Dewhurst D. N., and Nordgård Bolås H. M., 2012, An estimation of sonic velocities in shale from clay and silt fractions from the Elemental Capture Spectroscopy log: Extended abstract, 74th EAGE Conference, Copenhagen, Denmark.

- Pervukhina M., Golodoniuc P., and Dewhurst D. N., 2013, Rock physics modeling of sonic velocities in shales: Proceedings of the 11th SEGJ International Symposium, Yokohama, Japan, 398-401.
- Pervukhina M., Golodoniuc P., Gurevich B., Clennell M. B., Dewhurst D. N., and Nordgård Bolås H. M., 2015, Prediction of sonic velocities in shale from porosity and clay fraction obtained from logs – a North Sea well case study: Geophysics, **80(1)**, p. D1-D10, doi:10.1190/GEO2014-0044.1.

5.1 INTRODUCTION

Shales have been largely neglected in the past as barren overburden but have attracted considerable interest in recent years as reservoirs, source rocks and seals. In particular, knowledge of the factors that control elastic properties of shales is important for their characterisation from surface and borehole seismic data. Knowledge of elastic properties of shales and the parameters controlling those properties is important for the quantitative seismic data interpretation, pore pressure prediction and seismic anisotropy estimation. Most studies of shale properties are based on very laborious and time-consuming ultrasonic measurements on preserved shale samples. These samples give a very sparse representation of ubiquitous shaly sediments in the subsurface. Thus it would be useful to predict elastic properties of shales from their characteristics derived from well log data. The main objective of this chapter is to develop a methodology for predicting elastic properties of shales from their porosity and composition derived from logs, and to test and calibrate this approach against sonic log data.

Shales are highly heterogeneous multi-scale rocks with micro-scale silt inclusions, nano-scale porosity and various clay minerals as a host matrix. Despite the fact that elastic properties of shales have been studied for decades, there are still no generally accepted approaches to modelling of elastic properties of shales because of their complex nature. Application of effective medium theories, which have been successfully used to model properties of other rocks, to shales is challenging as the values of elastic properties of clay minerals are uncertain, as clays do not form large single mineral conglomerates and, thus, their properties cannot be measured by conventional ultrasonic pulse methods. The problem is further complicated by the fact that clay minerals exhibit strong elastic anisotropy. Theoretical, empirical and

experimental approaches have been proposed for estimation of elastic properties of shales and clays. Hornby et al. (1994) in their pioneering work modelled elastic properties of shales starting from isotropic clay penetrated with perfectly aligned ellipsoidal inclusions filled with water. They used self-consistent approximation (SCA) to model anisotropic moduli of a wet clay pack with different aspect ratios of ellipsoidal inclusions and then adjusted the amount of water to the desired value using the differential effective medium (DEM) approach. The Voigt-Reuss-Hill average was then used to calculate elastic moduli of wet clay composites with known orientation of clay platelets. The orientation distribution function (ODF) of the wet clay packs was estimated from SEM images of shale samples. Eventually, the effect of silt inclusions was taken into account by using DEM approach. Similar approaches to modelling of elastic properties of shales based on effective medium models were proposed by Jakobsen et al. (2000), Draege et al. (2006), Bayuk et al. (2007), Nishizawa (2010), Moyano et al. (2012) and Vasin et al. (2013). Ciz and Shapiro (2009) studied effects of discontinuities, such as clay platelet contacts and microcracks, on elastic properties of shales and their stress dependencies. Previously in Chapter 3, we showed that the ODF and strength of these discontinuities in shales change with depth. These physics-based theoretical approaches require a number of parameters, namely, aspect ratio of pores, the fractions of bound and free water and ODFs of clay platelets and microcracks that can be measured only in laboratories for a limited number of samples.

Elastic properties of clays with different mineralogies were studied by a number of authors. Aleksandrov and Ryzhova (1961) measured anisotropic elastic properties of crystalline mica. Woeber et al. (1963) measured elastic moduli of kaolinite on a cubic sample. Castagna et al. (1985) extrapolated experimental data with different mineralogies to a zero-porosity limit. Katahara (1996) derived elastic properties of different clay minerals using Voigt-Reuss-Hill averaging. Wang et al. (2001) inverted measured clay and epoxy mixture properties for elastic properties of illite, smectite, mixed layer illite-smectite and kaolinite. Pal-Bathija et al. (2008) and Prasad et al. (2005, 2002) studied properties of clay minerals using atomic force microscope and nanoindentation methods. Vanorio et al. (2003) measured elastic properties of smectite cold-pressed from the clay powder. Sayers (2005) and Bayuk et al. (2007) inverted experimental measurements in Cretaceous Shales (from Jones

and Wang, 1981) for elastic properties of illite-smectite-kaolinite mixture. Mondol (2007) and Voltolini et al. (2009) measured elastic properties of smectite, illite and kaolinite mixtures obtained from wet clay powders by compaction. All these studies result in a set of isotropic and anisotropic moduli of clay minerals that differ from each other by more than an order of magnitude. Indeed, bulk modulus *K*, ranges from 1.5-60.2 GPa and shear modulus μ from 1.4-31.8 GPa. Such an enormous variability in elastic properties of clays results in massive uncertainty when modelling elastic properties of shales using an effective medium approach.

Recently, an alternative approach (the so-called GeoGenom model) was developed and successfully applied for prediction of elastic properties of shales without a detailed knowledge of clay mineralogy or microstructure (Ulm and Abousleiman, 2006; Ortega et al., 2007). This approach is based on the hypothesis that elastic properties of wet clay are entirely controlled by its total porosity and, for a given total porosity, is insensitive to clay mineralogy. The properties of wet clay will still depend on mineralogy indirectly as different clay minerals have different water content. The foundation to the GeoGenom model was laid by Ulm and Abousleiman (2006) who suggested using nanoindentation for direct measurements of elastic properties of clays in natural shales of complex mineralogy. The experimental data were then used to calibrate poroelastic dependency of elastic moduli vs. porosity for wet clay composites by Ortega et al. (2007). The method was extended to predict elastic moduli of shales by populating the wet clay composites with silt inclusions. The effect of silt inclusions is taken into account by SCA modelling which assumes that both constituents are connected and thus can be load bearing when concentrations of the constituents are approximately equal.

The most attractive idea of the GeoGenom model is that elastic moduli of clay can be estimated from total porosity and silt fraction. This idea was further tested by Pervukhina et al., (2008a,b), who inverted ultrasonic anisotropic elastic coefficients of shales for elastic coefficients of clays using an anisotropic DEM approach (Nishizawa, 1982). Based on the obtained results, Pervukhina et al., (2008a,b) showed that a linear relationship between the water fraction in wet clay packs and the anisotropic elastic coefficients of clays is a reasonable first-order approximation. The elastic coefficients of hypothetical clay with zero water fraction were obtained by interpolation of these linear dependencies. This method, hereafter

called Clay-Plus-Silt (CPS) model, will be described further in more detail. An advantage of this method is that it does not require detailed knowledge of clay mineralogy and microstructure and has no fitting or adjustment parameters. It can be directly applied for modelling of elastic properties of shales from well log data as all the necessary parameters can be obtained from wireline measurements. Furthermore, as wireline logs contain thousands of point measurements, this method can be used for statistically representative inversion of elastic properties of shale for those of clay. Such inversion can be used for the justification and improvement of the clay moduli.

In this study, we first test the predictive power of Clay-Plus-Silt methodology by applying it to modelling of shale velocity profiles in a vertical well. The input parameters that are necessary for this modelling are recovered from independent wireline log measurements such as density log and neutron porosity. Grain density, which is required to calculate porosity from density logs, is obtained from Elemental Capture Spectroscopy (ECS) tool and known mineral grain densities. The simulated elastic wave velocities are compared with the velocities measured by the sonic tool (DSI). Then, we design an algorithm that allows inversion of measured sonic velocities of shales for elastic coefficients of clays.

5.2 FORWARD MODELLING WORKFLOW

To predict elastic properties of shales from log-derived porosity and mineralogy we employ the Clay-Plus-Silt (CPS) model proposed by Pervukhina et al. (2008a,b) based on the concept of the GeoGenom model. In the CPS model, the only required input parameters are volume fractions of shale constituents, namely, the volume fractions of clay, silt and water.

Here, the terms shale and clay are used in the sense that is common for rock physics studies (e.g., Hornby, 1994; Sayers, 2005; Bayuk, 2007; Mondol, 2007). By shale, we mean a composite material that consists of a wet clay load-bearing matrix and silt inclusions floating in this matrix. By wet clay we mean hypothetic composite material that includes all clay and water of the shale but without silt inclusions. All water is assumed to be contained in the wet clay; silt inclusions do not contain any porosity. For the sake of brevity hereafter, we sometimes use terms “clay” and “wet clay” to denote the wet clay. It is worth noting again that the terms “clay” and

"shale" have different meanings here as the latter means the composite of clay and silt (see Figure 5.1, which shows an SEM image of shale extracted from the well of interest). Hereafter, elastic coefficients of shale and clay are denoted with upper and lower-case letters, respectively.

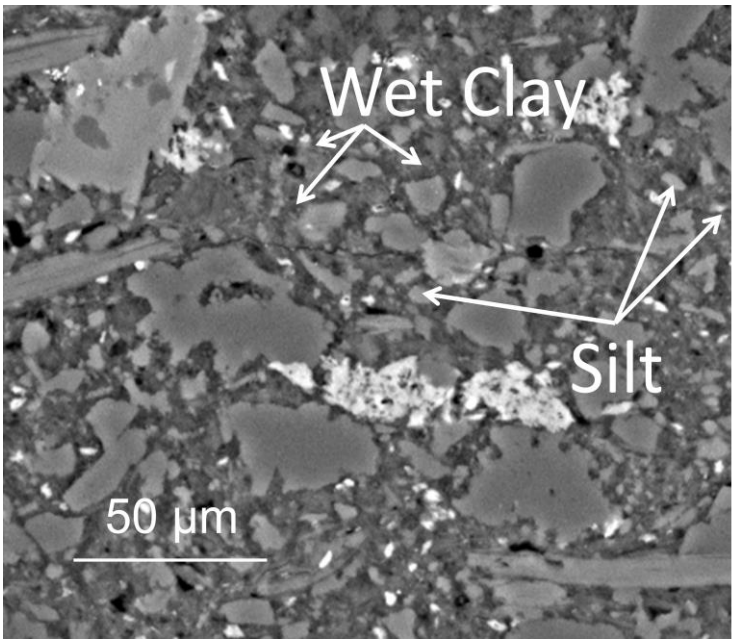

Figure 5.1 SEM image of a shale sample extracted from the well of interest (courtesy of C. Delle Piane). Silt fraction mainly consists of quartz carbonate inclusions. Wet clay occupies the remaining volume of the shale.

The CPS model was previously applied to a suite of shales for which ultrasonic velocities were measured by ultrasonic pulse method (Dewhurst and Siggins, 2006; Dewhurst et al., 2008; Kuila et al., 2011) and concentrations of clay and non-clay components were known from XRD analysis. The elastic coefficients of anisotropic shales predicted with the CPS model were shown to be in good agreement with the experimentally measured elastic coefficients of shales. (Pervukhina et al., 2008a,b).

The CPS model can be extended to prediction of sonic velocities of shales obtained by wireline log measurements if the porosity and concentration of clay and non-clay constituents are also obtained. Here we use the density and neutron porosity logs to find clay and silt fractions (Ellis and Singer, 2008). The results of the modelling procedure are compared with sonic velocities measured by a sonic tool

(DSI) from the same well. The detailed modelling procedure is described below. At each step, we underline all assumptions that we make.

1. At the first step we calculate porosity, ϕ, of rock from density log as follows:

$$\phi = (\rho_g - \rho_b)/(\rho_g - \rho_w) \tag{5.1}$$

Here ρ_b is bulk density, ρ_g is the matrix density obtained from the dry weight fractions of the composite minerals measured by the ECS tool and ρ_w is the saturating fluid density (brine for this particular well).

Alternatively, the porosity can be estimated from neutron logs by calibrating it with laboratory core measurements. However, one must be careful as the standard laboratory porosity measurement procedures are not well established for shale and might give systematically biased results. It is generally known that mercury intrusion porosimetry (MIP) underestimates porosity in shales. Another method of estimation of free water mass fraction in shales is based on the comparison of preserved (saturated) shale density with the density of the dry shale (obtained by keeping it in an oven at a temperature of 105°C for 24 hours). This method assumes that all water has been evaporated from the sample; this assumption is questionable, especially for low permeability shales. Hereafter we use the porosity calculated from the bulk and grain density using equation (5.1).

2. Clay and silt fractions out of the solid phase, f_c^0 and f_s^0, are then estimated using a neutron-density cross-plot (e.g., Ellis and Singer, 2008). The volumetric clay and silt fractions are then calculated as:

$$f_c = f_c^0(1-\phi) \tag{5.2}$$

and

$$f_s = 1 - f_c - \phi \tag{5.3}$$

3. The wet clay porosity, κ, is determined as a ratio of the volume of pores to the total volume of the clay constituent:

$$\kappa = \frac{\phi}{f_c + \phi} \tag{5.4}$$

The WCP is analogous to the clay packing density parameter (CPD) introduced by Ulm and Abousleiman (2006), but we find WCP more intuitive. CPD and WCP are connected by a simple relation $CPD = 1 - \kappa$. By introducing WCP parameter in such a way, we assume that all the porosity is hosted between clay platelets and that the silt is non-porous. This assumption is plausible as, for the well of interest, the silt mostly consists of quartz inclusions and these microscopic quartz particles can be considered as non-porous.

4. We here assume that both the shale and its clay constituent are transversely isotropic with a vertical symmetry axis (VTI). This is a reasonable approximation for shales that are not subject to vertical fractures or anisotropic horizontal stress. Furthermore, based on a number of laboratory experiments, Pervukhina et al. (2008a,b) showed that a linear dependency of shale elastic coefficients on clay packing density is a reasonable first order approximation for a wide range of wet clay porosities. The dependency of the elastic coefficients, c_{ij}, on WCP will then be linear as well:

$$c_{ij} = c_{ij}^{0}\left(0.5 - \kappa\right) \tag{5.5}$$

Here c_{ij}^{0} are elastic coefficients of hypothetical clay with $\kappa = 0$, which were obtained from the linear regression coefficients and were shown to be equal to c_{11}^{0} = 46.4 GPa, c_{33}^{0} = 29.9 GPa, c_{13}^{0} = 17.9 GPa, c_{44}^{0} = 6.7 GPa and c_{66}^{0} = 11.2 GPa (Pervukhina et al., 2008a). The coefficient 0.5 arises in equation 5.5 as we assume that the wet clay is not load-bearing if the volumetric water fraction in it is equal or exceeds 50%. Hereafter, we use these relations to estimate elastic coefficients of clay based of porosities and clay fractions obtained by logs (equations 5.1 and 5.2).

5. Steps 1-4 give allow us to compute anisotropic elastic moduli of wet clay. In addition to wet clay, the shale usually contains significant amount of silt inclusions, Indeed, the concept that silt fraction has a prominent effect on elastic coefficients of shales and that this effect must be taken into account is widely accepted (e.g., Hornby et al., 1994; Bayuk et al., 2007; Ulm and

Abousleiman, 2006). We take into account the effect of the silt inclusions using an anisotropic Differential Effective Medium (DEM) approach (Nishizawa, 1982). The DEM method calculates elastic properties of shale by incrementally adding silt inclusions into the clay matrix up to the measured fraction of the silt constituent (equation 5.2). Anisotropic elastic properties of the clay matrix are calculated from equation 5.5. Application of DEM model implies that silt is present in the form of isolated inclusions in the interconnected clay matrix. The silt inclusions are modelled as quartz spheroids. The assumption of connectivity of the clay matrix and round shape of silt inclusions are consistent with observations of numerous SEM images (e.g., Desbois, 2009). It is worth noting that this approach is not applicable to shaly sands in which microstructural distribution of clay in a sandstone should be taken into account and which can depend of clay fraction and compaction (for more detailed information see, for instance, Sams and Andrea, 2001).

6. Elastic wave velocities in the direction normal to bedding are then calculated as follows:

$$V_P = \left(C_{33}/\rho_b\right)^{1/2} \tag{5.6}$$

$$V_S = \left(C_{44}/\rho_b\right)^{1/2} \tag{5.7}$$

These equations will give sonic velocities in a well that is drilled normal to bedding plane. In the case of a deviated well or tilted bedding, the calculation of the velocities from the elastic coefficients depends on whether group or phase velocity is measured by a sonic tool. The detailed discussion on this topic can be found in Miller et al. (2012) and Pervukhina et al. (2013).

7. To estimate uncertainties of the velocity simulation at each depth, we perform simulations with N=100 realisations of the input parameters (namely, porosity, ϕ, and clay fraction, f_c, with added Gaussian noise of 5%). The mean and standard deviation for both compressional and shear velocities are then calculated as:

$$\overline{V} = \frac{\sum_{i=1}^{N} V\left(\phi^i, f_c^{\,i}\right)}{N} \tag{5.8}$$

and

$$\sigma = \frac{\sum_{i=1}^{N} \left(V_i - \overline{V}\right)^2}{N-1} \tag{5.9}$$

5.3 LOG DATA EXAMPLE

To test the predictions of the workflow described above, we apply it to log data in a vertical well. Log data, namely, gamma ray (GR), bulk and grain density, neutron and density porosity and mineralogy measured in the well are shown in Figure 5.2. The distance between the major grid lines is 100 metres and between the minor ones is 25 metres.

The GR values are high (160-180 gAPI) throughout the whole 500 metres depth interval apart from the interval of about 40 metres in the middle and a few short intervals at the bottom. The high gamma ray values are a good indication of shales if no other radioactive minerals are present. The abundance of the shale in the well is also confirmed by the deviation of the measured neutron porosity from the porosity calculated from density using equation 5.1. Neutron porosity is up to 20% higher than density porosity in the depth intervals with high gamma ray readings and the porosities match each other in the depth intervals with low gamma ray values. Modelling of shale properties is done only for the depths at which silt fraction is below 0.4.

Figure 5.3 gives a visual illustration that the silt effect on elastic properties of shales is observable on the log measurement scale. The elastic coefficients of shales are then plotted against wet clay porosity, κ, and colour coded in accordance with silt fraction, f_s. Elastic coefficients C_{33} are calculated from sonic velocities and bulk density as follows:

$$C_{33} = \rho_b V_P^2 \tag{5.10}$$

$$C_{44} = \rho_b V_S^2 \tag{5.11}$$

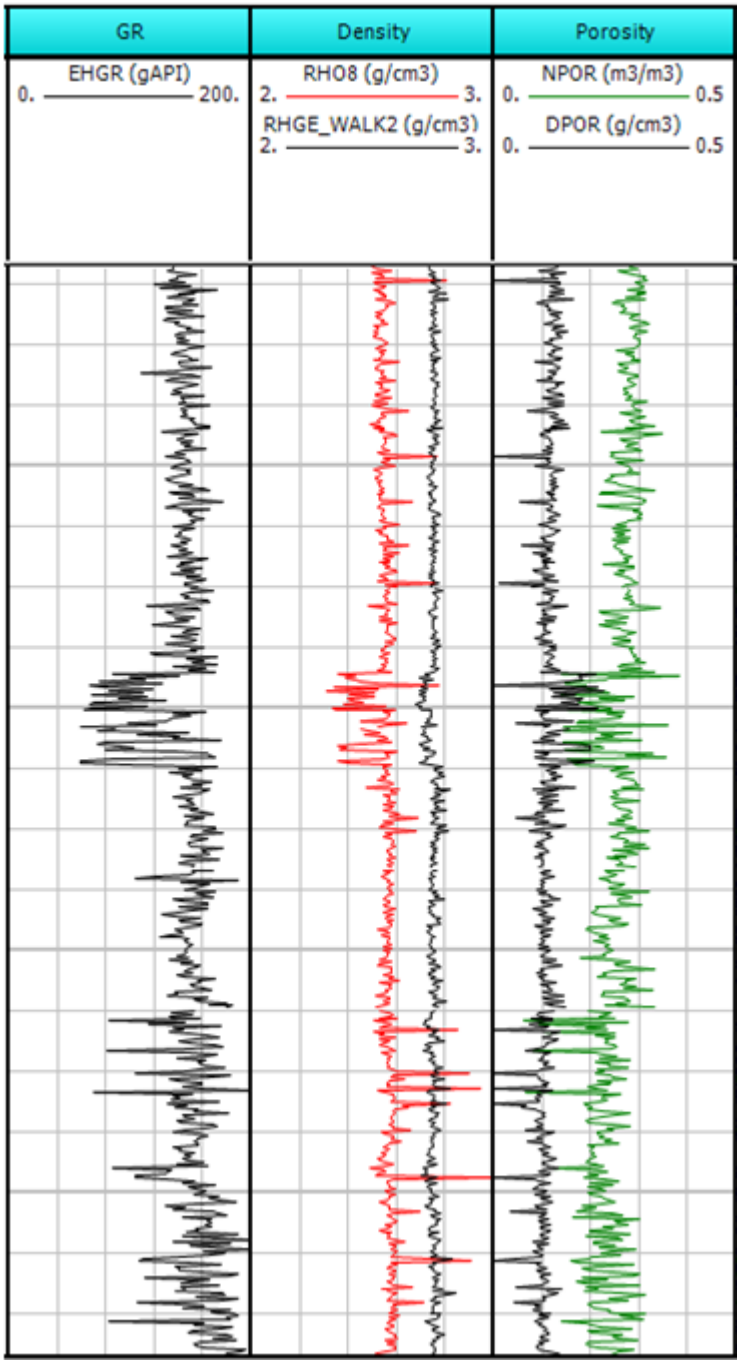

Figure 5.2 Log data (left to right): Gamma ray (GR), bulk (RHO8) and grain (RHGE) density, neutron (NPOR) and density (DPOR) porosity.

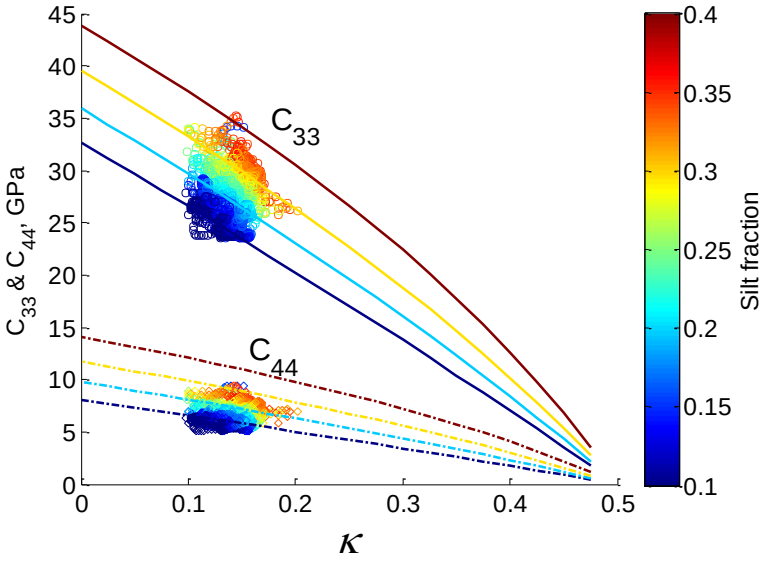

Figure 5.3 Elastic coefficients C_{33} and C_{44} calculated from log data vs. wet clay porosity, κ, colour coded with respect to silt fractions are compared to CPS model predictions for silt fractions of 0.4, 0.3, 0.2 and 0.1, which are shown by brown, yellow, cyan and blue, respectively.

The individual coefficients C_{33} and C_{44} are shown for shale ($f_s \le 0.4$) throughout the whole depth interval. The same elastic coefficients simulated using DEM approach for four different silt fractions 0.1, 0.2, 0.3 and 0.4 are shown by light blue, green, orange and dark red solid lines, respectively. The elastic coefficients of shale regardless its silt fraction exhibit significant scatter and show no obvious trend with wet clay porosity. However, for a narrower range of silt fractions, for example, from 0.1 to 0.2, the elastic coefficients show obvious trends that are similar to the trends of model predictions.

Gamma ray log, measured sonic velocities and CPS model predictions are shown in Figure 5.4 at two different scales. In Figure 5.4a the sonic velocities (blue lines) are shown in comparison with mean modelled velocities (red lines) calculated using equation (5.8) throughout the whole shale interval of about 500 metres. The dashed and dotted lines are the smoothed measured sonic velocities plus and minus 10%, respectively. In Figure 5.4b the gamma ray and velocities are shown for a ~50 metre interval. Red dashed and dotted lines in Figure 5.4b are $\overline{V} \pm 2\sigma$, where mean velocities and standard deviation are calculated using equations (5.8) and (5.9).

(a) (b)

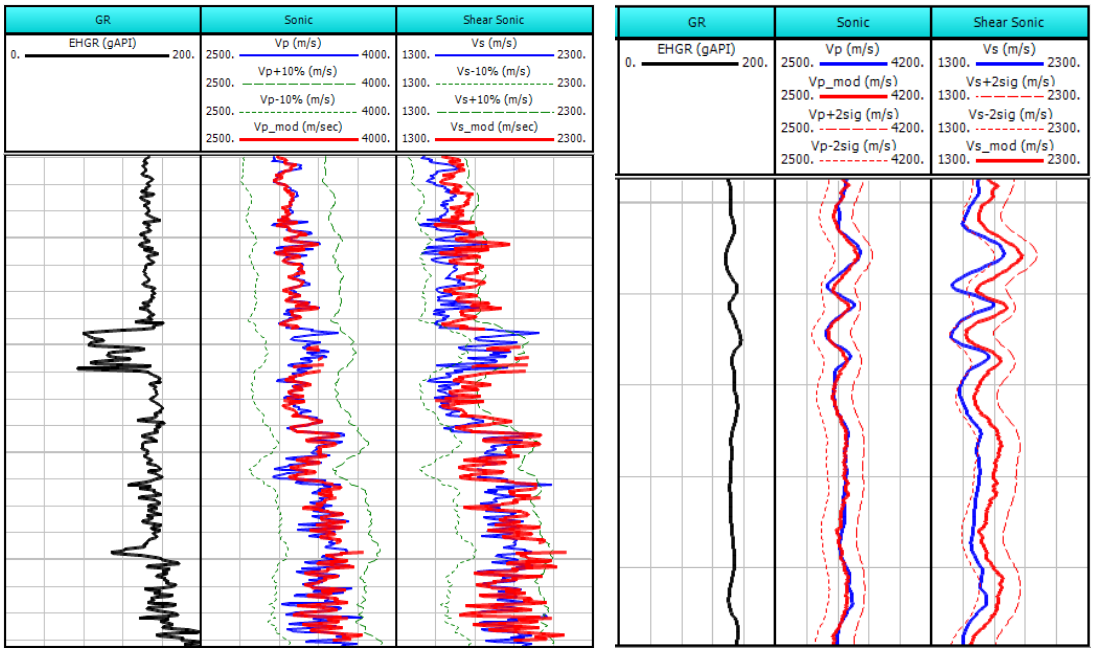

Figure 5.4 Gamma ray, compressional and shear sonic velocities (blue lines) in comparison with simulated velocities (red lines): (a) throughout the whole shale interval, the depth between major gridlines is 100 m; (b) throughout about 50 m of depth; 10 m distance between gridlines.

The cross-plot of the modelled versus measured velocities is shown in Figure 5.5. The modelled compressional velocity is in a good agreement with measured sonic log velocity with linear regression coefficient of 1.0 and the coefficient of determination R^2=0.8. The modelled shear velocities show a systematic shift of about 8% but the coefficient of determination is still 0.8. This discrepancy might be explained by the fact that for the forward modelling we used the elastic coefficients of clay that were derived from laboratory experiments on preserved shale samples excavated from different places all over the world (details can be found in Pervukhina et al., 2008a,b). In the following sections, we invert the log sonic velocities measured in shales for elastic coefficients of clay but we do not use these coefficients for forward modelling. The purpose of the inversion is to study variations of clay properties with wet clay porosity and with depth in more detail, rather than to fit modelling results with the measured ones.

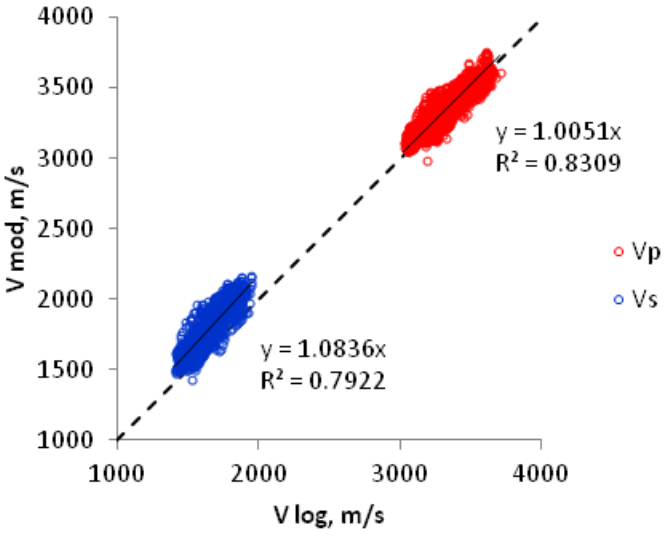

Figure 5.5 Modelled shale velocities vs. measured sonic log velocities.

5.4 INVERSION FOR ELASTIC PROPERTIES OF WET CLAY

In the previous section, we showed that the CPS model can be used to estimate elastic moduli of shales from porosity and mineralogy logs. In the interval covered by sonic data, we can also invert the sonic velocity and silt fraction for elastic moduli of wet clay using the anisotropic DEM model without a priori knowledge of the relationship between clay moduli and porosity. However, it is worth noting that the inversion is limited to two elastic coefficients of clays c_{33} and c_{44}, as only these elastic coefficients of shale can be obtained from sonic velocity measurements in vertical wells drilled normal to bedding.

Here we invert the elastic properties of shales obtained from the sonic log measurements in the same vertical well throughout the whole 500 metres shale interval. The inversion is done by minimising the function:

$$\Phi\left(c_{ii}\right)=\sum_{i=3}^{4}\left(C_{ii}^{DEM}\left(\kappa, f_s, \alpha, c_{ii}\right)-C_{ii}^{\exp}\right)^2 \qquad (5.12)$$

Elastic coefficients of shales $C_{ii}^{\exp}$ are calculated from sonic log velocities using equations (5.10) and (5.11). C_{ii}^{DEM} are simulated using anisotropic DEM (Nishizawa, 1982). κ and f_s are calculated for a particular depth log measurements using equations (5.3) and (5.4). The inversion is done for several aspect ratios, α, of

silt inclusion ranging from 0.1 to 1. The initial guess for the inversion is obtained using equation (5.5) with c_{33}^0 = 29.9 GPa, and c_{44}^0 = 6.7 GPa. The Levenberg-Marquardt method (Moré, 1977) implemented in the MATLAB optimization toolbox is used to minimise function (5.12).

To study sensitivity of the inverted elastic coefficients of clay to the aspect ratio of silt inclusions, we inverted C_{33} and C_{44} for elastic coefficients of clays for six aspect ratios of silt inclusions of 0.1, 0.2, 0.3, 0.5, 0.7 and 1.0. The study is limited to the aspect ratios in the range from 0.1 to 1.0 as these aspect ratios of the silt inclusions have been observed in micro- and nanotomographic studies of shale microstructure. The inverted C_{33} and C_{44} are plotted in Figure 5.6 against κ for silt inclusion aspect ratio of 1. This figure demonstrates that removing the effect of silt dramatically reduced the large scatter (as shown in Figure 5.3) of the elastic moduli for a given clay porosity. Elastic coefficients exhibit obvious negative trend with the increase of WCP. The best fit linear trends are shown in the same plot by black solid lines. Elastic coefficients c_{33}^0 and c_{44}^0 of the clay in the hypothetic non-porous state (with zero wet clay porosity) can be obtained by extrapolating the trend lines to zero WCP.

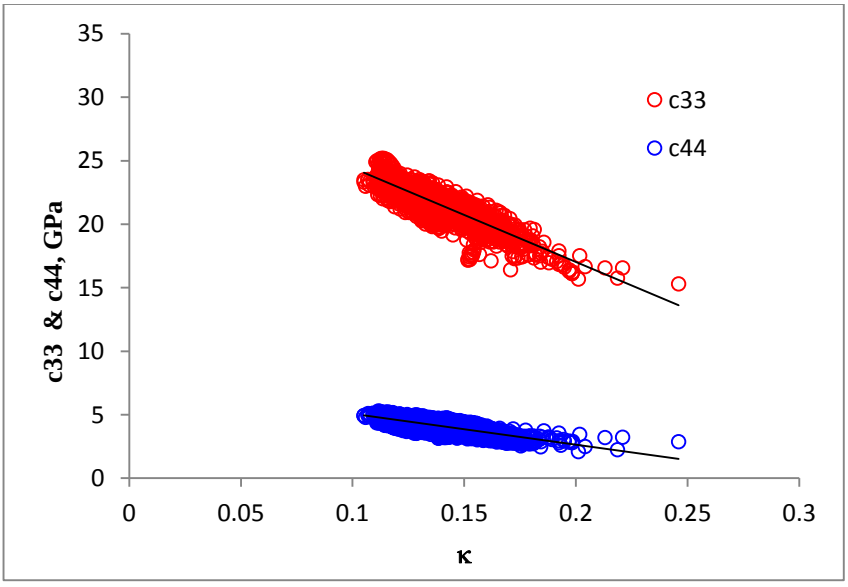

Figure 5.6 Elastic coefficients, c_{33} and c_{44}, of clay obtained by the inversion procedure against wet clay porosity using silt aspect ratio of 1 (i.e. spherical). The best linear fit is shown by black line.

The elastic coefficients at zero wet clay porosity are shown in Table 5.1 for different aspect ratios of silt inclusions of 0.1, 0.2, 0.3, 0.5, 0.7 and 1.0. The averaged values are $c_{33}^0 = 32.3 \pm 0.3$ and $c_{44}^0 = 7.5 \pm 0.1$. One can see that the effect of the aspect ratio of silt inclusions on the inverted coefficients of clays does not exceed 2%. This indicates that the rigorous bounds for elastic moduli are quite close for these moduli of the constituents. Therefore, in further analysis, we use elastic coefficients inverted using silt particles with aspect ratios of 1.0 (i.e., spheres). These values of the elastic coefficients of hypothetic clay with zero porosity are close (especially for c_{33}) to the values of 29.9 GPa and 6.7 GPa, which were acquired from laboratory measurements (Pervukhina et al., 2008a) and are used for forward modelling.

Table 5.1 Results the linear extrapolation of the inverted clay coefficients to $\kappa = 0$ using silt inclusions with different aspect ratios, α. Coefficients of determination, R^2, indicate that linear trends fit the inverted coefficients better in the cases of large aspect ratios of silt inclusions.

α	0.1	0.2	0.3	0.5	0.7	1.0
c_{33}, GPa	32.0	32.0	32.1	32.3	32.4	32.7
R_{33}^2	0.7	0.7	0.7	0.8	0.8	0.8
c_{44}, GPa	7.3	7.4	7.5	7.6	7.6	7.6
R_{44}^2	0.5	0.6	0.7	0.7	0.7	0.7

5.5 DISCUSSION

The inversion results for the moduli c_{33} and c_{44} of clay, corresponding to the original moduli of shale C_{33} and C_{44}, wet clay porosity and silt fraction are shown in Figure 5.7 (a, b). The best linear fits of these values are shown in the same plots and Table 5.2 summarises their depth gradients. We see that the shale moduli, C_{33} and C_{44}, systematically increase with depth by ~5% and ~3% per 100 metres, respectively. Assuming that wet clay porosity decreases with depth due to compaction, we must expect to see some increase of clay elastic coefficients with depth. As a matter of fact for this particular well, the depth gradients of either WCP or clay elastic coefficients c_{33} and c_{44} are negligible (Table 5.2). Instead, a noticeable silt fraction increase with the increase of depth of 4% per 100 metres is detected, which may explain the observed stiffening of the shale.

The lack of increase of compaction-induced porous clay moduli with depth is intriguing. This might be the result of the fact that the clay fraction is obtained from the neutron-density separation using a single clay point for the whole 500 metres depth. It is hard to assess the validity of this assumption in our well since it shows very large systematic increase of silt fraction with depth. It is most likely that the depth interval of 500 metres is simply not sufficient to clearly see the compaction trend and separate it from the strong shale trend caused by the changes in silt and clay fractions. This issue requires further analysis.

Table 5.2 Depth gradients.

	Per 100 meters
C_{33},GPa	5%
C_{44}, GPa	3%
c_{33}, GPa	-0.5%
c_{44}, GPa	-0.5%
κ, %	-0.5%
f_s, %	4%

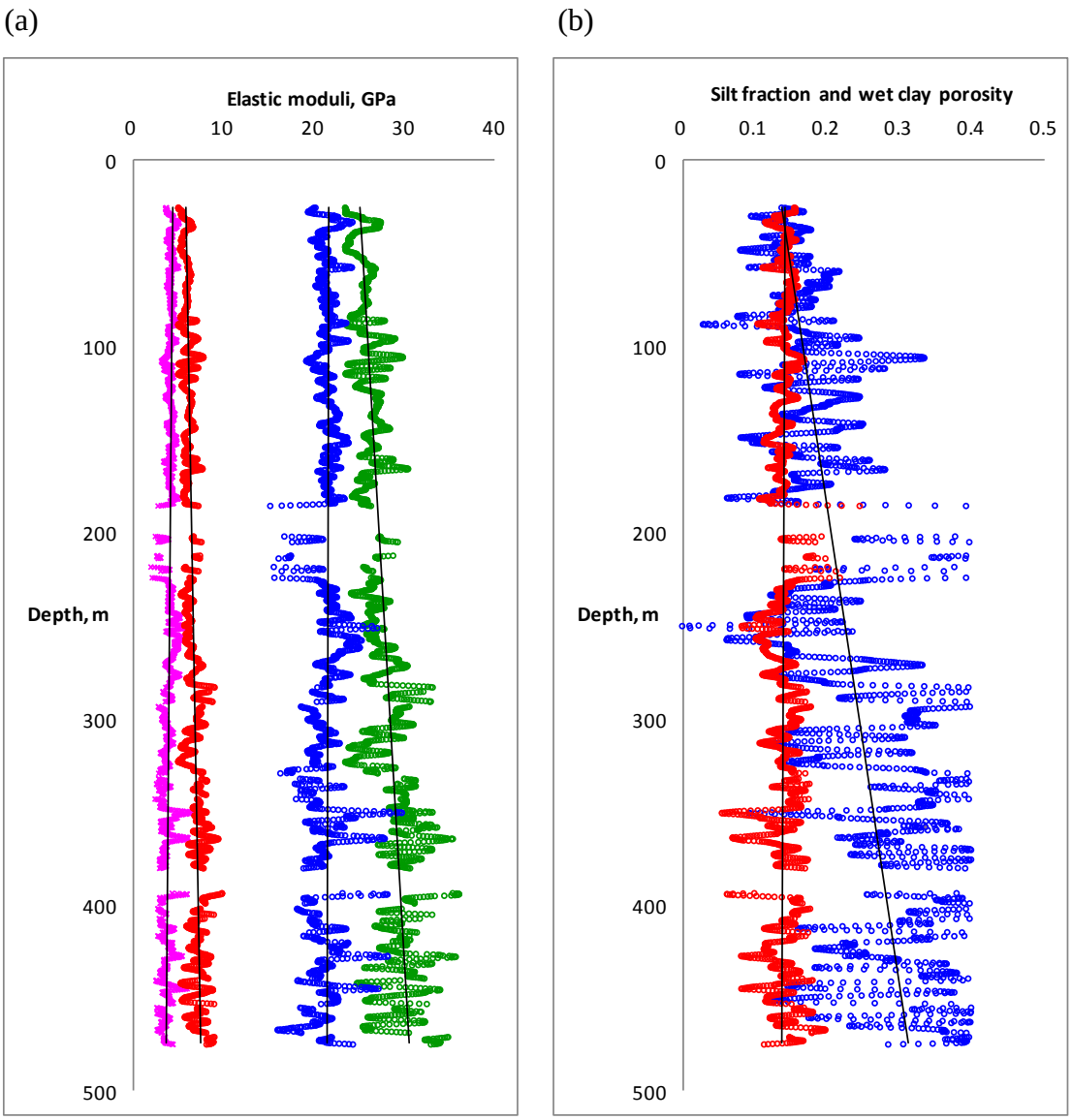

Figure 5.7 Depth dependencies of elastic coefficients, silt fraction and wet clay porosity: (a) C_{33} (green), c_{33} (blue), C_{44} (red) and c_{44} (magenta) and (b) wet clay porosity (red) and silt fraction (blue). By depth here, we mean the depth from some non-zero level.

5.6 CHAPTER CONCLUSIONS

We have confirmed that wet clay porosity and silt fraction are the two key parameters for modelling of elastic properties of shales. These parameters can be obtained from clay fraction derived from common well log measurements such as neutron-density separation or similar quantitative mineralogy information. Knowledge of these parameters allowed prediction of elastic properties of shales throughout the depth interval of about 500 metres without detailed knowledge of the shale mineralogy. The predicted velocities show good agreement with the measured velocities but a systematic shift is observed for shear velocities.

The analysis of the elastic properties of clay inverted on the basis of the knowledge of the log measurements of sonic velocities, bulk and grain density, plus silt fraction shows that in the considered well, the increase in elastic coefficients of shales is controlled by the increase of silt fraction with depth. Elastic coefficients of clay show no increase with depth. Furthermore, compared to the elastic moduli of shale, the inverted elastic moduli of wet clay show much stronger correlation with clay porosity, which confirms the hypothesis that silt fraction is one of the key parameters for modelling of elastic properties of shale.

CONCLUDING REMARKS

Various research aspects covered in this thesis include (a) 3D reconstruction of X-ray microtomographic images for acquisition of realistic computer models of rocks, (b) experimental verification of velocity-stress relationship for isotropic porous rocks, (c) shale anisotropy and parameterization of elastic stress sensitivity in shales, (d) prediction of sonic velocities in shales from clay and silt fractions from the data obtained from wire logging tools without detailed knowledge of rock mineralogy. Given the diversity of petrophysics problems addressed in this thesis and independence of some chapters, obtained results from each chapter are summarised individually:

- Chapter 1. A comprehensive digital rock physics workflow has been developed to support realistic 3D image reconstruction, processing and noise suppression, and finite element method simulations to complement laboratory experiments. On a computer model reconstructed from a real sandstone specimen it has been demonstrated that numerically simulated elastic moduli correlate well with laboratory measurements, proving the method applicability for computational up-scaling of elastic moduli of porous rocks.

- Chapter 2. Dual porosity concept and its interpretation of exponential stress dependency of elastic properties of rocks has been tested using laboratory measurements on dry sandstones and has shown that (a) elastic compressibility is linearly dependant on soft porosity, and (b) exponential decay of soft porosity and elastic compressibility can be observed with effective stress up to 60 MPa. The obtained results reconfirm the applicability of Shapiro's (2003) stress sensitivity model and hence provide justification for using this approach to model the effect of stress on properties of both isotropic and anisotropic rocks.

- Chapter 3. The main objective has been achieved with the development of a new stress dependency model for TI media for parameterization of dependencies of the elastic properties of shales. The proposed model is based on a combination of the dual porosity approach of Shapiro (2003) and the

non-interactive approximation of Sayers and Kachanov (1995). Our findings suggested that the proposed model allows the prediction of stress dependency of all five elastic compliances if only three or four compliances are known. This opens up new opportunities for the reconstruction of stress dependencies of all five elastic compliances of shale from log data, when detailed information is not available or is hard to obtain.

- Chapter 4. In this chapter, we further developed the model proposed in Chapter 3 for prediction of elastic properties variation due to application of uniaxial stress for TI media with discontinuities. The results of numerical simulations have shown that (a) effects caused by application of small uniaxial stresses can be described using four physically plausible parameters, and (b) predicted variations in elastic velocities are in a good agreement with experimentally measured data. This allowed the model to be used for prediction of elastic properties response to application of a small uniaxial stress normal to the bedding plane when only variation of elastic properties with isotropic stress is known.

- Chapter 5. In this chapter, we used the Clay-Plus-Silt (CPS) model that is based on two physical parameters, namely, clay packing density and silt fraction that are considered to be the key parameters for modelling of elastic properties of shales. Knowledge of these parameters allows accurate prediction of elastic properties of shales without detailed mineralogical analysis, whereas clay packing density and silt fraction parameters may relatively easy be obtained from wireline measurements or derived from common log measurements such as neutron-density separation or similar quantitative mineralogy information. The clay packing density parameter is shown to be a proxy of the effect of compaction processes on elastic properties of clay matrix of shales. Elastic coefficients of clay have shown no increase with depth. The predicted velocities show good agreement with the measured velocities but a systematic shift is observed for shear velocities. In addition, the inverted elastic moduli of wet clay, as compared to the elastic moduli of shale, have shown much stronger correlation with clay porosity.

This confirmed the hypothesis that silt fraction is one of the key parameters for modelling of elastic properties of shale.

REFERENCES

ABAQUS, Inc., 2004, ABAQUSTM, ABAQUS. Version 6.5 Documentation.

Abousleiman, Y., Tran, M. H., Hoang, S. K., Ortega, J. A. and Ulm, F. J., 2010, Geomechanics field characterization of Woodford Shale and Barnett Shale with advanced logging tools and nano-indentation on drill cuttings. The Leading Edge, **29**, 730-736.

Aleksandrov, K. S. and Ryzhova, T. V., 1961, Elastic properties of rock-forming minerals II. Layered silicates, Bull. Acad. Sci. USSR, Geophys. Ser. English translation (12), 1165-1168.

Alliez, P., Ucelli, G., Gotsman, C. and Attene, M., 2005, Recent Advances in Remeshing of Surfaces. Research Report, AIM@SHAPE Network of Excellence.

Al-Raoush, R. I. and Wilson, C. S., 2005, A pore-scale investigation of a multiphase porous media system. Journal of Contaminant Hydrology, **77 (2005)**, 67 – 89, doi:10.1016/j.jconhyd.2004.12.001.

Angus, D. A., Verdon, J. P., Fisher, Q. J. and Kendall, J. M., 2009, Exploring trends in microcrack properties of sedimentary rocks: An audit of dry-core velocity-stress measurements. Geophysics, **74(5)**, E193-E203.

Arns, C. H., Knackstedt, M. A., Pinczewski, W. V. and Garboczi, E. J., 2002, Computation of linear elastic properties from microtomographic images: Methodology and agreement between theory and experiment. Geophysics, **67(5)**, 1396-1405.

AVIZO, VSG. (2009). Visilog 6, reference guide.

Avseth, P., Draege, A., A.-J. Van Wijngaarden, Johansen, T. A. and Jorstad, A., 2008, Shale rock physics and implications for AVO analysis: A North Sea demonstration. The Leading Edge, **27(6)**, 788-797.

Banik, N. C., 1984, Velocity anisotropy in shales and depth estimation in the North Sea basin. Geophysics, **49**, 1411-1419.

Barber, C. B., Dobkin, D. P. and Huhdanpaa, H. T., 1996, The Quickhull Algorithm for Convex Hulls. ACM Trans. Mathematical Software, **22**, 469-483.

Bayuk, I. O., Ammerman, M. and Chesnokov, E. M., 2007, Elastic moduli of anisotropic clay. Geophysics, **72(5)**, D107-D117.

Becker, K., Shapiro, S., Stanchits, S., Dresen, G. and Vinciguerra, S., 2007, Stress induced elastic anisotropy of the Etnean basalt: Theoretical and laboratory examination. Geophysical Research Letters, **34(11)**.

Berryman, J. G., 1980. Long-wavelength propagation in composite elastic media I. Journal of Acoustic Society of America, **69**, 416-424.

Berryman, J. G., 1980. Long-wavelength propagation in composite elastic media II. Ellipsoidal inclusions. Journal of Acoustic Society of America, **68(6)**, 1820-1831.

Castagna, J. P., Batzle, M. L. and Eastwood, R. L., 1985, Relationships between Compressional-Wave and Shear-Wave Velocities in Clastic Silicate Rocks, Geophysics, **50(4)**, 571-581.

Castagna, J. P., Batzle, M. L. and Kan T. K., 1993, Rock physics – The link between rock properties and AVO response in Offset-Dependent Reflectivity in Theory and practice of AVO Analysis, edited by Castagna, J. P. and Backus, M., pp. 135-171, Society of Exploration Geophysicists, Tulsa, Oklahoma.

Ciz, R. and Shapiro, S. A., 2009, Stress-dependent anisotropy in transversely isotropic rocks: Comparison between theory and laboratory experiment on shale. Geophysics, **74(1)**, D7-D12.

Crampin, S., 1985, Evaluation of anisotropy by shear-wave splitting. Geophysics, **50(1)**, p. 142-152, doi: 10.1190/1.1441824.

De Berg, M., Cheong, O., Kreveld, M. and Overmars, M., 2008, Computational Geometry: Algorithms and applications. Springler-Verlag. ISBN 978-3-540-77973-5.

De Paula, O. B., Pervukhina, M. and Gurevich, B., 2008, Role of compliant porosity in stress dependency of ultrasonic velocities in carbonates and sandstones. Proceedings of the third National Geophysical symposium, Belem-Para.

Delaunay, B., 1934, Sur la Sphere Vide. Izvestia Akademia Nauk SSSR, VII Seria, Otdelenie Matematicheskii i Estestvennykh Nauk, **7**, 793-800.

Delle Piane, C., Dewhurst, D. N., Siggins, A. F. and Raven, M. D., 2010, Stress-induced anisotropy in saturated shale. Geophysical Journal International, **184(2)**, 897-906, doi:10.1111/j.1365-246X.2010.04885.x.

Desbois, G., Urai, J. L. and Kukla, P. A., 2009, Morphology of the pore space in claystones – evidence from BIB/FIB ion beam sectioning and cryo-SEM observations, eEarth, **4**, 15-22.

Dewhurst, D. N. and Siggins, A. F., 2006, Impact of fabric, misrocracks and stress field on shale anisotropy, Geophysical Journal International, **165**, 135-148.

Dewhurst, D. N., Siggins, A. F., Kuila, U., Clennell, M. B., Raven, M. D. and Nordgard-Bolas, H. M., 2008a, Elastic, Geomechanical and Petrophysical Properties of Shales. Paper presented at American Rock Mechanics Association Symposium.

Dewhurst, D. N., Siggins, A. F., Kuila, U., Clennell, M. B., Raven, M. D. and Nordgard-Bolas, H. M., 2008b, Rock Physics, Geomechanics and Rock Properties in Shales: Where Are The Links?, Paper presented at Proceedings of the 1st SHIRMS conference.

Draege, A., Jakobsen, M. and Johansen, T. A., 2006, Rock physics modelling of shale diagenesis. Petroleum Geoscience, **12(1)**, 49-57.

Drury, M. R. and Fitz Gerald, J. D., 1996, Grain boundary melt films in an experimentally deformed olivine-orthopyroxene rock: implications for melt distribution in upper mantle rocks. Geophysical Research Letters, **23**, 701–704.

Dvorkin, J., 2009, Accuracy and Relevance of Digital Rock Results: Successes and Failures. Ingrain Digital Rock Physics Lab, **1-22**.

Eberhart-Phillips, D., Han, D.-H. and Zoback, M. D., 1989, Empirical relationships among seismic velocity, effective pressure, porosity and clay content in sandstone. Geophysics, **54(1)**, 82-89.

Ellis, D. V. and Singer, J. M., 2008, Well Logging for Earth Scientists. Springer, The Netherlands.

Flannery, B. P., Deckman, H. W., Roberge, W. G. and D'Amico, K. L., 1987, Three-Dimensional X-ray Microtomography. Science, **237(4821)**, 1439-1444.

Fortin, J., Gueguen, Y. and Schubnel, A., 2007, Effects of pore collapse and grain crushing on ultrasonic velocities and V_p/V_s. Journal of Geophysical Research, **112**, B08207, doi:10.1029/2005JB004005.

Garbozci, E. J., 1998, Finite element and finite difference programs for computing the linear electrical and elastic properties of digital images of random materials. National Institute of Standards and Technology Internal report.

Garland, M. and Heckbert, P., 1997, Surface simplification using quadric error metrics. Proceedings of the 24th Annual Conference on Computer Graphics and Inteactive Techniques, 209-216.

Gassmann, F., 1951, Uber die Elastizitat poroser Medien. Vierteljahrschrift der Naturforschenden Gesellschaft in Zurich, **96**, 1-23.

Gurevich, B., Makarynska, D. and Pervukhina, M., 2009, Are penny-shaped cracks a good model for compliant porosity? SEG, edited. SEG, Houston, USA.

Gurevich, B., Makarynska, D., Pervukhina, M. and De Paula, O., 2009, A New Squirt-Flow Model for Elastic Wave Attenuation and Dispersion in Fluid-Saturated Rocks. Poro-Mechanics Iv, 700-705, 1151.

Gurevich, B., Pervukhina, M. and Makarynska, D., 2011, An analytical model for stress-induced anisotropy of dry rocks. Geophysics, **76**, 125-133.

Han, D.-H., Nur, A. and Morgan, D., 1986, Effects of porosity and clay content on wave velocities in sandstones. Geophysics, **51**, 2093-2107.

Hornby, B. E., Schwartz, L. M. and Hudson, J. A., 1994, Anisotropic effective-medium modeling of the elastic properties of shales. Geophysics, **59(10)**, 1570-1583.

Hornby, B. E., 1998, Experimental laboratory determination of the dynamic elastic properties of wet, drained shales. Journal of Geophysical Research, **103**, 29945–29964.

Jakobsen, M. and Johansen, T. A., 2000, Anisotropic approximations for mudrocks: a seismic laboratory study. Geophysics, **65**, 1711-1725.

Jakobsen, M., Hudson, J. A., Minshull, T. A. and Singh, S. C., 2000, Elastic properties of hydrate-bearing sediments using effective medium theory. Journal of Geophysical Research - Solid Earth, **105(B1)**, 561-577.

Jensen, E. H., Andersen, C. F. and Johansen, T. A., 2011, Estimation of elastic moduli of mixed porous clay composites. Geophysics, **76**, E9-E20.

Johansen, T. A., Ruud, B. O. and Jakobsen, M., 2004, Effect of grain scale alignment on seismic anisotropy and reflectivity of shales. Geophysical Prospecting, **52**, 133-149.

Johnston, J. E. and Christensen, N. I., 1993, Compressional to shear velocity ratios in sedimentary rocks: International Journal of Rock Mechanics and Mining Sciences and Geomechanics. Abstract, **30**, 751-754.

Johnston, J. E. and Christensen, N. I., 1995, Seismic anisotropy of shales. Journal of Geophysical Research, **100(B4)**, 5991-6003.

Jones, L. E. A. and Wang, H. F., 1981, Ultrasonic Velocities in Cretaceous Shales from the Williston Basin. Geophysics, **46(3)**, 288-297.

Kachanov, M., Prioul, R. and Jocker, J., 2010, Incremental linear-elastic response of rocks containing multiple rough fractures: Similarities and differences with traction-free cracks. Geophysics, **75(1)**, D1-D11.

Kaestner, A., Lehmann, E. and Stampanoni, M., 2008, Imaging and image processing in porous media research. Advances in Water Resorces, **31**, 1174-1187.

Katahara, K. W., 1996, Clay mineral elastic properties, in SEG Annual Meeting Expanded Technical Programme Abstracts, edited, pp. 1691-1694.

Kuila, U., Dewhurst, D. N., Siggins, A. F. and Raven, M. D., 2011, Stress anisotropy and velocity anisotropy in low porosity shale. Tectonophysics, doi:10.1016/j.tecto.2010.09.023, **503(1-2)**, 34-44.

Liu, H. H., Rutqvist, J. and Berryman, J. G., 2008, On the relationship between stress and elastic strain for porous and fractured rock. International Journal of Rock Mechanics and Mining Sciences, **46(2)**, 289-296, doi:10.1016/j.ijrmms.2008.04.005.

MacBeth, C., 2004, A classification for the pressure-sensitivity properties of a sandstone rock frame. Geophysics, **69**, 497-510.

MacBeth, C. and Schuett, H., 2007, The stress dependent elastic properties of thermally induced microfractures in aeolian Rotliegend sandstone. Geophysical Prospecting, **55(3)**, 323-332.

Marion, D. and Nur, A., 1991, Pore-Filling Material and Its Effect on Velocity in Rocks. Geophysics, **56(2)**, 225-230.

Marion, D., 1990, Acoustical, mechanical and transport properties of sediments and granular materials. Stanford University.

Matthijs de Winter, D. A., Schneidjdenberg, C. T. W. M., Lebbink, M. N., Lich, B., Verkleij, A. J., Drury, M. R. and Humbel, B. M., 2009, Tomography of insulated biological and geological materials using focused ion beam (FIB) sectioning and low-kV BSE imaging. Journal of Microscopy, **233**, 372–383.

Mavko, G. and Nur, A., 1978, The effect of Nonelloptical Cracks on the Compressibility of Rocks, Journal of Geophysical Research, **83**, 4459-4468, 1978.

Mavko, G., and Jizba, D., 1991, Estimating grain-scale fluid effects on velocity dispersion in rocks. Geophysics, **56(12)**, 1940-1949.

Mavko, G., Mukerji, T. and Dvorkin, J., 1998, The rock physics handbook. Tools for seismic analysis in porous media. Cambridge University Press. ISBN 0 521 62068 6.

Mayo, S., Davis, T., Gureev, T., Miller, P., Paganin, D., Pogany, A., Stevenson, A. and Wilkins, S., 2003, X-ray phase-contrast microscopy and microtomography. Optic Express, **11(19)**, 2289-2302.

Miller, D. E., Horne, S. A. and Walsh, J., 2012, Precise inversion of logged slownesses for elastic parameters in a gas shale formation. Geophysics, **77(4)**, B197-B206.

Mondol, N. H., Bjorlykke, K., Jahren, J. and Hoeg, K., 2007, Experimental mechanical compaction of clay mineral aggregates - Changes in physical properties of mudstones during burial. Marine and Petroleum Geology, **24**, 289-311.

Moré, J. J., 1977, The Levenberg-Marquardt Algorithm: Implementation and Theory. Springer Verlag.

Najman, L. and Schmitt, M., 1994, Watershed of a continuous function. Signal Processing (Special issue on Mathematical Morphology), **38**, 99–112.

Nikolaou, N. and Papamarkos, N., 2009, Color reduction for complex document images. International Journal of Imaging Systems and Technology, **19(1)**, 14-26.

Nishizawa, O., 1982, Seismic velocity anisotropy in a medium containing oriented cracks - transversely isotropic case. Journal of Physics of the Earth, **30**, 331-347.

Nur, A., 1971, Effects of stress on velocity anisotropy in rocks with cracks. J. Geophys. Res., **76**, 2022-2034.

Nygard, R., Gutierrez, M., Gautam, R. and Hoeg, K., 2004, Compaction behavior of argillaceous sediments as function of diagenesis. Marine and Petroleum Geology, **21**, 349–362.

Ortega, J. A., Ulm, F.-J. and Abousleiman, Y., 2007, The effect of the nanogranular nature of shale on their poroelastic behavior. Acta Geotechnica.

Ortega, J. A., Ulm, F. J. and Abousleiman, Y., 2009, The nanogranular acoustic signature of shale. Geophysics, **74(3)**, D65-D84.

Pal-Bathija, A., Prasad, M., Liang, H., Upmanyu, M., Lu, N. and Batzle, M., 2008, Elastic properties of clay minerals. SEG Technical Program Expanded Abstracts 2, edited, pp. pp. 1610-1614.

Peltonen, C., Marcussen, O., Bjorlykke, K. and Jahren, J., 2008, Mineralogical control on mudstone compaction: a study of Late Cretaceous to Early Tertiary mudstones of the Voring and More basins, Norwegian Sea. Petroleum Geoscience, **14**, 127-138.

Peltonen, C., Marcussen, O., Bjorlykke, K. and Jahren, J., 2009, Clay mineral diagenesis and quartz cementation in mudstones: the effects of the smectite to illite reaction on rock properties. Marine and Petroleum Geology, **26**, 887-898.

Pervukhina, M., Siggins, A. F., Dewhurst, D. N. and Gurevich, B., 2007, Elastic properties of shales with respect to silt fraction. ASEG, Extended Abstract, Perth.

Pervukhina, M., Dewhurst, D. N., Gurevich, B., Kuila, U., Siggins, A. F., Raven, M. and Hordgard Bolas, H. M., 2008a, Stress-dependent elastic properties of shales: Measurement and modeling. The Leading Edge, **27(6)**, 772-779.

Pervukhina, M., Dewhurst, D. N., Kuila, U., Siggins, A. F. and Gurevich, B., 2008b, Stress Dependent Anisotropy in Shales: Measurements and Modelling. Proceedings. SHIRMS, **2**, 287-300.

Pervukhina, M., Gurevich, B., Dewhurst, D. N. and Siggins, A. F., 2010, Applicability of velocity–stress relationships based on the dual porosity concept to isotropic porous rocks. Geophysical Journal International, **181(3)**, 1473–1479, doi:10.1111/j.1365-246X.2010.04535.x.

Pervukhina, M., Delle Piane, C., Dewhurst, D. N., Clennell, M. B. and Nordgard Bolas, H. M., 2013, An Estimation of Pore Pressure in Shales from Sonic Velocities. 83rd SEG Annual Meeting, Extended Abstract, Houston, USA.

Prasad, M., Kopycinska, M., Rabe, U. and Arnold, W., 2002, Measurement of Young's modulus of clay minerals using atomic force acoustic microscopy. Geophysical Research Letters, **29(8)**.

Prasad, M., Hofmann, R., Batzle, M., Kopycinska-Muller, M., Rabe, U. and Arnold, W., 2005, Values of mineral modulus of clay. SEG Technical Program Expanded Abstracts.

Prioul, R. and Lebrat, T., 2004, Calibration of velocity-stress relationships under hydrostatic stress for their use under non-hydrostatic stress conditions. SEG Extended Abstract, edited, pp. 1698-1701, Denver, USA.

Prioul, R., Bakulin, A. and Bakulin, V., 2004, Nonlinear rock physics model for estimation of 3D subsurface stress in anisotropic formations: Theory and laboratory verification. Geophysics, **69(2)**, 415-425.

Qi, Z., Zambelli, J., Bevins, N. and Chen, G-H., 2010, Quantitative imaging of electron density and effective atomic number using phase contrast CT. Physics in Medicine and Biology, **55**, 2669-2677.

Roberts, A. P. and Garboczi, E. J., 2000, Elastic properties of model porous ceramics. Journal of American Ceramic Society, **83**, 3041–3048.

Ruud, B. O., Jakobsen, M. and Johansen, T. A., 2003, Seismic properties of shales during compaction. SEG Extended Abstract, Dallas, USA.

Saenger, E., Ciz, R., Kruger, O., Schmalholz, S., Gurevich, B. and Shapiro, S., 2007, Finite-difference modelling of wave propagation on microscale: A snapshot of the work in progress. Geophysics, **72(5)**, 1293-1300.

Sayers, C. M., 1988, Stress-induced ultrasonic wave velocity anisotropy in fractured rock. Ultrasonics, **26**, 311-317.

Sayers, C.M., 1988, Inversion of ultrasonic wave velocity measurements to obtain the microcrack orientation distribution function in rocks. Ultrasonics, **26**, 73-77.

Sayers, C. and Kachanov, M., 1995, Microcrack-indused elastic wave anisotropy of brittle rock. Journal of Geophysical Research, **100**, 4149-4156.

Sayers, C., 1999, Stress-dependent seismic anisotropy of shales. Geophysics, **64(1)**, 93-98.

Sayers, C. and Han, D.-H., 2002, The effect of pore fluid on the stress-dependent elastic wave velocities in sandstones. SEG Extended Abstract, Salt Lake City, USA.

Sayers, C., 2005, Seismic anisotropy of shales. Geophysical Prospecting, **53**, 667-676.

Sayers, C., Taleghani, A. D. and Adachi, J., 2009, The effect of mineralization on the ratio of normal to tangential compliance of fractures. Geophysical Prospecting, **57(3)**, 439-446.

Sayers, C. M., 2013, The effect of anisotropy on the Young's moduli and Poisson's ratios of shales. Geophysical Prospecting, **61(2)**, 416-426.

Schoenberg, M., 2002, Time-dependent anisotropy induced by pore pressure variation in fractured rock. Journal of Seismic Exploration, **11(1-2)**, 83-105.

Shapiro, S. A., 2003, Elastic piezosensitivity of porous and fractured rocks. Geophysics, **68(2)**, 482-486.

Shapiro, S. A. and Kaselow, A., 2005, Porosity and elastic anisotropy of rocks under tectonic stress and pore-pressure changes. Geophysics, **70(5)**, 27-38.

Shikhaliev, P. M., 2008, Computed tomography with energy-resolved detection: a feasibility study. Physics in Medicine and Biology, **53**, 1475-1495.

Shulakova, V., Pervukhina, M., Lebedev, M., Mueller, T., Mayo, S., Schmid, S., Clennel, B. and Gurevich, B., 2011, Computation of elastic properties based on microtomogram images. 73rd EAGE conference, Vienna, Austria, Extended Abstract.

Siggins, A. F. and Dewhurst, D. N., 2003, Saturation, pore pressure and effective stress from sandstone acoustic properties. Geophysical Research Letters, **30(2)**, 1089, doi:10.1029/2002GL016143.

Sinha, B. K., Vissapragada, B., Renlie, L. and Tysse, S., 2006, Radial profiling of the three formation shear moduli and its application to well completions. Geophysics, **71(6)**, E65-E77.

Solymar, M. and Fabricius, I. L., 1999, Image Analysis and Estimation of Porosity and Permeability of Arnager Greensand, Upper Cretaceous, Denmark. Physics and Chemistry of the Earth (A), **24(7)**, 587-591.

Spanne, P., Thovert, J., Jacquin, J., Lindquist, W. B., Jones, K. and Coker, D., 1994, Synchrotron computed microtomography of porous media: topology and transports. Physical Review Letters, **73**, 2001-2004.

Storvoll, V. and Brevik, I., 2008, Identifying time, temperature, and mineralogical effects on chemical compaction in shales by rock physics relations. The Leading Edge, **27(6)**, 750-756, doi:10.1190/1.2944160.

Surazhsky, V., Alliez, P. and Gotsman, C., 2003, Isotropic remeshing of surfaces: a local parameterization approach. Proceedings of 12th International Meshing Roundtable, Sandia National Laboratories, 215–224.

Szymczak, A., Rossignac, J. and King, D., 2003, Piecewise regular meshes: Construction and compression. Graphical models.

Thomsen, L., 1986, Weak Elastic Anisotropy. Geophysics, 51(10), 1954-1966.

Tsvankin, I., 1997, Anisotropic parameters and P-wave velocities for orthorhombic media. Geophysics, **62**, 1292-1309.

Tsvankin, I., Larner, K., Gaiser, J. and Grechka, V., 2009, Seismic Anisotropy - Introduction. Geophysics, **74(5)**, Wb1-Wb2.

Ulm, F. J. and Abousleiman, Y., 2006, The nanogranular nature of shale. Acta Geotechnica, **1(2)**, 77-88.

Van Geet, M. and Swennen, R., 2001, Quantitative 3D-fracture analysis by means of microfocus X-ray computer tomography (mCT): An example from coal. Geophysical Research Letters, **28**, 3333–3336.

Vanorio, T., Prasad, M. and Nur, A., 2003, Elastic properties of dry clay mineral aggregates, suspensions and sandstones. Geophysical Journal International, **155**, 319-326.

Vernik, L. and Kachanov, M., 2010, Modelling elastic properties of siliciclastic rocks. Geophysics, **75(6)**, E171-E182.

Voltolini, M., Wenk, H. R., Mondol, N. H., Bjorlykke, K. and Jahren, J., 2009, Anisotropy of experimentally compressed kaolinite-illite-quartz mixtures. Geophysics, **74(1)**, D13-D23.

Vlastos, S., Liu, E., Main, I. G., Schoenberg, M. Narteau, C., Li, X.Y. and Maillot, B., 2006, Dual simulations of fluid flow and seismic wave propagation in a fractured network: effects of pore pressure on seismic signature. Geophys. J. Int., **166**, 825-838.

Walsh, J., 1965, The effect of cracks on the compressibility of rock. Journal of Geophysical Research, **70**, 381-389.

Wang, Z. J., Wang, H. and Cates, M. E., 2001, Effective elastic properties of solid clays. Geophysics, **66(2)**, 428-440.

Wang, Z. J., 2002, Seismic anisotropy in sedimentary rocks, part 2: Laboratory data. Geophysics, **67(5)**, 1423-1440.

Wenzlau, F. and Müller, T. M., 2009, Finite-difference modelling of wave propagation and diffusion in poroelastic media. Geophysics, **74**, T55-T66.

Wenzlau, F., Altmann, J. B. and Müller, T. M., 2010, Ansiotropic dispersion and attenuation due to wave-induced flow: quasi-static finite-element modelling in poroelastic solids. Journal of Geophysical Research, **115**, B07204.

Westenberger, P., 2008, AVIZO - 3D visualization framework. Geoinformatics Conference, 1-11.

Woeber, A. F., Katz, S. and Ahrens, T. J., 1963, Elasticity of selected rock and minerals. Geophysics, **28**, 658-663.

Yang, Y. S., Gureyev, T. E., Tulloh, A., Clennell, B. and Pervukhina, M., 2010, Feasibility of a data-constrained prediction of hydrocarbon reservoir sandstone microstructures. Measurement Science and Technology, **21**, doi:10.1088/0957-0233/21/4/047001.

Yasushi, I., Shin, A., Erukala, A., Soni, B., Chernikov, A., Chrisochoides, N. and Nakahashi, K., 2004, Parallel unstructured mesh generation by an advancing front method. MASCOT04-IMACS/ISGG Workshop.

Zimmerman, R. W., Somerton, W. H. and King, M. S., 1986, Compressibility of porous rocks. Journal of Geophysical Research, **91**, **12**, 765-12, 777.

Zimmerman, R. W., 1991, Compressibility of sandstones. Elsevier, Amsterdam.

Every reasonable effort has been made to acknowledge the owners of copyright material. I would be pleased to hear from any copyright owner who has been omitted or incorrectly acknowledged.

Appendix B contains permission statements from the copyright owners of the material presented in this thesis, which was published as journal articles or conference extended abstracts. I acknowledge SEG copyright of materials published as either SEG extended abstracts or papers in Geophysics and that the papers were reprinted with SEG permission (see Appendix B).

APPENDIX A

STRESS DEPENDENCY OF ELASTIC COMPLIANCES OF TRANSVERSELY ISOTROPIC MEDIA WITH ANISOTROPICALLY DISTRIBUTED DISCONTINUITIES

Orientation distribution of cracks is commonly described with the help of two coordinate systems, global (measurement system) and local (associated with the orientation of an individual crack). The two systems are related by three Eulerian angles (θ, φ, ψ), where θ ranges lie in the range [0, π] and determine the angle between the *z'*-axis of the local system and the *z*-axis of global system, φ controls the rotation about the *z*-axis (range [0, 2π]), and ψ specifies the rotation of the crack about the local *z'*-axis (range [0, 2π]). If the *z'*-axis of the local coordinate system coincides with the normal to the crack surface, we reduce the number of angles to two, namely, θ and φ. The spherical system determined with these two angles and the *z*-axis, which here is assumed to coincide with the axis of rotational symmetry of the medium, is a convenient system for calculating α_{ij} and β_{ijkl} tensors from equations 3.5 and 3.6. Note that the three components of a unit vector in a spherical coordinate system can be written as:

$$n_1 = sin\theta cos\varphi, \tag{A.1}$$

$$n_2 = sin\theta cos\varphi, \tag{A.2}$$

$$n_3 = cos\theta. \tag{A.3}$$

Calculation of α_{ij} and β_{ijkl} tensors for cracks with a particular orientation distribution function, determined by equations 3.1 and 3.2 and with surface area governed by equation 3.3, involves integration over all possible orientations of cracks, i.e. over all angles θ and φ that define the direction of the normal to a crack surface. Integration over the angles θ and φ is integration over the surface of a unit sphere; the infinitesimal element of the surface should be written as $\sin\theta d\theta d\varphi$.

The probability that the normal to the surface of the crack forms an angle θ with the *z*-axis that lies in the interval [θ_1, θ_2] can be written as:

$$P(\theta_1 \le \theta \le \theta_2) = \int_0^{2\pi}\int_0^{\pi} W(\theta,\varphi)\sin\theta d\theta d\varphi \tag{A.4}$$

or, if we take into account equation 3.1, as follows:

$$P(\theta_1 \le \theta \le \theta_2) = \int_0^{2\pi}\int_{\theta_1}^{\theta_2} \frac{1+\eta\cos^2\theta}{4\pi(1+\eta/3)} \sin\theta d\theta d\varphi$$

$$= \frac{1}{4\pi(1+\eta/3)} \int_0^{2\pi}\int_{\theta_1}^{\theta_2} (1+\eta\cos^2\theta)\sin\theta d\theta . \qquad (A.5)$$

The specific number of cracks per unit volume whose normals form an angle θ with the *z*-axis that lie in the interval [θ_1, θ_2] can then be written as:

$$N(\theta_1 \le \theta \le \theta_2) = \frac{N_0}{4\pi(1+\eta/3)}$$

$$\times \int_0^{2\pi}\int_{\theta_1}^{\theta_2} (1+\eta\cos^2\theta)\sin\theta d\theta d\varphi . \qquad (A.6)$$

where N_0 is the total number of cracks.

In equation 3.5, summation over all cracks can be replaced with integration over all angles, and α_{ij} for a unit volume can be written as:

$$\alpha_{ij} = \frac{N_0}{4\pi(1+\eta/3)} \int_0^{2\pi}\int_0^{\pi} B_T A(1+\eta\cos^2\theta) n_i n_j \sin\theta d\theta d\varphi . \qquad (A.7)$$

Taking into account equation 3.3 and assuming that B_T is the same for all crack orientations, equation A.7 can be rewritten as:

$$\alpha_{ij} = \frac{N_0 B_T A^0 \exp(-P/P_c)}{4\pi(1+\eta/3)} \int_0^{2\pi}\int_0^{\pi} (1+\eta\cos^2\theta) n_i n_j \sin\theta d\theta d\varphi . \qquad (A.8)$$

Noting that the specific surface area of cracks per unit volume is equal to $s_0 = N_0 A^0$ and denoting $s_n = s_0/(1+\eta/3)$, we can rewrite equation A.8 as follows:

$$\alpha_{ij} = \frac{s_n B_T \exp(-P/P_c)}{4\pi} \int_0^{2\pi}\int_0^{\pi} (1+\eta\cos^2\theta) n_i n_j \sin\theta d\theta d\varphi . \qquad (A.9)$$

Taking into account equations A.1-A.3 and integrating over all angles in equation A.9 we finally get the tensor α_{ij} as follows:

$$\alpha_{ij} = \frac{1}{15} s_n B_T e^{-\frac{P}{P_c}} \begin{bmatrix} 5+\eta & 0 & 0 \\ 0 & 5+\eta & 0 \\ 0 & 0 & 5+3\eta \end{bmatrix}. \tag{A.10}$$

The tensor β_{ijkl} for a unit volume can be obtained in a similar way:

$$\beta_{ijkl} = s_n B_T e^{-\frac{P}{P_c}} \times$$

$$\times \begin{bmatrix} \frac{7B-7+\eta B-\eta}{35} & \frac{7B-7+\eta B-\eta}{105} & \frac{7B-7+3\eta B-3\eta}{105} & & & \\ \frac{7B-7+\eta B-\eta}{105} & \frac{7B-7+\eta B-\eta}{35} & \frac{7B-7+3\eta B-3\eta}{105} & & 0 & \\ \frac{7B-7+3\eta B-3\eta}{105} & \frac{7B-7+3\eta B-3\eta}{105} & \frac{7B-7+5\eta B-5\eta}{35} & & & \\ & & & \frac{4(7B-7+3\eta B-3\eta)}{105} & 0 & 0 \\ & 0 & & 0 & \frac{4(7B-7+3\eta B-3\eta)}{105} & 0 \\ & & & 0 & 0 & \frac{4(7B-7+\eta B-\eta)}{105} \end{bmatrix} \tag{A.11}$$

Substituting α_{ij} and β_{ijkl} into equation 3.4, we obtain the excess compliances (equations 3.7-3.11) caused by cracks with an orientation distribution function given by equation 3.1. If $B = 1$, equations 3.7-3.11 reduce to equations 3.12-3.16.

APPENDIX B

SEG PUBLICATIONS

Letter from Ted Bakamjian
Director, Publications
Society of Exploration Geophysicists

From: Ted Bakamjian <Tbakamjian@seg.org>
Sent: Friday, 1 May 2015 10:34 AM
To: Pavel Golodoniuc <pavel.golodoniuc@postgrad.curtin.edu.au>
Cc: Permissions <permissions@seg.org>
Subject: Re: Permission to use copyright material

Greetings Pavel,

Please find the permission you request in the attached form.

Sincerely,
Ted

--
Ted Bakamjian, IOM CAE
Director, Publications
Society of Exploration Geophysicists
P. O. Box 702740, Tulsa, OK 74170-2740 USA
Shipping: 8801 S. Yale Ave., Suite 500, Tulsa, OK 74137
Phone: (918) 497-5506; Fax: (918) 497-5557
Web: http://www.seg.org/
SEG Digital Library: http://library.seg.org

PERMISSION TO USE COPYRIGHT MATERIAL AS SPECIFIED BELOW

- Pervukhina M., Gurevich B., Golodoniuc P., and Dewhurst D. N., 2010, Parameterization of elastic stress sensitivity in shales: Geophysics, **76(3)**, p. WA147–WA155, doi:10.1190/1.3554401, http://dx.doi.org/10.1190/1.3554401.
- Pervukhina M., Gurevich B., Golodoniuc P., and Dewhurst D. N., 2011, Stress dependency of elastic properties of shales: the effect of uniaxial stress: SEG Extended abstract, San Antonio, USA, doi:10.1190/1.3627669, http://dx.doi.org/10.1190/1.3627669.
- Pervukhina M., Golodoniuc P., Gurevich B., Clennell M. B., Dewhurst D. N., and Nordgård Bolås H. M., 2015, Prediction of sonic velocities in shale from porosity and clay fraction obtained from logs – a North Sea well case study: Geophysics, **80(1)**, p. D1-D10, doi:10.1190/GEO2014-0044.1, http://dx.doi.org/10.1190/geo2014-0044.1.

I hereby give permission for Pavel Golodoniuc to include the abovementioned material(s) in his higher degree thesis for the Curtin University of Technology, and to communicate this material via the Australasian Digital Thesis Program. This permission is granted on a non-exclusive basis and for an indefinite period.

I confirm that I am the copyright owner of the specified material.

Permission to use this material is subject to the following conditions:

Please include DOI-based permalinks in citations for these articles. Please also ensure that the links are live in online versions of your theses. Also, please acknowledge SEG copyright and that the papers are reprinted with SEG permission. Thank you for publishing in Geophysics. Best of luck with your thesis.

Signed: 

Name: Ted Bakamjian

Position: SEG Director, Publications

Date: 1/05/2015

Copyright permissions statement from
http://www.seg.org/resources/publications/permissions

PERMISSIONS

SEG publishes journals, books, and digital works with the primary aim of disseminating research in and theory and applications of applied geophysics. Consistent with this objective, the Society provides mechanisms for those who seek to reuse or republish material from SEG publications while protecting the viability of the SEG publications program. Any further questions about permissions can be sent via email to the SEG publications department at permissions@seg.org.

Fair use

Authors and publishers may present or republish up to two figures or tables per SEG article or per SEG book without seeking written permission from SEG, provided that full acknowledgment of the source is provided in the new work. If SEG has cited a publication for which it is not the publisher, rights should be obtained from that publisher. SEG considers this fair use. There are no fees associated with this permission. Authors who need documentation that SEG is extending this permission are encouraged to print this message and present it to their publishers. Those who require further documentation should contact the SEG publications director. Requests to use any portion of "Seismic Data Analysis: Processing, Inversion, and Interpretation of Seismic Data" should be directed to the SEG publications director.

Permission granting

Those seeking permission to republish more material than described above should contact the SEG publications director. Such requests should include complete citations of works for which permission to republish is sought. If permission for specific figures or tables is sought, please provide figure and table numbers. Requests should include a description of the work in which the SEG material would be republished. Information about the audience and the intended distribution also should be included. The requests should be prepared on institutional letterhead if the

requesting party is representing an institution. License fees are assessed only when the request is for a large amount of material or when the proposed usage is commercial in nature or would limit SEG's market. If a license fee is assessed, it must be paid prior to use or the permission is void.

Purchase redistribution rights online

Those seeking to redistribute SEG publications or portions thereof in print, by fax, or online may purchase permission to do so online. SEG publications are registered with the Copyright Clearance Center, and licenses to redistribute SEG articles and portions of books are obtained through this nonprofit agency. Special pricing is available for university professors, including license to distribute SEG material through electronic course packs. Licenses also are available for distribution of journal articles and expanded abstracts via email or posting on Intranets and Extranets for limited time periods.

Authors' right to redistribute

Authors of articles in Geophysics, Interpretation, The Leading Edge, and the Technical Program Expanded Abstracts may post their own articles on their personal Web sites or the Web sites of their institutions without obtaining further permission from SEG. Authors of journal articles and Expanded Abstracts retain similar rights for print redistribution. If an author or an author's institution redistributes an author's article online or in print, the original publication venue encompassed in a complete citation and including SEG's status as publisher must be identified. Authors of SEG books, or portions of SEG books, must seek permission from the SEG publications director to redistribute these works in any form. Such permission will not be withheld if SEG's investment in the original publication of the works is not threatened. Questions should be directed to the publications director.